1.3micron Quantum Dot Lasers and Superluminescent Light Emitting Diodes

Sumon kumar Ray

This thesis is submitted for the degree of Doctor of Philosophy

Department of Electronic and Electrical Engineering

University of Sheffield

January 2007

Contents

Abstract

The work described in this thesis involves the development of gallium arsenide based quantum dot lasers and superluminescent light emitting diodes (SLEDs) emitting around 1.3μm. Initially, the improvement in overall temperature characteristics of a 5 DWELL 1.3μm quantum dot laser is described through a change in the fabricated device design incorporating a shallow ridge etch and selective gold electroplating. This improved fabrication technique allowed higher temperature ground state operation of the laser and an improvement of 10K in the characteristics temperature at a temperature range higher than 60°C. Later a novel method to broaden the emission spectrum of a SLED by incorporating different amounts of indium in different wells of a DWELL structure is proposed and described. For this device 85nm broad emission spectrum is obtained along with 2.5mW of CW output power at room temperature. Further modification of this structure resulted in a SLED with >8mW CW output power and a 95nm wide, flat emission spectrum at room temperature. In the last part of this thesis a new growth mechanism is described to improve the overall performance of lasers, SLEDs and mesa diodes. For the laser structures lower threshold current density, higher efficiency and lower transparency current densities are observed while the SLEDs emitted >40mW CW output power at room temperature which linearly increased with drive current. Also the mesa diodes exhibited lower reverse leakage current and higher breakdown voltages.

Chapter 5: Molecular Beam Epitaxial Growth of High Power Quantum Dot Superluminescent Light Emitting Diodes

Chapter 6: Conclusion (*Page 143-150*)

Acknowledgements

First of all I would like to thank all the members of the QD group and National Centre for III-V semiconductors at Sheffield for their support and valuable advice. Thanks to Kris Groom for his continuous guidance, advice and support in device fabrication and characterization during this whole work. I would also like to thank Hui-Yun and Mark for their support in growing the samples. Also I am thankful to Rob, Abbes, Paul and Dave for their advice on different technological issues. Also I would like to thank Ryan for programming the data acquisition software for the device characterization. Thanks to Paolo and Chao for their help in PL measurements.

Special thanks to my supervisor Richard Hogg for giving me the opportunity to work in a very friendly atmosphere. I would like to thank him also for giving me continuous motivation and inspiration through out my stay in the EEE department. I would also like to thank John David for giving me the opportunity to work in Sheffield. On a personal level I would like to thank my mother Rama Ray and my father Swapan Kumar Ray for their continuous inspiration during my academic career. Also I would like to thank my sister Tum for her support and my partner Somali for her patience. Finally thanks to all my friends.

Dedication

This thesis is dedicated to my parents. This would not have been possible without their continuous inspiration and encouragement through out my academic life.

- Sumon kumar Ray

Chapter 1: Introduction

1.1 Evolution of Low dimensional Physics

The principle issue regarding the development of low dimensional physics is the method of carrier confinement in different directions in the semiconductor. Initially bulk semiconductors were used as the active element in semiconductor light emitting devices in which the motion of the carriers was unrestricted in all the three directions. Further development gave birth to quantum well (QW) structures, where the carriers are confined in the direction of the growth plane. In quantum wire structures the free motion of carriers is further restricted to only one direction. If further restriction on the motion of carriers is imposed, the carriers are confined in all 3 directions. These structures are known as quantum dot (QD) structures. The behaviour of all these structures can be well understood if expressed in terms of their density of states (DOS).

As stated above the motion of the carriers are completely unrestricted in all the directions of the semiconductor and the DOS is given by

$$g(E) = 1/2\pi^2[(2m_{eff})^{3/2} / \pi\hbar^2]E^{1/2} \qquad (1.1)$$

where m_{eff} is the effective mass of the carrier, $\hbar$ is Planck's constant and E is the carrier energy. The DOS of the carriers confined in a 2-dimensional plane (*ie.* QW structures) is given by the following equation

$$g(E) = [m_{eff} / \pi\hbar^2] \qquad (1.2)$$

For the QD structures the motion of the charge carriers in a semiconductor material are restricted to a confined area with a dimension of the de Broglie wavelength (~10nm or less in each direction) [1]. Considering this confinement of the carriers the DOS is expressed as

$$g(E) = \delta (E-E_n) \qquad (1.3)$$

where $\delta(x)$ is the delta function and E_n ($n = 1, 2, 3\ldots$) are the energies of the confined states of the carrier. This discrete DOS of the QD represents well-defined energy levels for the structure each with a finite degeneracy. The ground state (GS) of the QDs discussed in this chapter is two-fold degenerate and the first excited state is four fold degenerate. Figure 1 shows the schematic diagram of the DOS as a function of the energy for different low dimensional structures.

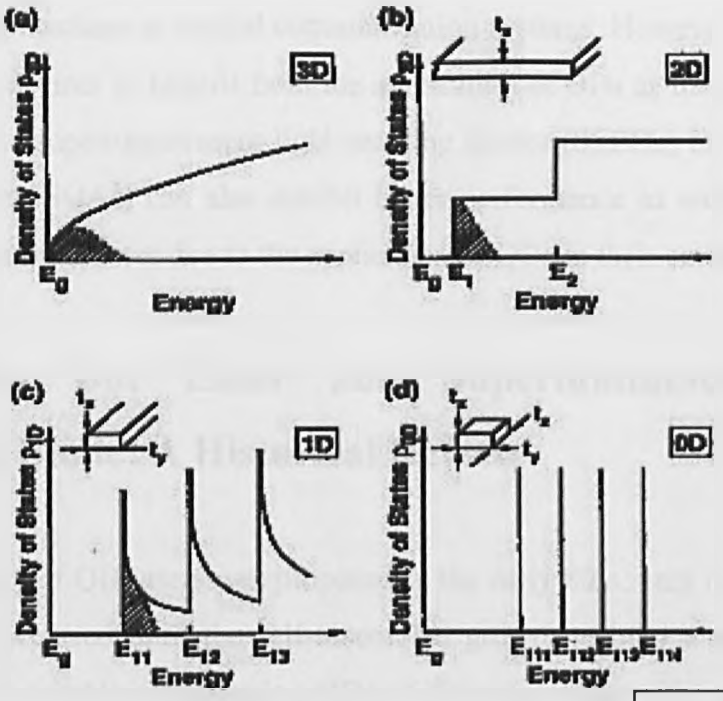

Fig 1.1. Schematic of the density of states as function of the energy of the states for (a) bulk semiconductor, (b) quantum well, (c) quantum wire and (d) quantum dot

Figure taken from,' Quantum Well Lasers' Edited by Zory.

Massive technological developments in epitaxial growth techniques in the last few decades have made it practically possible to realize the advancement of low dimensional physics. The introduction of low dimensional systems as the active region for a laser has resulted in lower threshold current densities [2] and improved temperature stability [3] due to the modified density of states. InP and GaAs based QW lasers have been already employed in various applications in day-to-day life. In 1982 Arakawa and Sakaki first theoretically proposed that the use of quantum dots as the active region of a laser would drastically improve the overall characteristics of the laser due to their delta like DOS [4]. Especially, the temperature characteristic of the laser can be significantly improved due to the confinement of the carrier movement in all dimensions. The same group in 1985 was the first to demonstrate the improvement

excitation carriers out of the ground state lasing state to the excited dot states or even completely out of the dots [15]. Previously, below 175K, almost temperature insensitive operation of QD lasers was reported [16]. Incorporating QDs in the quantum wells was suggested and demonstrated by a group so as to improve the carrier confinement at higher temperature [17]. It has been observed by many other groups that the characteristic temperature for a QD laser strongly depends on the internal loss of the devices. Recently Fathpour *et al.* demonstrated an InAs/GaAs QD laser with infinite characteristic temperature ($T_0 = \infty$) in the temperature range 5-75^{0}C [18]. In chapter 3 a new fabrication technique is described which enabled us to obtain an improved temperature performance for a 1.3μm QD laser.

The structure of a superluminescent light emitting diode is similar to a ridge waveguide laser; the main difference is that optical feedback is suppressed, in our case by the ridge being tilted with respect to the facet so as to suppress lasing. Superluminescence is obtained from the device due to amplified spontaneous emission as a result of the gain of the active region at high current. The main features of the superluminescent LED are the high output power *and* the broad emission bandwidth. Furthermore, the emission wavelength of interest is 1000-1300nm for application in optical coherence tomography (OCT). The introduction of a QW as the active region showed a promising increase in the emission bandwidth for a SLED compared to conventional bulk double heterostructure [19]. Lin *et al.* reported another technique to broaden the spectra, in which they employed multiple quantum wells of different width [20]. In late 90's some groups suggested QW intermixing for the low loss laser cavities. Later this technique was used to broaden the emission spectra of the broadband QW SLEDs [21]. In recent years QDs have drawn more attention as a potential SLED material for their naturally broad emission spectrum due to an inhomogeneity of ~10% in the dot size, and variation in indium composition of the self assembled quantum dots [22, 23, 24]. Several approaches were made in the last few years to widen the emission spectra of quantum dot superluminescent LEDs. One of those approaches was to increase the dot size distribution [21] but to date the exact control over the QD size is not possible and hence not reproducible. In Chapter 4 a novel technique is described which enabled us to engineer a broad emission spectrum

by combining the ground states and the excited states of "chirped" QD SLEDs emitting around 1300nm.

The other main issue for the SLEDs is the output power. Several methods have been used previously to increase the output power of a SLED. Methods like using a fiber power amplifier [25] or the combination of an edge emitting LED and a single transverse-mode semiconductor amplifier [26] or tapered optical semiconductor amplifier seeded by a SLED [27] were proposed to increase the output power of the SLED. In recent years some other techniques tapered waveguide has been used to increase the output power of the SLED structure. One group in recent years has reported an InGaAs QD SLED with 0.9W output power and 80nm Full Width at Half Maximum (FWHM), but the peak emission wavelength was around 1000nm [28]. Very recently another group has reported about InGaAs/InAs tilted ridge QD SLED operating in pulsed mode with high normalized output power of ~10mW at 10^0C and emitting around 1300nm [29].

1.3 Advantage of InAs/GaAs QD lasers and SLEDs

For fiber-optic communication system two wavelengths, 1.3μm and 1.55μm are most important wavelengths as they correspond to the minimum in dispersion and attenuation for standard single mode fiber, respectively. So it is important to achieve emission around 1.3μm from lasers. Conventionally lasers based on InGaAsP quaternary material lattice matched to InP for short and long haul communication. However this material system has some problems due to the small band offset and small refractive index differences. Also InP based telecommunication lasers require active cooling. The fabrication steps are also complicated for the integration and coupling to the optical fiber, which makes them very costly devices. These problems related to InP technology made the more mature and low cost GaAs technology attractive for this application. Devices based on the GaAs and AlGaAs offer the advantage of larger band offsets, which in turn offers carrier confinement and comparatively larger refractive index difference. This makes GaAs based devices more efficient for high temperature operation. Also by incorporating InGaAs QWs it has been possible to extend the emission wavelength to around 1.2μm. To extend the

emission wavelength further, two attractive techniques are being used nowadays. The first one is dilute nitride semiconductor as this material system can cover the fiber–optic communication wavelength and also offer good temperature performance due to the large confinement potential. However, significant development of the epitaxy of these materials is still required.

The alternative method is to use self assembled QDs as for this structure the emission wavelength can be extended by careful optimization of the growth condition. Previously to extend the emission wavelength of QD lasers to 1.3μm different methods like low growth rate (LGR) [30] or the atomic layer epitaxy (ALE) was used [31]. The problem related to both the techniques is low quantum dot density and hence low saturated gain. Another method adopted by some groups to reach the 1.3μm emission is to cover the InAs dots with InGaAs or alternatively to grow the dots within an InGaAs quantum well (QW) [31, 32, 33,]. The structure with InAs QDs in an InGaAs QW is popularly known as the "dot-in-well" (DWELL) structure.

For superluminescent LEDs emission around 1300nm is also important because for applications like OCT the deepest penetration into the tissues is achieved in between the wavelengths 1200nm and 1800nm [34, 35]. The QD material is preferred for SLEDs for this reason and also for the other advantages offered for the QD lasers. The self assembled InAs/GaAs QDs exhibit an inhomogeneously broadened emission and gain spectrum which can be problematic for QD lasers. However, this naturally broadened spectrum is advantageous for the SLEDs as one of the prerequisite for the SLED is the broad emission spectrum.

1.4 Growth of InAs QDs on GaAs

For QD structures, In(Ga)As dots formed on a GaAs layer have a number of advantages for long wavelength applications. The most widely employed technology so far for growing QDs is the Stranski-Krastanov growth method. In this method self-assembled QDs can be grown which individually display a near singular density of states. The variation in size and composition of the ensemble of QDs leads to a broad emission band. The main advantage of this growth technique is the control over the

size and density of the QDs changing the growth temperature, growth rate and the flux of the reactant gasses.

Under Stranski–Krastanov growth mode, the formation of quantum dots is driven by strain (lattice mismatch of ~7%) during the epitaxial growth of InAs dots on a GaAs substrate. Typically a thin wetting layer (WL) is formed when the amount of deposited material does not exceed a critical value of 1-2 monolayers [36]. Deposition of additional materials results in the formation of 3D islands. This allows the relaxation of elastic energy compared to a two dimensional layer. The strain is relieved elastically without introduction of crystal defects, which is key to the high optical quality of these QDs. The dot size, areal density, and optical properties depend on the growth parameters, such as growth temperature, growth rate, and III-V ratio. If the growth condition is inappropriate or too much material is deposited large dislocated islands may appear locally or islands may coalesce creating defects [36, 37]. The size of the quantum dots can be controlled over a reasonable range by varying the deposition rate and/or growth temperature.

For application in laser devices, the self assembled In(Ga)As QDs on GaAs has importance because of their potential for optical fibre communication in the wavelength range 1.3μm to 1.6μm. However QD lasers with single layer QDs at the active region exhibit a low maximum modal gain, especially at the above mentioned wavelength range [38, 39]. In order to achieve sufficient modal gain for ground state lasing, multiple QD layers are needed in the active region of the QD lasers.

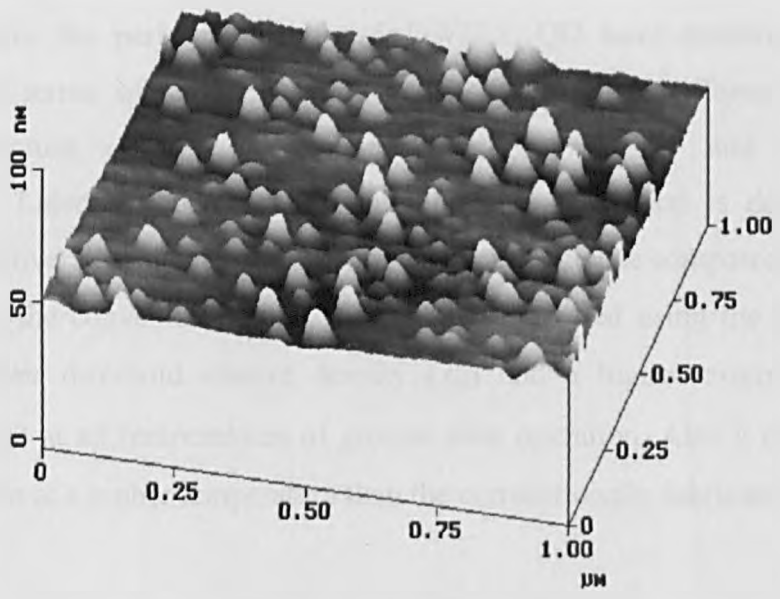

Fig.1.2 Atomic Force Microscopic image of the uncapped InAs QDs grown on GaAs

Stacking of multiple layers too close together may give rise to defect formation due to the strain formed by the deposited material. In order to get rid of those, several groups suggested different solutions. Strain compensation [40, 41] or removals of the largest dots by selective evaporation [42] are a few of those solutions. The incorporation of a high growth temperature spacer layer in between the QD layers has been proposed by researchers in Sheffield, who demonstrated a significant enhancement in the characteristics of 1.3μm QD lasers [43, 44].

1.5 Outline of the thesis

1.5.1 Chapter 2: Growth, Device fabrication and Experimental Techniques

In this chapter the detailed growth for the QD material and the fabrication of narrow stripe lasers, broad area lasers, mesa diode and the SLEDs is described. Subsequently the electrical and optical characterization methods for all the above-mentioned devices are detailed. Also, some technical development issues, relevant to the experimental results described later are discussed. The results obtained from different characterization techniques are laid out in the following chapters.

1.5.2 Chapter 3: Improved device fabrication for 1.3μm Quantum Dot Lasers

In this chapter the performance of a 5xDWELL QD laser emitting at 1.3μm is described in terms of threshold current density, external differential efficiency, internal quantum efficiency, transparency current density and characteristics temperature. Later in this chapter a new fabrication method is described which improves the overall temperature characteristics of the device compared to the devices fabricated in the conventional way. The device fabricated using the new technique shows a lower threshold current density (J_{th}) and a higher external differential efficiency (η_d) at all temperatures of ground state operation. Also it exhibits ground state operation at a higher temperature than the conventionally fabricated device.

1.5.3 Chapter 4: 1.3μm InAs/GaAs Quantum Dot Superluminescent Light Emitting Diode

This chapter outlines a new method of broadening the emission spectra of a 5xDWELL QD superluminescent LED operating around 1.3μm. Compared to the conventional 5xDWELL SLED this device exhibit a broader emission spectra and a moderate output power at room temperature. An epitaxial layer design is employed in order to obtain a structure in which both the ground state and the excited state emission from different wells in the active region overlap to exhibit a broad almost flat topped emission spectrum. Characterizing narrow stripe lasers fabricated from these two types of materials also exhibits the overlapping of the ground state and the excited states. Later in this chapter, results from a modified version of this broad band SLED is discussed which shows further broadening of the emission spectra with a flat top, emitting in the 1200-1300nm range.

1.5.4 Chapter 5: Molecular Beam Epitaxy grown High Power Superluminescent Light Emitting Diode

A new growth mechanism to increase the output power of a narrow band QD SLED is described in this chapter. The SLEDs fabricated from this new material exhibit a dramatic increase in output power. The laser devices made from this new material also show a remarkable reduction in the threshold current density and an increase in external differential efficiency. Electrical characterization of the mesa diodes made from this new material indicates improved quality of the new material due to a decrease in the defect density. The details of the growth mechanism and the origin of the improved device performance are then discussed.

1.5.5 Chapter 6: Conclusion

Different issues raised in all the chapters are discussed in detail in chapter 6. Also the problems faced during the experiments and different ways to overcome those problems are outlined. Future plans for the further improvement in the device performance and the experimenting methods are also discussed in this chapter.

References

[1] J. H. Davies, "The Physics of Low dimensional Semiconductor", Cambridge University Press (1998).

[2] Z. I. Alferov, V. M. Andreev, E. L. Portnoi, M. K. Trukam. Fiz-Tekn. Pol 3, 1328, (1969).

[3] Z. I. Alferov, V. M. Andreev, D. Z. Garbuzov, Y. V. Zhilyaev, E. P. Morozov, E. L. Portnoi, V. G. Trofin. Fiz-Tekn. Pol 4, 1826, (1970).

[4] Y. Arakawa and H. Sakaki, Appl. Phys. Lett. 40, 939 (1982).

[5] H. Sakaki, Y. Arakawa, M. Nishioka, J. Yoshina, H. Okamoto, N. Miura, Appl. Phys. Lett. 46, 83 (1985).

[6] M. Asada, IEEE J. Quantum Elect. 3, 196 (1986).

[7] 'Quantum Dot Heterostructure' D. Bimberg, M. Grundmann, N. N. Ledentsov; J. Wiley and sons Ltd. (London 1998).

[8] H. Hirayama, K. Matsunaga, M. Asada, Y. Suematsu, Elect. Lett. 30, 142 (1994).

[9] N. Kirstaedter, N. N. Ledentsov, M. Grundmann, D. Bimberg, V. M. Ustinov, S. S. Ruvinov, M. V. Maximov, P. S. Kop'ev, Z. I. Alferov, U. Richter, P. Werner, U. Gosele, J. Heydenreich, Elect. Lett. 30, 1416 (1994).

[10] D. J. Mowbray, L. Harris, M. S. Skolnick, A. D. Ashmore, D. C. Brenchley, Proc. Semi. Sci. and Tech. La Jolla, California, USA (1998).

[11] H. Shoji, K. Mukai, N. Ohtsuka, M. Sugawara, T. Uchida, H. Ishikawa, IEEE Photon. Technol. Lett. 7, 1374 (1995).

[12] A. E. Zhokov, A. R. Kovsh, N. A. Maleev, S. S. Mikhrin, V. M. Ustinov, A. F. Tsatsul'nikov, M. V. Maximov, B. V. Volovik, Y. M. Shernyakov, P. S. Kop'ev, Z. I. Alferov, N. N. Ledentsov, D. Bimberg, Appl. Phys. Lett. 75, 1926 (1999).

[13] G. T. Liu, A. Stintz, H. Li, T. C. Newell, A. L. Gray, P. M. Varangis, K. J. Malloy, L. F. Lester. IEEE J. Quantum Elect. 36, 1272, (2000).

[14] G. Park, O. B. Shchekin, D. L. Huffaker, D. G. Deppe, IEEE Photon. Technol. Lett. 13, 230 (2000).

[15] O. B. Shchekin, J. Ahn, D. G. Deppe, Elect. Lett. 38, 712 (2003).

[16] 'Quantum Wells, Wires and Dots' P. Harrison, J. Wiley & sons Ltd. (2000).

[17] G. Liu, A. Stintz, H. Li, L. F. Lester, K. J. Malloy. Elect. Lett. 35, 1163, (1999).

[18] S. Fathpour, Z. Mi, S. Chakraborty, P. Bhattacharya, A. R. Kovsh, S. S. Mikhrin, I. L. Krestnikov, A. V. Kozhukhov, N. N. Ledentsov, 62nd Device Research Conference Digest IEEE, New York, 156-157, (2004).

[19] T. R. Cheng, Y. H. Eng, A. Yariv, N. S. Kwong, P. C. Chen, Appl. Phys. Lett. 56 1345, (1990).

[20] C. -F. Lin, B. -L. Lee, P. -C. Lin, IEEE Photonics. Technol. Lett. 8, 1456, (1996).

[21] S. D. McDougall, O. P. Kowalski, J.H. Marsh, J. H. Aitchison, IEEE Photon. Technol. Lett. Vol 11, No.12, 1557-1559, (1999).

[22] D.C. Heo, J.D. Song, W.J. Choi, J.I. Lee, J.C. Jung, I. K. Han , Electron. Lett. 39 (11), (2003).

[23] Z.Y. Zhang, Z.G. Wang, X.P. Jin, Z. Z. Sun, F.Q. Liu, IEEE Photonics. Technol. Lett. 16, (1), 27-29, (2004).

[24] M. Rosseti, A. Markus, A. Fiore, L. Occhi, C. Velez, IEEE Photonics. Technol. Lett. Vol. 17, No. 3, 540-542 (2005).

[25] N. S. Kwong, IEEE Photon. Technol. Lett.4, 9, 996-999, (1992).

[26] K. Y. Liou and G. Raybon, IEEE Photon. Technol. Lett. 7, 1025-1027, (1995).

[27] L. Goldberg and D. Mehuys, Electron. Lett. 30, 1682-1684, (1994).

[28] D.C. Heo, J.D. Song, W.J. Choi, J.I. Lee, J.C. Jung, I. K. Han Electron. Lett. 39 (11), (2003).

[29] M. Rosseti, A. Markus, A. Fiore, L. Occhi, C. Velez, IEEE Photonics. Technol.. Lett. Vol. 17, No. 3, 540-542 (2005).

[30] P. B. Joyce, T. J. Krzyzewski, G. R. Bell, T. S. Jones, S. Mali, D. T. Childs, R. Murray, Phys Rev. B. 62, 10891 (2000).

[31] K. Nishi, H. saito, S. Sugou, J-S Lee, Appl. Phys. Lett, 74, 1111 (1999).

[32] A. E. Zhukov, A. R. Kovsh, A. Yu Egorov, N. A. Maleev, V. M. Ustinov, B. V. Volvik, M. V. Maximov, A. F. Tsatsul'nikov, N.N. Ledentsov, Yu. M. Shernyakov, A. V. Lunev, Yu. G. Musikhin, N. A. Bert, P. S. Kop'ev, Zh .I. Alferov, Semiconductors 33, 153 (1999).

[33] L. F. Lester, A. Stintz, H. Li, T. C. Newell, E. A. Pease, B. A. Fuchs,K. J. Malloy, IEEE Phot. Tech. Lett. Vol 11, 931, (1999).

[34] J. G. Fujimoto, M. E. Brezinski, G. J. Tearney, S. A. Boppart, B. E. Bouma, M. R. Hee, J. F. Southern, E. A. Swanson, Nature Med, vol 1, 970-972, (1995).

[35] B. E. Bouma, L. E. Nelso, G. J. Tearney, D. J. Jones, M. E. Brezinski, J. G. Fujimoto, J. Biomed. Opt, vol 3, 76-79, (1998).

[36] D.Bimberg, M. Grundmann, N.N.Ledentsov; MRS Bulletin Feb. Vol. 23 (2) (1998).

[37] X. Chen, A. Markus, A. Fiore, U. Oesterle, R. P. Stanley, J. F. Carlin, R. Houdre, M. Ilegems L. Lazzarini , L. NasiM. T. Todaro, E. Piscopiello, R. Cingolani, M. Catalano, J. Katcki and J. Ratajczak; Jrnl. of App. Physics Vol. 91, no 10, 15 may (2002).

[38] N. N. Ledenstov, M. Grundmann, F. Heinrichsdorff, D. Bimberg, V. M. Ustinov, A. E. Zhukobv, M. V. Maximov, Z. I. Alferov, J. A. Lott, IEEE J. Sel. Topics quantum Electron, vol. 6, no. 3, 439-451 (2000).

[39] P. M. Smowton, E. J. Pearce, J. Lutti, D. R. Mathews, H. D. Summers, G. M. Lewis, P. Blood, M. Hopkinson, A. B. Krysa, Novel In plane Semiconductor Lasers III, Proc. Society of Photo-Optical Instrumrntation Engineers (SPIE) vol. 5365, 86-95, May, (2004).

[40] X. Q. Zhang, S. Ganapathy, I. Suemune, H. Kumano, K. Uesagi, Y. Nabetani, T. Matsumoto, Appl. Phys. Lett., vol 83, 4524-4526, (2003).

[41] P. Lever, H. H. tan, C. Jagadish, J. Appl. Phys. Vol 95, 5710-5714, (2004).

[42] N. N. Ledenstov, "Semiconductor Device and Method of Making Same" U. S. patent 6 653 166, (2003).

[43] H. Y. Liu, I. R. Sellers, T. J. badcock, D. J. Mowbray, M. S. Skolnick, K. M. Groom, M. Gutierrez, M. Hopkinson, J. S. Ng, J. P. R. David, R. Beanland, Appl. Phys. Lett. Vol 85, 704-706, (2004).

[44] H. Y. Liu, I. R. Sellers, M. Gutierrez, K. M. Groom, W. M. Soong, M. Hopkinson, J. P. R. David, R. Beanland, T. J. badcock, D. J. Mowbray, M. S. Skolnick, J. Appl. Phys., vol 96, 1988-1992, (2004).

Chapter 2: Wafer Growth, Device Fabrication and Experimental Techniques

2.1 Introduction

This chapter describes the various experimental techniques used during this project. Firstly, the growth of samples by molecular beam epitaxy (MBE) is described. Fabrication techniques for the preparation of narrow stripe lasers, superluminescent LEDs, broad area lasers and mesa diodes are then described in detail together with some useful experimental observations arising during the fabrication of such devices. Finally a review of the various experimental techniques used for characterisation of the epitaxial material and the fabricated devices are described.

2.2 Growth of samples using Molecular Beam Epitaxy

A solid-source VG Semicon V90H molecular beam epitaxy (MBE) system was used to grow the Quantum Dot structures. MBE growth is preferred MOVPE for the epitaxial growth of QD structures, the main attribute being the in-situ monitoring of the growth of the QDs by RHEED (Reflection High Energy Electron Defraction) allowing observation of the transition from 2D to 3D growth. A MBE reactor consists of a number of ultra high vacuum chambers, connected by interlocks, which prevent the chamber from contamination during loading and removal of the wafer. The samples were grown on Si doped GaAs (100) substrates by either Dr Hui-Yun Liu or Dr Mark Hopkinson. The substrate is held on a heated molybdenum block. The block rotates with the substrate to improve the uniformity of deposition. Several cells (Knudsen Cells) in the system contain the elemental sources required for the growth of III-V semiconductors, and for the different dopant species. The deposition rate is controlled by the temperature of the cells and a mechanical shutter, attached at the exit of each cell, is used to switch on/off the flux of the source. The atomic flux from each cell is directed to the substrate and forms the required semiconductor upon the

substrate. Due to the slow growth rate and fast shutter switching time it is possible to produce multi-layer structures with an atomically flat surface.

The active regions of the samples studied here consist of quantum dots (QD) grown within the quantum wells (QW). The QDs are formed in the wells using the Stranski-Krastanow [1] growth mechanism. In this work the InAs QDs are formed on GaAs or on InGaAs. The lattice mismatch between GaAs and InAs is ~7%. So during the growth of InAs on GaAs a strain field is produced and after deposition of some critical thickness of InAs, ~1.6 monolayers (ML) of InAs, 3D indium-rich clusters are formed on the GaAs. This method is described more elaborately in the chapter 1. The active region design for the QD lasers and QD SLEDs studied here is popularly known as the dot-in-well (DWELL) structure. During the deposition of the DWELL 3MLs of InAs is deposited on 2nm of $In_{0.15}Ga_{0.85}As$ and capped by 6nm of $In_{0.15}Ga_{0.85}As$. This combination of InAs deposition thickness and quantum well combination has been previously shown to optimise the optoelectronic properties of 1.3μm QD lasers [2]. There are several alternative approaches for the growth of InAs QDs on GaAs or InGaAs for emission at 1.3μm. One of them is to grow the QDs at an ultra low growth rate (<0.02ML/s) [3], in order to increase the dot size and hence the emission wavelength. However, for the devices studied here, the QDs are grown at a higher growth rate (0.092ML/s) in conjunction with continuous InAs deposition, with the long wavelength emission a result of the large amount of indium available for QD growth from the InGaAs QW. This gives improved QD density ensuring a high gain and high optical quality of the 1.3μm laser [2]. The DWELLs are separated by a GaAs spacer layer. In most of the devices studied here the GaAs spacer layer has a width of 50nm. Following the deposition of each DWELL, the initial 15nm of the GaAs spacer layer was deposited at 510°C, following which the temperature was increased to 580°C for the remaining 35nm of GaAs. The temperature was then decreased back to 510°C for the growth of the next DWELL. In the later part of this project the elevated temperature used during the deposition of the final 35nm of the GaAs spacer layer was increased to 620^0C. This resulted in improved performance and ground state emission being observed for lasers of shorter lengths. Additionally, the thickness of the low growth temperature layer was changed and compared for high power SLEDs. This is discussed in chapter 5. It has been observed that the indium content of QDs is not uniform and strongly depends on the indium content of the underlying wetting

layer (WL) [4]. The QDs are also strongly affected by choice of capping material used to cover them. When QDs are capped by GaAs their properties change due to In-Ga intermixing and segregation of indium from the QDs. This leads to smaller confining potentials which results in a shorter emission wavelength. The detailed growth mechanism of the complete device will be discussed in subsequent chapters.

2.3 Device fabrication

During this project different device structures were fabricated. Besides narrow ridge lasers and SLEDs, mesa diodes were also fabricated in order to observe the electrical characteristics of the material. Broad area lasers were also fabricated, chiefly to gain an appreciation of the material performance before lengthier, complete fabrication of the narrow ridge lasers or superluminescent LEDs was performed. The results from broad area lasers accurately provided device performance parameters such as threshold current density (J_{th}), internal loss (α_i), internal efficiency (η_i) since they are less sensitive to process-induced damage than narrow ridge devices. However due to their large size and associated high operating currents, temperature dependent measurements are generally performed on narrow ridge devices. Suitable sets of samples were chosen to fabricate lasers or SLEDs for comparative studies after first obtaining successful performance from the broad area lasers. Later in this chapter the complete fabrication steps required for tilted ridge SLEDs are described.

2.3.1 Laser fabrication

The complete fabrication process for narrow stripe lasers is described in the following paragraphs. Fabrication process for other devices will be described with reference to this laser fabrication method.

2.3.1.1 Nomenclature and cleaning the sample

Since multiple fabrication runs are required for each wafer for experimental purposes, generally a quarter of a 2" or 3" wafer is taken to start with. At the corner of each

piece the sample number is scribed with a diamond-tip scriber so as to recognize the sample after processing. Samples are then cleaned using a three step cleaning process to ensure all the dust and debris removed. The sample is first placed into a beaker of n-butyl acetate and boiled for approximately 30 seconds. This ensures the removal of all types of grease. After boiling the sample it was placed on a clean filter paper and cotton buds were used to remove the remaining dust and debris. The sample was then dried using a nitrogen gun and placed into a beaker of acetone. The sample was agitated in the warm acetone before being placed in a beaker of warm Isopropyl alcohol and agitated for few seconds. After removing the sample from the beaker it was dried thoroughly using a nitrogen gun and inspected under a microscope. The process was repeated until a cleanliness of $\leq$ 1 particle per field of view of 50X magnification was observed. The existence of dust or dirt can prevent good adhesion of deposited metals.

2.3.1.2 Photolithography for definition of p^+ ohmic contact

This step of the device fabrication was performed in the yellow room as it ensures that only the areas exposed to the UV radiation from the Karl-Suss (MJB-3) mask-aligner is modified. To prevent tweezer damage to the surface of the samples, sample smaller than a ¼ wafer were mounted on a thin glass slide to act as a carrier. To do this a thin glass slide was placed on a hot plate and a thin layer of wax was melted on top of the slide. The sample was then placed upon the slide with the top surface facing upwards and the other side adhered to the glass slide with wax. The sample is pre baked at 100^0C. This pre baking removes any solvents remaining from the preparatory cleaning steps. A positive photoresist (BPRS200) is then spun on to the sample at 4000rpm for 30 seconds to ensure a uniform layer of photoresist is formed upon the sample surface. Photoresist is then soft baked at 100^0C for 1 minute to remove solvent from the resist.

The sample is then placed on the stage of the mask aligner and covered up by Molybdenum sheets keeping the sides of the sample open and exposed for 30 seconds. This step is carried out to remove the thick photoresist beads that occur at the edges of the sample, known as 'edge bead removal'. To remove this resist the sample edges are exposed to the UV light for a time approximately 3 times that of the standard

exposure time for the normal thickness resist. After the exposure the sample was then developed in a 1:3 H_2O: Developer for 1min.

The mask used for definition of the contact stripes contains 5μm and 15μm wide stripes and some additional circular features for electrical measurements. The mask is first thoroughly cleaned using Acetone and IPA to ensure there is no stale photoresist on it, which may remain from contact lithography of previous samples. A cleaved edge of the sample is then aligned with the mask so that stripes run along the crystal orientation. The resist is then exposed under UV light for 15 seconds. After exposure the sample is agitated in the positive photoresist developer for 1 minute. The sample is then rinsed in flowing deionised water (DIW) and dried with a N_2 gun. Prior to metallisation the sample is placed in an O_2 plasma asher for ~1min. to remove any photoresist that may remain in the exposed/developed stripes. Any photoresist remnant would be deleterious to metal adhesion and/or cause series resistance.

2.3.1.3 Metallisation of the p-type ohmic contact

To form an ohmic contact to the p-type GaAs Au-Zn-Au (5nm-10nm-200nm) is used. The constituent metals in the thermal evaporation (BOC Edwards thermal evaporator) metals Au (20mg) and Zn (20mg) are first boiled in n-butyl acetate to degrease. The metals are then placed in Tungsten coils. Prior to loading, the samples are placed in a 19:1 H_20:NH_3 solution for 20seconds and dried in order to remove native surface oxides. The sample is then placed in the evaporator near to the crystal detector of a thickness monitoring system. The Zn coil and the Au coil are placed at distances of 6cm from the sample and a vacuum of ~10^{-6} mB is applied. Initially a thin (5nm) Au layer is deposited, before 10nm of Zn is deposited on top. This thin Au layer improves the adhesion of the Zn. Finally ~200 nm of Au is deposited. The thickness is measured with a crystal monitor to within ±5nm. After deposition of the metals the sample is then allowed to cool down for 10 minutes before being removed from the vacuum. The sample is then placed into a beaker containing acetone for a process known as "lift-off". During lift-off the photoresist underneath the metal is dissolved in acetone, lifting off the metal, and leaving well defined metal contacts on the ridges and other required portions. Upon inspection under the microscope, if some metal is adhered to the semiconductor between stripes, the sample may be placed in an

ultrasonic bath to aid removal of any erroneous metal. The samples are then cleaned using the usual three-step cleaning process and annealed in the rapid thermal annealer at 360^0C in order to drive Zn into upper semiconductor layer and reduce the metal/semiconductor barrier height, thus reducing the voltage drop across the contacts.

2.3.1.4 Photolithography for the ridge etching

The sample is then patterned again for the ridge etch. During this photolithographic process the mask named RIDGES is used. BPRS200 is spun and baked. The edge beads are removed as before. The second mask layer is aligned to alignment marks defined in the first stage lithography and exposed to the UV light for 15 seconds. After developing the sample for 1 min it is inspected under the microscope. If the lithography is good the resist is given a hard bake at 100^0C for 1min to create a durable coating on the upper surface of the photoresist and the sample is taken for the ridge etch.

2.3.1.5 Dry and wet chemical etching

A) Dry etching using Inductive Coupled Plasma etching technique

Inductively Coupled Plasma (ICP) etching technique is used to etch the ridges. ICP etching is a plasma source in which energy is created by the electric current which is produced by electromagnetic induction. A time varying electric field is passed through a coil, which produces a time varying magnetic, filed. This magnetic field induces an azimuthal electric current in the selected gas and after breakdown it creates plasma. In order to etch GaAs $SiCl_4$ is used. The main advantage of the ICP technique is the well-defined ridge profile of the laser structure. The ICP technique is generally used for etching high aspect ratio, smooth vertical profiles with lower DC bias than reactive ion etching technique, resulting in lower damage. Wet chemical etching can not accurately transfer the mask pattern to semiconductor for small features and can not also produce a uniform ridge profile if etched deep.

The patterned samples are loaded in the ICP etcher. The deep etched laser ridges discussed in chapter 3 were etched to a depth of ~3.2μm completely through the active region. This deep etch improves the optical confinement of the mode. However etching through the active region of the laser produces rough sidewalls, which increases optical loss. Also, it contributes to the electrical loss through the formation of the non-radiative recombination centers along it. It is predicted that such recombination centers are less significant in QD structures compared to QW or bulk because of the 3D localization of carriers within dots and corresponding reduced mobility in the growth plane.

B) Wet chemical etching

The ridges of most of the devices discussed in this thesis are formed by wet chemical etching. A variation of the well known 1:1:1 chemical etchant is used. In this etchant a mixture of one portion (~6ml) of Hydrobromic acid, one portion of Acetic acid and one portion of Potassium Dichromate solution is used (HBr: CH_3COOH: $K_2Cr_2O_7$). The etch rate of this solution at room temperature is ~4μm/min and the etching is isotropic. In order to gain good controllability of the etch depth rate 50% Potassium Dichromate and 50% deionised water was mixed with HBr and CH_3COOH solution. With this solution a precise control over the etching depth is achieved, allowing etching depth of 1.8μm with ±100nm precision. The patterned sample is submerged into the solution and agitated gently and uniformly for about 30 seconds initially. The etch depth is then measured under the surface profilometer (Dektak). The process of etch and measurement is repeated until the required etching depth is achieved. The non uniformity of the etch depth along the ridge is ~. 05μm. The standard etch depth of most of the laser and SLED devices are 1.7-1.8μm, corresponding to stopping the etch after removal of the p-doped upper cladding layer only.

2.3.1.6 Deposition of the SiN_x isolation layer

After the etching process the samples are coated with a dielectric layer. The width of the laser ridges are 5, 8, 10, 15 or 20μm depending on the mask used. For such narrow ridge widths direct bonding to the ridges is difficult, (as the ball bond diameter is ~70μm) so a dielectric layer is deposited so as to allow the deposition of large

bondpads, isolated from the etched region of semiconductor, and contacting only the p-type material at the top of the ridge. Hence this layer eliminates the problem of short circuits. Dielectric coating of laser ridges has also the advantage of passivating the etched sidewalls by tying up dangling bonds.

Before deposition of the dielectric (Si_3N_4) the sample is solvent cleaned to remove the photoresist from the previous step. The sample is also prepared in a 19:1 H_20-NH_3 solution to deoxidise the sample surface and then 500nm of Silicon nitride is deposited on the sample, via plasma enhanced chemical vapour deposition (PECVD). In this step a recipe, 'SIN500' is used which deposits 500nm of Si_3N_4 is deposited on the sample. The total process takes about 1 hour. In PECVD a good step coverage is obtained. A good step coverage means that an almost homogeneous thickness of SiN coats all exposed surfaces of the sample. In order for the bondpad to contact to the p-doped metallisation above the laser ridge, a window must be opened in the dielectric region.

2.3.1.7 Photolithography to open a window on the ridge

Photolithographic steps are carried out to open a window in the dielectric layer on the top of the ridge. The same positive photoresist (BPRS200) is spun on the sample, and prepared as before (Sec 2.3.1.2). The sample is properly aligned and exposed for about 20 seconds. This exposure time is ~ 20% higher than before, to compensate for absorption of the light by the dielectric layer. After developing and inspection a hard bake for 1 min. is given, to make the resist more resistant to the etching process.

2.3.1.8 Opening a window on top of the dielectric using Reactive Ion Etching

The patterned sample is then put in the reactive ion etching (RIE) system. In a typical RIE system the sample is placed in a cylindrical chamber. Vacuum is created in the chamber and the gas flow rates are set. The gasses used for this process are O_2 and CHF_3 and the flow rates are set to 5sccm and 35sccm respectively. As the RIE process and the etching rate strongly depend on the RF power applied, it is important to set the applied RF power to an optimum value, using higher values may cause a deeper etch. Monitoring the previous etching results of the system provides suitable calibration to

allow an etch time to be selected. The RF power is typically set at 60W. The sample is then etched for approximately 12 minutes until the Si_3N_4 is removed. After etching the sample is checked under a microscope to ensure that the dielectric is completely removed from the ridges.

2.3.1.9 Removing the photo resist

After opening a window on top of the ridge the bondpad is to be deposited. To ensure that the bondpad will adhere to the sample the remnant of the photoresist must be removed. During the CHF_3 chemistry, the photoresist becomes very hard and resistant to standard acetone cleaning. The sample is placed in the O_2 plasma asher for ~10 minutes. If still some resist remains, the sample is placed in a glass container with some resist stripper in it. The sample is then placed and agitated gently on a hot plate. When fumes start to come out of the container it is removed from the hot plate. The sample is then rinsed well in DI water, dried and then given a general clean using the three cleaning steps, before inspection.

2.3.1.10 Photolithography for the bondpads

The photolithographic steps are then carried out for the bondpad formation. The same BPRS200 photoresist is used. The exposure time is 2.5 times the standard exposure time. This will ensure that photoresist located at the foot of the laser ridge (where it is more difficult to expose, and may be thicker) is well exposed. Any resist under the metal will lead to device failure. It is a good practice to put the sample in the plasma asher for 1-1.5 mins to make sure there is no photoresist left along the ridges. Otherwise if some phototoresist remains underneath, wire bonding to the bondpads will be affected. In worst case it may not be possible to bond because the gold may peal off during the bonding process.

2.3.1.11 Deposition of the top bondpads

For thermal evaporation of Ti:Au bondpads, the constituent metals are degreased then placed 12cm and 6cm away from the sample respectively. One piece of Au and Ti is positioned at either side of the sample to make the metal deposition up the side- wall

of the ridge even. 15nm of Ti, which is used to aid gold adhesion, is deposited from each side and then 200nm of Au is deposited from each side. Lift off is performed in acetone to reveal the bondpad features. Since the evaporation was done from both sides of the ridge, there is a risk that acetone may not easily reach the photoresist since lift-off relies upon a gap between the semiconductor surface and the top of the photoresist, resulting from directional evaporation from above. In the worse case an ultrasonic bath is used to assist in lift off of the unnecessary metals. The sample is cleaned and then annealed at 340^0C for 1 min.

2.3.1.12 Photolithography for electroplating and selective electroplating

Photolithographic steps are carried out for electroplating the gold bond-pads. The same photoresist is used and the exposure time remains the same for this step. The purpose of electroplating is to provide a better heat sink to the sample, and to ensure sufficiently thick gold contact that will not 'blow' at high voltage or temperature. The general gold evaporation or the e-beam evaporation technique is not chosen for this purpose because electroplating several microns of gold is cheaper than evaporating large amounts of gold. Also, a thicker gold layer (~3.2μm) can be deposited on the semiconductor surface by electroplating at a higher uniformity, with good step coverage (*ie.* thick metal on side of the ridges).

For electroplating the exposed area of the sample is roughly calculated to determine the drive current through the electrodes. The area covered by the photo resist is not considered for electroplating. Care is taken to select the drive current. If the drive current is too high, it may result in porous gold deposited on the surface of the semiconductor. This porous gold has a poor conductivity and the wire bonding may not adhere to the bond pads.

2.3.1.13 Thinning the sample

Before the deposition of the back contact the sample is thinned so that it can be cleaved properly and to aid in heat sinking. Initially, two layers of thick photoresist are spun on the top surface of the sample to prevent any damage to the sample during mounting and demounting. Two layers of BPRS200 are deposited and the sample is given a hard bake at 100^0C for 2min. Then a cylindrical metal block is taken and

placed on the hot plate. Then the sample is then mounted on the block with the top surface of the sample adhered to the block surface with wax. The thickness of the sample is measured. Three different diamond grits were used for polishing. Initially, the sample is simply *ground away* using the 9μm grit and finally fine polishing was achieved using the 3μm and 1μm grit. The thickness of the thinned sample is in the range of 150-180μm. When the process is complete the sample is cleaned with DIW and is de-mounted on a hot plate. The sample is then cleaned properly using the three step cleaning process and is ready for the evaporation of the back contact metal.

2.3.1.14 Evaporation of the back contact

An InGe-Au back contact is applied to the samples. The sample is first rinsed for 20 seconds in the 19:1 Ammonium solution prior to the deposition. This is done to remove the oxide formed on the semiconductor surface as a result of the contact with the atmospheric oxygen. Removal of the oxides ensures good contact between semiconductor and the metal. After that the sample is placed in the evaporator and 20nm of InGe is deposited followed by 200nm of gold. The annealing temperature for this contact is ideally 420^0C but the sample is annealed at a lower temperature at 340^0C, since the annealing temperature for the front contact was only 360^0C and annealing at a higher temperature may cause the Ti in the bondpad to delaminate from the SiN. Although this is not the ideal contact, it still appears ohmic, with low contact resistance as a result of the high doping concentration in the substrate.

2.3.1.15 Cleaving the sample

As the characterization of the lasers involves length dependent determination of external differential efficiency or transparency current density, it needs to be cleaved in to different lengths. Generally the laser samples are cleaved in to 4, 3, 2.5, 2, 1.5, 1 and .5mm lengths.

2.3.1.16 Mounting the sample on ceramic tile

The narrow stripe lasers are mounted on ceramic (AlO_2) tiles. Eutectic InPbAg in the form of balls within a flux is used to bond the sample to the gold on the ceramic tile.

The sample is placed on a hotplate at 100^0C for half minute and then transferred to a hot plate at 180^0C for 10-15 seconds to create the eutectic bond.

2.3.1.17 Wire bonding

The temperature of the sample workholder is set to 90^0C, and gold wire is used to connect a bond pad of a ridge to a gold lead of the ceramic tile, which the current may be injected to the p-type top contact of the device. Approximately 1 wire is ball-bonded for every ½ mm length of the ridge.

2.3.2 Superluminescent LED fabrication

The superluminescent LEDs were fabricated in a similar manner to the narrow stripe lasers. In the following sections the differences in fabrication steps between SLEDs and the standard laser ridge described above will be described.

2.3.2.1 Photolithography for top p-contact (SLED)

For the SLED devices the ridges must be tilted so that the regenerative feedback from the facets is suppressed to prevent it from lasing. The mask was designed in such a way that aligning the edge of the sample with some specific marks on the mask, results in the ridges being tilted by 8^0 to the normal of the facet so as to suppress the regenerative feedback.

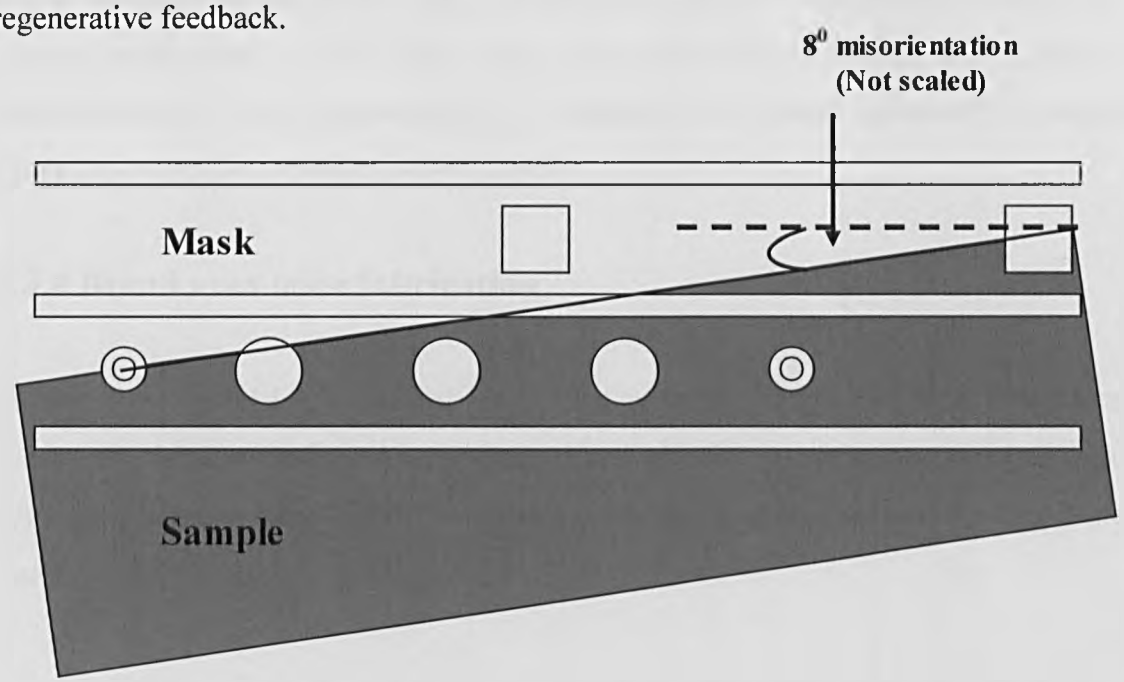

Fig. 2.1 Schematic of the position of mask and the sample is shown, which gives an 8^0 misorientation of the ridge to the normal of the facet of the SLED

2.3.2.2 Selective electroplating of the ridges

Investigations on the electroplated gold thickness were performed during the fabrication of the SLEDs. Initially ~3μm gold was deposited on the SLED (as was the case for ridge lasers) and it was observed that some gold flaps cover the facet after cleaving, as a consequence of the tilted ridge of the SLEDs. Therefore for subsequent SLED devices only ~1μm of gold was deposited.

The SLED devices are cleaved into 6mm, 8mm and 12mm long cavities. The 6mm long device is chosen to be the shortest cavity for the SLEDs because it was observed that for the 8^0 tilted ridges the ground state superluminescent emission is observed for a length 3 times longer than the shortest laser cavity to lase from the ground state. For most of the DWELL laser devices characterized in this project, it was observed that 2mm long cavities are the shortest cavities to lase from the ground state. It was observed that the SLED cavities shorter than 6mm could not achieve the required gain to demonstrate superluminescence from the ground state.

2.3.3 Mesa diode fabrication

Circular mesa diodes were fabricated in parallel with the lasers and SLEDs. Such mesas are useful for on wafer testing of electrical properties. The diameter of the mesa diodes incorporated in the mask design was 50μm and 100μm, and electrical characterization was performed as a function of device geometry. During characterization the mesa are probed directly.

2.3.4 Broad area laser fabrication

To obtain an initial impression of the optical properties of the material broad area lasers are fabricated. Broad area lasers are simpler to fabricate compared to fabricating narrow ridge lasers. Fewer steps are required to fabricate the broad are lasers.

2.3.4.1 Defining stripe contact

After cleaving and cleaning, the samples are prepared for contact lithography. BPRS-100, a positive photoresist is spun on the sample after a hard bake of 1min. The mask set used for defining the stripe contact has 100, 50 and 20μm wide ridge features. 3.5 sec exposure time and 1 min developing time was used for the photolithographic process.

2.3.4.2 Metallization for the p-type contact

The sample is deoxidized in 19:1 H_2O/NH_3 solution. The standard Au-Zn-Au (5nm-10nm-200nm) p-contact was deposited and annealed at 360^0C for 1min.

2.3.4.3 Photolithography for ridge etching

Photolithographic steps for the ridge etch are carried out with BPRS-200 photoresist. In this step a thicker (~2μm) photoresist is used as during the wet chemical etching so as to get over the tops of the features. For this step a thinner resist like BPRS100 also can be used. The exposure time is 6.5 seconds for BPRS200 while the developing time remained same. The sample is hard baked for 1min prior to the wet etching.

2.3.4.4 Wet chemical etching

A wet chemical etch is performed using the same 1:1:1 (HBr: CH_3COOH: $K_2Cr_2O_7$) etching solution. Again to control the etch rate a potassium dichromate is 50% diluted with DI water. Again the etch depth was maintained at around 1.8μm removing just the top p-doped GaAs and AlGaAs cladding layer. The sample was then thinned and a back contact was applied as for the standard lasers in section 2.3.1.14.

2.3.4.5 Cleaving the sample

The samples were then cleaved into of lengths of 3, 2.5, 2, 1.5 and 1mm. The samples were then ready for characterization. As the ridges are broad, they may be probed directly. However, during cw characterization of the device it was observed that the

sample suffers from localized heating around the probe tip as a consequence of the localized high carrier density there. CW performance was degraded by this measurement method. This situation can be avoided in different ways. The first is to wire bond the device, as for narrow ridges with bondpads, so that the injected carriers are spread over the length of the device and equally pump the ridge along its length. Alternatively, the laser can be operated in the pulsed regime, so that heat generating due to the injection of carrier is minimized.

2.4 Investigations during device fabrication

2.4.1 Etching mechanism

To maximize the confinement of the optical mode of the QD laser a deep etch of the ridge through the active region is necessary. However this may lead to both electrical and optical losses along the sidewalls of the device due to carrier mobility to surface states (non-radiative recombination) and scattering imperfections. It has been predicted that electrical losses due to the rough sidewalls may be negligible for the QD structures because of the 3 dimensional localization of carriers in the dots.

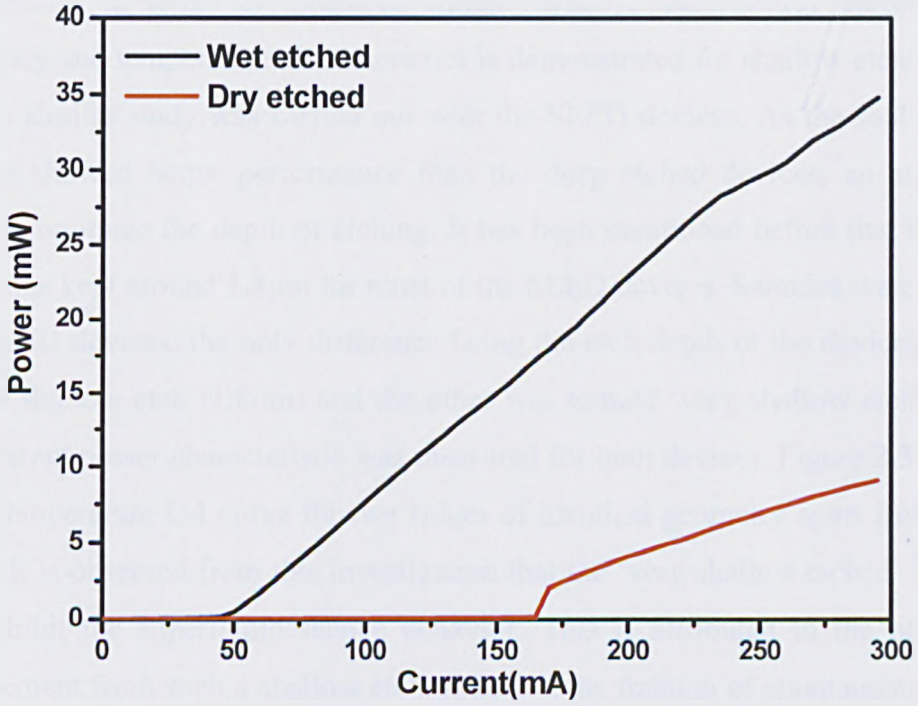

Fig. 2.2 Current-power characteristics for a wet chemical etched and dry reactive ion etched device

To investigate the comparative effect of the etch quality on the performance of deeply etched by wet or dry etch, two pieces of the same sample were processed into ridge lasers, the only difference being the etching procedure of the ridges. One sample was etched using the ICP etcher and the other was etched using 1:1:1 (HBr: CH_3COOH: $K_2Cr_2O_7$) solution. The etching depth (~3μm) for both the samples was same, corresponding to an etch through the QD containing active region. The room temperature current-power characteristics were measured for both devices. 3mm long and 15μm wide ridges were measured and the characteristics are shown in Fig. 2.2. It is evident from the characteristics that the room temperature threshold current density for the wet etched sample is much lower than that of the dry etched one. The reason for the lower J_{th} is attributed to the lower electrical loss along the sidewalls of the wet chemical etched device as compared with the dry etched device. The fabrication process for the following laser and SLED devices were influenced by this result and most of them were shallow etched by wet chemical etching unless mentioned otherwise [5].

2.4.2 Etch depth

In chapter 3 a detailed study of the ridge geometry is discussed. Improved performance in terms of threshold current density, transparency current density, efficiency and temperature characteristics is demonstrated for shallow etched devices. Later a similar study was carried out with the SLED devices. As the shallow etched devices showed better performance than the deep etched devices, an attempt was taken to optimize the depth of etching. It has been mentioned before that the etching depth was kept around 1.8μm for most of the SLED devices. Samples were processed into SLED devices, the only difference being the etch depth of the devices. One was termed shallow etch (1.8μm) and the other was termed 'very shallow etch' (0.5μm). The current power characteristic was measured for both devices. Figure 2.3 shows the room temperature L-I curve for two ridges of identical geometry apart from the etch depth. It is observed from this investigation that the 'very shallow etched' devices do not exhibit the superluminescence behavior. This is attributed to the poor optical confinement from such a shallow etch, reducing the fraction of spontaneous emission guided within the waveguide. Also, current spreading is expected to result in lower

current densities for the "very shallow etched" sample. Results from deeply etched SLEDs (i.e. through the active region) are not considered in this thesis because it was observed that deep etched SLEDs tend to lase at low drive currents. This is attributed to more confined optical modes of the SLEDs, which results lower effective facet reflectivities and therefore in regenerative. If broad-band, low reflectivity facet coatings, or other methods to reduce effective facet reflectivity are implemented, then deeply etched SLEDs may require further investigation.

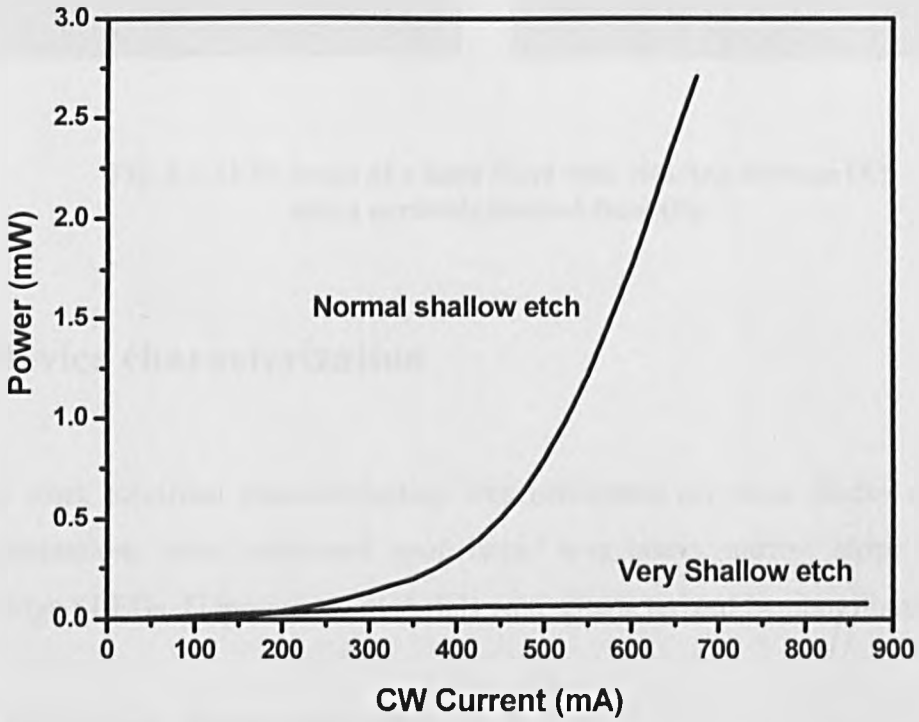

Fig. 2.3 Current-power characteristics for a normal shallow etched SLED device and a very shallow etched device.

2.4.3 Cleave damage on the facet

It has been observed that some laser ridges suffer damage due to poor control of the cleaving process. Figure 2.4(A) depicts an example of such damage due to cleaving and Fig. 2.4(B) is an example of a perfectly cleaved ridge facet. Since minor imperfections alter the reflectivity of the facet, and hence the condition for threshold, results from devices with such facet damage should be discarded.

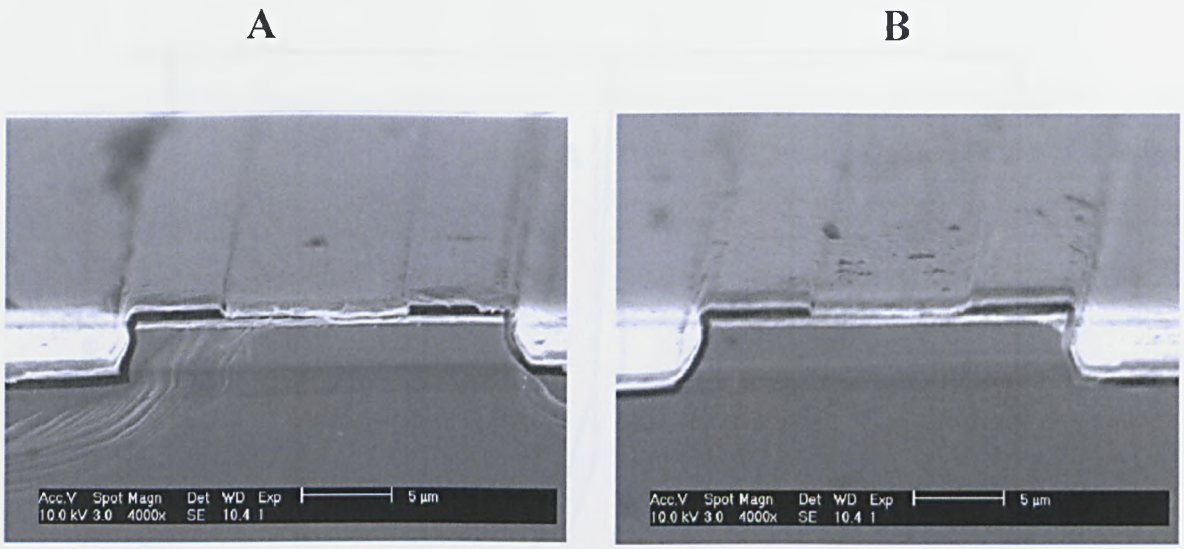

Fig. 2.4 SEM image of a laser facet with cleaving damage (A) and a perfectly cleaved facet (B).

2.5 Device characterization

In this work electrical characterization was performed on mesa diodes and optical characterizations were performed upon broad area lasers, narrow stripe lasers and tilted ridge SLEDs. Unprocessed materials were characterized by photoluminescence.

2.5.1 Electrical characterization

2.5.1.1 Current-voltage characteristics

The current voltage (I-V) characteristics of mesa diodes are measured to determine the quality of material used for the QD lasers and SLEDs. Reverse leakage current is measured in order to determine the defect density in the material. At a particular reverse voltage, lower reverse leakage current is a good indication of the presence of fewer dislocation defects in the material, as dislocations would form a leakage path through the active region. Also the observation of a higher reverse breakdown voltage draws the same conclusion. A sharp breakdown voltage compared to a soft breakdown is also indicative of fewer dislocations and hence good material quality [6].

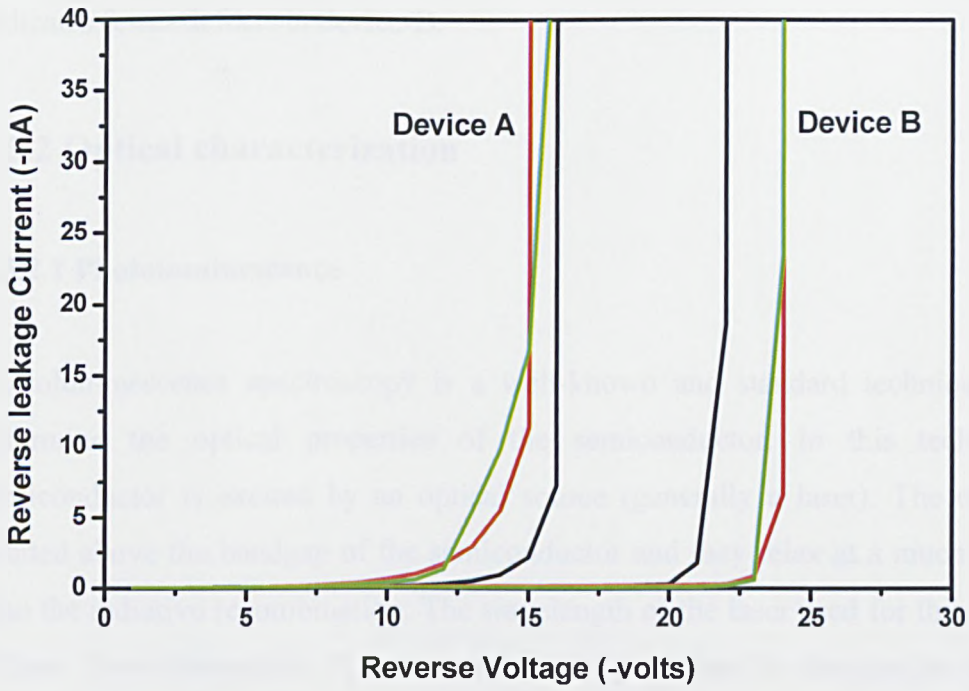

Fig. 2.5 Reverse leakage current plotted as a function of the reverse bias voltage for two mesa diodes.

On the other hand the forward I-V characteristics give a measure of the series resistance of the device. The reverse I-V is measured by direct probing. The samples measured were mesa diodes of 50 or 100μm diameter. The top p-contact was probed directly by the probe and the negative probe is connected to the n-side of the device through the base of the ceramic tile. The growth mechanism for the two devices in the fig. 2.5 are different where device B benefits form a narrower low temperature grown GaAs barrier layer between the dot layers, which improves the electrical characteristics. The difference in the growth of these two devices is discussed in detail in chapter 5.

The current is driven through the device by a current source through the probes. The output is connected to a curve tracer. A computer using Labview software drives the current source. The voltage as a function of current is recorded in the computer simultaneously from the curve tracer. A typical example of I-V characteristics demonstrating the effect of a reverse leakage is depicted in Fig. 2.5. The reverse voltage is plotted as a function of the reverse current in the linear scale. Higher break

down voltage and smaller reverse current at a particular reverse bias (>-17Volts) indicates fewer defects in device-B.

2.5.2 Optical characterization

2.5.2.1 Photoluminescence

Photoluminescence spectroscopy is a well-known and standard technique used to determine the optical properties of the semiconductor. In this technique the semiconductor is excited by an optical source (generally a laser). The carriers are excited above the bandgap of the semiconductor and they relax at a much faster rate than the radiative recombination. The wavelength of the laser used for this purpose is 532nm. Power dependent PL measurements are performed to characterize the ground state emission peak and the excited state of the QD material. With increasing excitation power state filling occurs due to the limited degeneracy of the QD states. From the linewidth of the emission we gain information regarding the inhomogenity of the QDs (i.e. the size/composition distribution).

2.5.2.2 Electroluminescence

Electroluminescence (EL) spectroscopy is similar experiment to PL. In EL carriers are electrically injected into the processed device instead of optical pumping. In EL the current is injected through the p and n region of the QD laser or SLED and the emission from the active region of the device is captured by an optical fiber and traced in an optical spectrum analyzer (OSA). As the width of the ridge is generally 20, 15 or 5μm a multimode fiber is used so that most of the output light is captured. Spectra are recorded in a computer from the OSA using a Labview software program. Most of the measurements are performed at room temperature. However for measurements at elevated temperature a heater is connected to the sample holder and a thermocouple measures the temperature of the sample. This facility enables us to record the EL spectrum over a range of temperatures, up to 150^0C. Later in this chapter some of the measurements are done at little below the room temperature. For this a peltier cooler was used, which enabled us to perform the measurement 5^0 below the room

temperature. A schematic diagram of the apparatus required for the EL measurement is shown in Fig.2. 6.

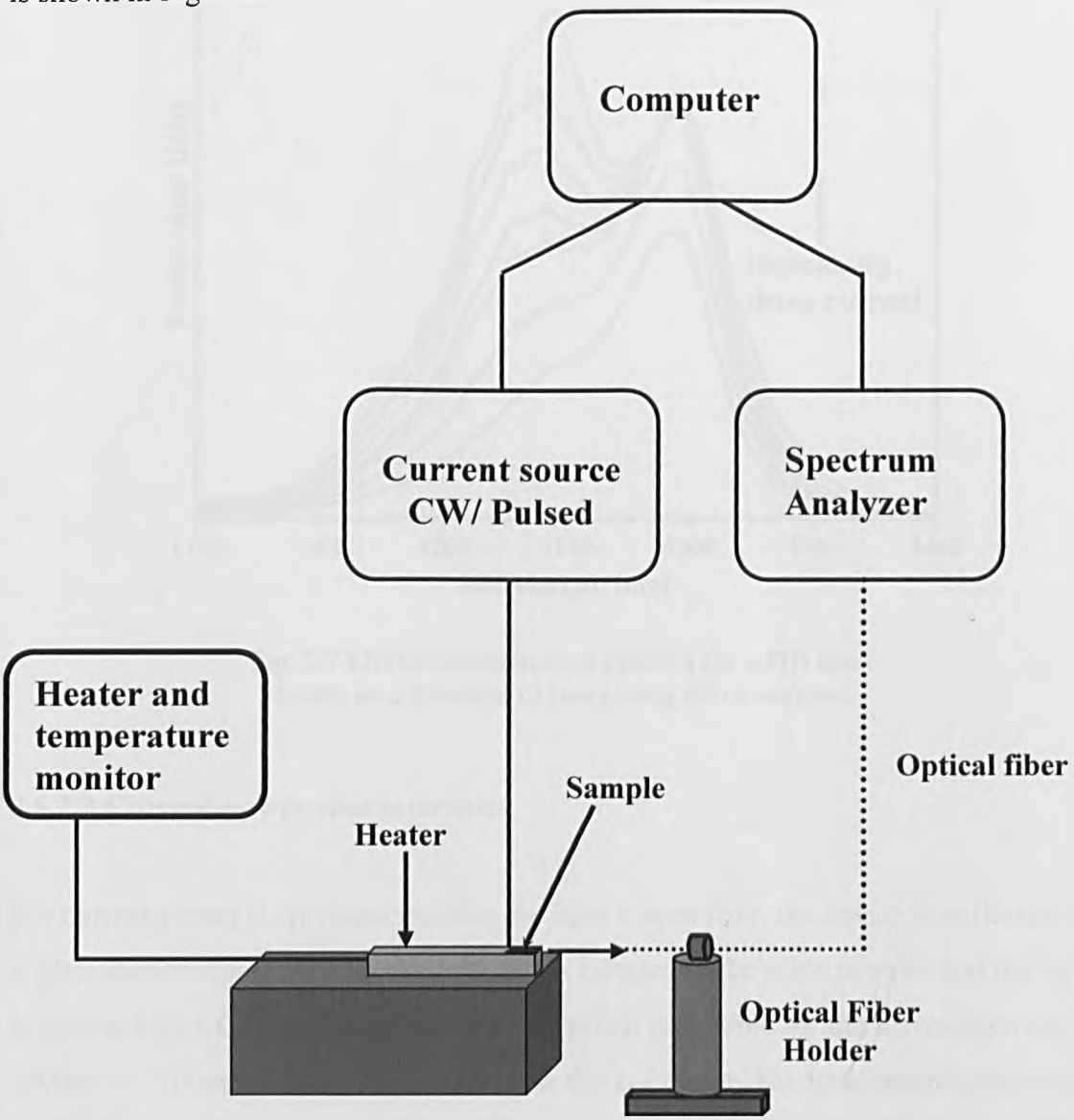

Fig. 2.6 Schematic diagram for the Electroluminescence measurement set up

From the EL spectrum, information about the quality and size distribution of the QDs grown in the active region of the device can be ascertained. The shift of the wavelength to the excited states from the ground state as a function of drive current, temperature or cavity length can be investigated. Primary information about the saturation of the QD states can also be obtained. Figure 2.7 shows the room temperature EL spectrum as a function of drive current of a QD SLED. It clearly shows saturation of the ground state of the QDs in the device and increase in the first excited state with increasing drive current.

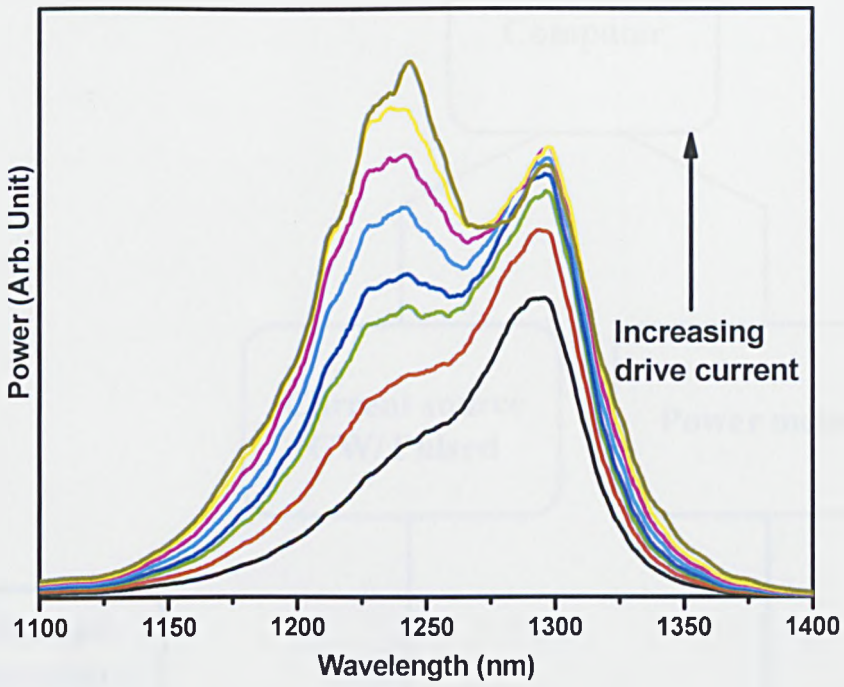

Fig. 2.7 Electroluminescence spectra for a QD laser device as a function of increasing drive current.

2.5.2.3 Current-power characteristics

For current-power (L-I) characteristics the light output from the device is collected by a photodetector/power meter. The current is injected in the same manner and the light is captured by a Germanium photodetector, which is suitable for the wavelength range 600nm to 1700nm. Labview software plots the L-I curve. The temperature dependent L-I curve is also obtainable using this setup. A Peltier cooler is used to set the temperature to $\sim 10^0$C above or below room temperature. For high temperature operation of the device a heater is used to raise the temperature of the device as mentioned in the previous paragraph. A schematic diagram of the set up is shown in Fig. 2.8.

From the L-I curve we can extract the threshold current (I_{th}) of the laser device, and the external differential efficiency (i.e. the gradient), η_d. Additionally, if the lasing transition in the device changes state as the current is increased this will show a kink in the L-I curve. Figure 2.9 shows a typical L-I curve of as 2mm long laser cavity at room temperature.

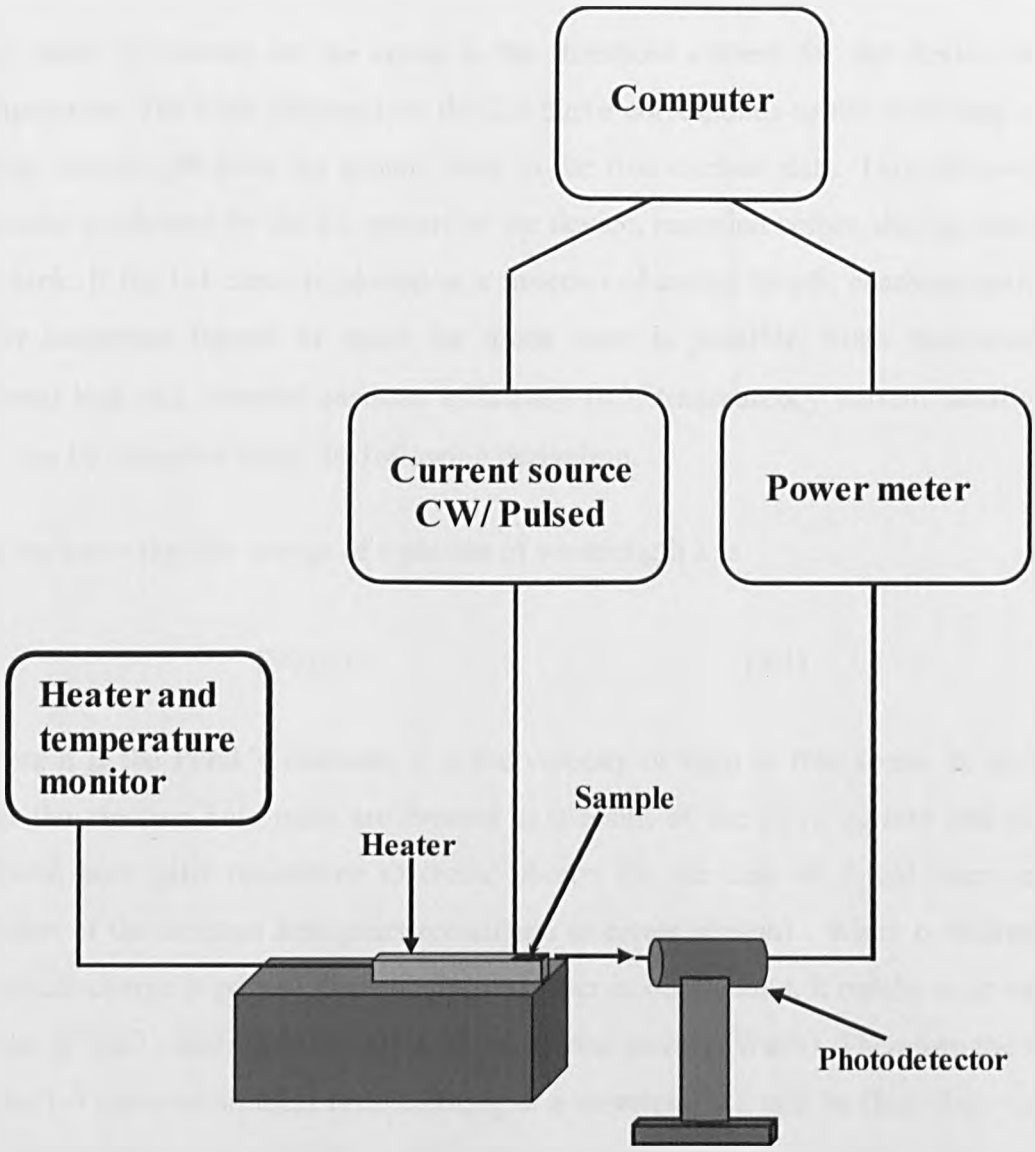

Fig. 2.8 Schematic diagram for the current-power characteristics measurement setup.

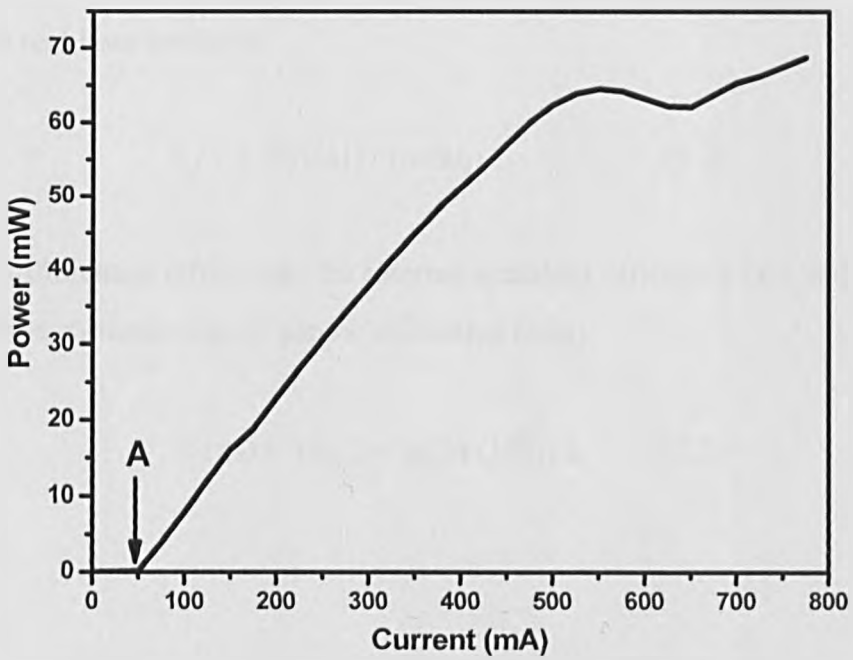

Fig. 2.9 Typical current-power characteristics curve for a 2mm long QD laser. The curve shows the switching of state

The point '*A*' shown on the curve is the threshold current for the device at that temperature. The kink observed on the L-I curve corresponds to the switching of the lasing wavelength from the ground state to the first excited state. This phenomenon was also confirmed by the EL spectra of the device, recorded before, during, and after the kink. If the L-I curve is plotted as a function of cavity length, characterization of other important figures of merit for diode laser is possible. Such parameters as internal loss (α_i), internal quantum efficiency (η_i); transparency current density (J_0) etc. can be extracted using the following derivation.

As we know that the energy of a photon of wavelength λ is

$$E=h(c/\lambda) \qquad (2.1)$$

Where h is the Plank's constant, c is the velocity of light in free space. In an ideal laser the electron hole pairs are created as a result of the drive current and all the electron hole pairs recombine to create photon (In the case of a real laser only a fraction of the electron hole pairs recombine to create photon) . When q coulomb of electrical charge is passed through an ideal laser in one second, it results in an output power of $h(c/\lambda)$ Joules per of output power in one second (Watts). Therefore the slope of the L-I curve of an ideal laser emitting at a wavelength λ will be $(hc)/(\lambda q)$. On the other hand the slope efficiency ($P\Delta/\Delta I$) of the real laser can be obtained from the linear part of its L-I curve. It must be remembered that for a laser with two cleaved facets only half the output power is measured. Thus the external differential efficiency (η_d) of the real laser becomes

$$\eta_d = 2\,(P\Delta/\Delta I) / (hc/\lambda q) \qquad (2.2)$$

From the differential efficiency, the internal quantum efficiency (η_i) and the internal loss (α_i) for a particular cavity can be calculated from;

$$1/(\eta_d) = 1/\eta_i\,[1+ \alpha_i/ \ln(1/R)]\,L \qquad (2.3)$$

Where L is the length of the laser cavity and R is the reflectivity of the facet. As all the lasers described in this thesis are GaAs based device, the reflectivity is taken 0.32 in all cases.

If the L-I characteristic is recorded as a function of temperature, the characteristic temperature, T_0, may also be extracted. This can be deduced from the equation.

$$T_0 = \Delta T / \ln(\Delta J_{th}) \qquad (2.4)$$

Where ΔJ_{th} is the change in the threshold current density due to the change in cavity temperature ΔT.

2.5.2.4 Gain measurement using Hakki-Paoli method

The gain measurement is performed in a similar manner to the EL measurement described in section 2.5.2.2. A similar experimental setup with a very high resolution OSA is required for the gain measurement of the QD laser. Short length laser cavities are used for this measurement in order that individual Fabry-Perot modes may be resolved. Gain spectra are obtained by measuring the depth of the modulation, caused by the Fabry-Perot resonance, in the emission spectrum [7]. Initially the EL spectrum is captured over a very short wavelength span (5nm) in order to optimize the collection efficiency and resolution. The spectra are then recorded over the complete wavelength range of interest (~200nm) around which the short cavity laser emits from its ground state and first excited state. The captured spectra are then processed using an excel macro to obtain the gain spectrum. The macro selects the maxima and the minima of the peaks of the whole spectra captured. The program then calculates the modulation depth by averaging each two consecutive peaks $\frac{1}{2}(P_1 + P_2)$ and dividing by the intermediate valley V_1 and the depth of modulation is obtained by the relation:

$$r_1 = (P_1 + P_2) / 2V_1 \qquad (2.5)$$

The net gain is then obtained by the relation:

$$\Gamma G_1 = 1/L \ln[(r_1^{1/2}+1)/(r_1^{1/2}-1)] + 1/L(\ln R) \qquad (2.6)$$

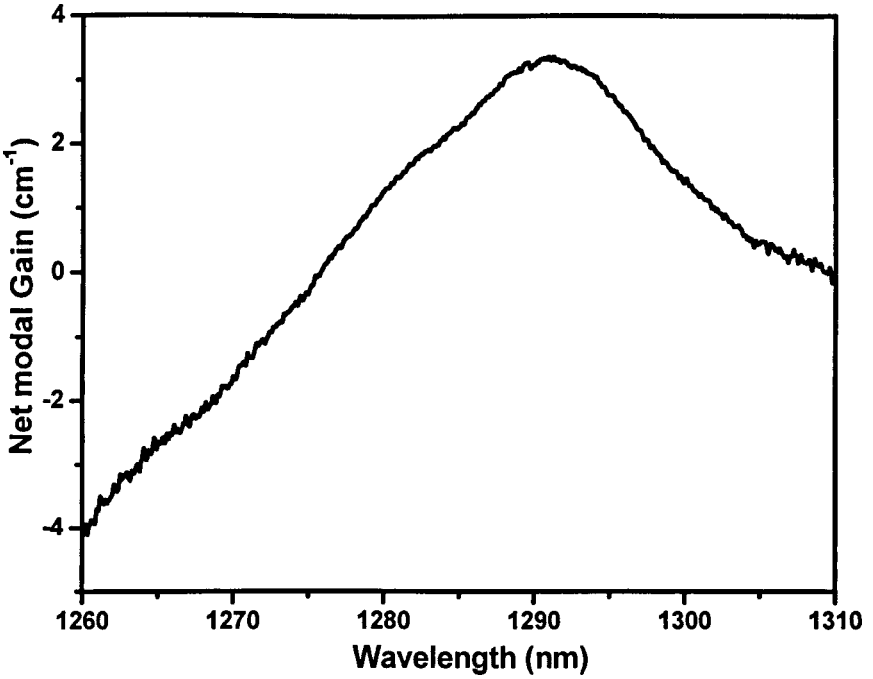

Fig. 2.10 Hakki-Paoli gain curve of a 2mm long QD laser at $0.9J_{th}$. The curve shows the ground state emission peak around 1290nm

In this equation Γ is the electromagnetic filling factor, L is the length of the laser and R is the reflectivity of the as cleaved facet. Figure 2.10 shows a typical gain spectrum of a short cavity laser. The spectrum is taken at $0.9J_{th}$ of a 2mm long 5 DWELL laser. The peak around 1290nm corresponds to the ground state emission.

References

[1] I. N. Stranski and L. Krastanow. Sitzungsberichte d. Akad. D. Wissenschaften in Wien, Abt IIb, Band 146, 797, (1973).

[2] H. Y. Liu, M. Hopkinson, C. N. Harrison, M. J. Steer, R. Frith, I. R. Sellers, D. J. Mowbray and M. S. Skolnick J. Appl. Phys. 93, 2931 (2003).

[3] P. B. Jocye, T. J. Krzyzewski, G. R. Bell, T. S. Jones, E. C. Le Ru, and R. Murray, Phys. Rev. B 64, 235317 (2001).

[4] T. J. Walter, A. G. Cullis, D. J. Norris and M. Hopkinson, Phys. Review Lett.86, 2381 (2001).

[5] S. K. Ray, K. M. Groom, R. A. Hogg, H. Y. Liu, M. Hopkinson, T. J. Badcock, D. J. Mowbray, M. S. Skolnick, IEEE Photon. Technol. Lett. Vol. 17, No. 9, (2005).

[6] P. G. Neudeck, W. Huang and M. Dudley Solid state electron., Vol. 42, No. 19 2157-2164, (1998).

[7] B. W. Hakki and T. L. Paoli "Gain spectra in GaAs double heterostructure injection lasers" J. Appl. Phys, Vol 46, No. 3, March (1975).

Chapter 3: Publications came out of this work

Journal publications:

1> S. K. Ray, K. M. Groom, R. A. Hogg, H.Y. Liu, I R. Sellers, M. Hopkinson, T. J. Badcock, A. J. Ramsay, D. J. Mowbray, M. S. Skolnick. *"Growth, Fabrication, and Operating Characteristics of Ultra-Low Threshold Current Density 1.3 um Quantum Dot Lasers"*. Jpn, Jrnl. of Appl. Phys. 44 (4B), 2520-2522, (2005).

2> S. K. Ray, K. M. Groom, R. A. Hogg, H. Y. Liu, M. Hopkinson, T. J. Badcock, D. J. Mowbray, M. S. Skolnick. *"Improved Temperature Performance of 1.31-μm Quantum Dot Lasers by Optimised Ridge Wavelength Design"*. IEEE Photon. Technol. Lett. Vol. 17, No. 9, September (2005).

Poster and conference presentation:

1> Poster presentation, Laser Summer School, 16-25th Aug. 2004, Gregynog, Wales.

2> Oral presentation, SIOE 2005, *"Effect of Processed Device Structure on Improving the Performance of 1.31 um Qunatum Dot Lasers"*. 21-23rd March 2005, Cardiff, Wales

Chapter 3: Improved device fabrication for 1.3μm Quantum Dot Lasers

3.1 Introduction

The use of a quantum dot (QD) active region is of considerable interest for the realisation of temperature insensitive lasers [1]. More recently the use of QDs as the active element in optical amplifiers, for the regeneration, reshaping and retiming of an optical signal, has been shown to exhibit considerable promise [2]. For QD lasers an important issue is gain saturation, which results from the relatively small number of states in the quantum dot array. Many groups have showed different approaches aimed to overcome this problem, for example increasing the quantum dot areal density and improving the size uniformity of the quantum dots within a single quantum dot layer [3, 4]. Another alternative method to increase the effective number of QDs is to use a multilayer quantum dot active region. The ideal multilayer QD structure should have different layers with identical size distribution of quantum dots with no degradation of their optical efficiency compared to a single layer QD structure. In this chapter I describe previous work from my research group on developing 1.3μm QD lasers, and my work on characterising these materials with regard to ground state saturation and a phenomenon peculiar to QD system-wavelength switching between the ground state and the excited states. Furthermore, the development of device fabrication techniques which result in an improved device performance in terms of threshold current density, transparency current density, efficiency and temperature characteristics, is discussed.

3.2 Previous work

Conventional In(Ga)As quantum dot lasers based on In(Ga)As dots in a GaAs matrix emitting in the wavelength range ~0.98-1.2μm was demonstrated previously [5]. To extend the emission wavelength to the commercially important 1.3μm several groups have demonstrated a number of techniques. Previously, to extend the emission wavelength to 1.3μm a low growth rate (LGR) (≤0.05ML/sec) has been used. This

technique resulted in larger InAs clusters with higher indium composition. QD laser fabricated from these structures have shown 1.3μm emission [6] but suffered from low QD densities (~$1x10^{10}$ cm^2) and gain saturation unless low loss cavity designs are used even in multilayered systems. Atomic layer epitaxy (ALE) is another method to extend the emission to 1.3μm. In this technique a pause is introduced between the growth of In and Ga, which enhance the surface migration of In atoms and also results in large In rich clusters. These structures also suffer from a low QD density and hence low saturated gain. Another approach to extend the emission wavelength is to cover the InAs QDs with an InGaAs strain reducing layer (SRL) and/or a thin AlAs cap layer [7].

Another method adopted by some groups to reach 1.3μm emission is to cover the InAs dots with InGaAs or alternatively to grow the dots within an InGaAs quantum well (QW) [7-9]. The structure with InAs QDs in an InGaAs QW is now popularly known as dot-in-well structure or DWELL structure. These DWELL lasers have shown both longer emission wavelengths and low threshold current density (J_{th}). One more advantage of the DWELL structure is that the QD density is higher than those which are grown on top of a GaAs layer [9]. QD laser structures reported in this chapter are all multilayered DWELL structures.

Vertically stacked and closely spaced QD structures were investigated by several groups, typically based on InAs QDs within GaAs spacer layers [10, 11]. The electronic properties of the QDs of these multilayered structures are significantly changed by the stacking, and the QDs exhibit a redshift of their emission wavelength compared to the single QD layer samples [11]. This is attributed to the strain field from one QD layer affecting the nucleation and physical structure of the QDs in the subsequent layers. This may give rise to the individual QD layers having different properties and more over, the strain accumulation may limit the number of layers that can be deposited before defect formation. One method to overcome this problem is to increase the thickness of the spacer layer in between multi layers. These uncoupled multilayered QD structures with thick spacer layers are of considerable attention nowadays, and are important for some QD structures like 1.3μm InAs/GaAs QD lasers and QD memory devices. The QD laser structures studied in this chapter benefit from relatively thick GaAs spacer layer and some other engineering

techniques incorporated in the GaAs spacer layer, which will be discussed later in this chapter.

Initially it was predicted that the QD structures would be temperature insensitive because of their delta like density of states (DOS) [12]. In practice QD devices are not as temperature insensitive as they were predicted to be. The key assumption of Arakwa's paper is that the separation between levels is much larger than *kT*. This is generally not the case for the hole states within the QD. Sensitivity to temperature gave rise to several problems like higher threshold current density, rolling over of the power at higher temperature due to thermal loss of carriers, switching to the excited state due to gain saturation and of course homogeneous broadening. Several attempts have been made to improve the temperature performance of the QD device. An application of p-type modulation doping was proposed to improve QW laser characteristics by Takahashi *et al.* in the late 80s [13]. The p-doped layer acts as the supplier of holes to the closely spaced hole energy levels of the QDs, which increases optical and differential gain in the QD lasers. Techniques such as p-type doping of the dots [14] and the use of tunnel injection heterostructures [15] have resulted in reduced temperature sensitive threshold current density and higher characteristic temperature.

Apart from growth of the materials some other groups have tried to enhance performance of ridge waveguide lasers by optimising different fabrication parameters incorporating different fabrication techniques. One of the methods was to optimise the etching mechanism and etch-depth of the ridge waveguide structure. Ouyang *et al.* reported different ridge structures with different etch depths [16]. Deep etched devices were etched by dry etching technique and the shallow etched devices were etched by wet chemical etching. The deep etched devices enabled them to get a lower threshold current density compared to the shallow etched device.

Later in this chapter a technique to optimise the ridge etch and incorporate heat sinking is demonstrated. This technique results in a lower threshold current density for the shallow etched devices with a better temperature performance of the lasers compared to the deep etched device.

3.3 Growth of In(Ga)As quantum dots in an InGaAs quantum well

The InAs/InGaAs DWELL structures were grown in a VG Semicon V90H MBE system on Si-doped GaAs (100) substrate by Dr. M. Hopkinson and Dr H.Y. Liu. A schematic diagram of the layer structure of a DWELL is shown in Fig. 3.1. In the well the QDs were deposited by the continuous deposition of InAs. The growth rate for the deposition of QDs was ~0.092ML/sec. Each dot layer consisted of 3MLs of InAs grown on 2nm $In_{0.15}Ga_{0.85}As$ strained buffer layer (SBL). The InAs dots were covered by 6nm of $In_{0.15}Ga_{0.85}As$ strain reducing layer (SLR) to extend the emission wavelength and this gives a complete DWELL structure. The growth temperature for this layer was 500^0C [17].

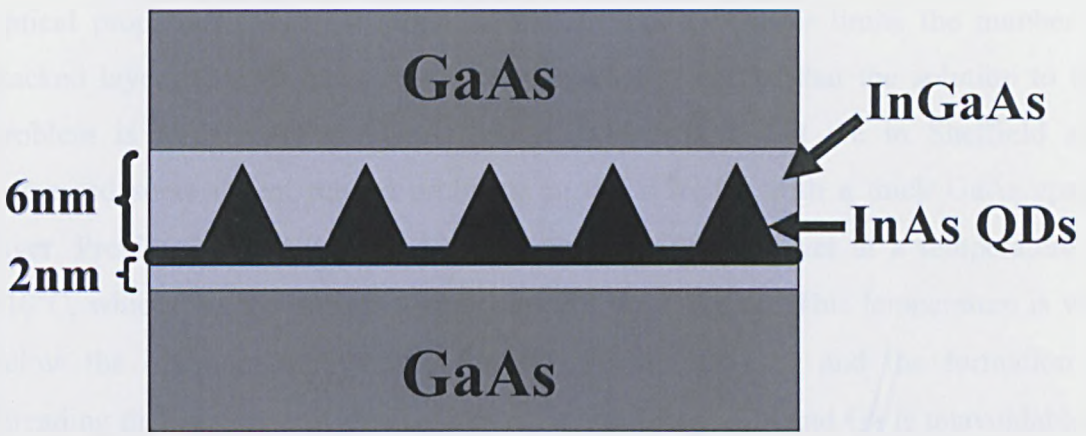

Fig. 3.1 Schematic diagram of a single DWELL structure. QD s are grown on 2nm InGaAs SBL and capped by 6nm InGaAs SLR

3.4 Optimisation of the growth of InAs QD in InGaAs well

3.4.1 Two Indium sources

After the deposition of the InAs/InGaAs DWELL the InGaAs well and the GaAs barrier layer were deposited at the same growth temperature as the DWELL (500^0C) with one In source. However, 500^0C is significantly below the optimum growth temperature of both InGaAs and GaAs. And hence the optical quality of this layer is

compromised. In addition, the use of a low growth rate of the InGaAs and GaAs requires a longer time at low temperature, which causes further degradation of the material quality. All the DWELL structures reported in this chapter were grown using two different In sources. This allowed us to reduce the detrimental effects associated with the low temperature growth. One cell was used to deposit the InAs QDs with a low growth rate of ~0.092ML/sec. The second cell was used to deposit the InGaAs quantum well structure with a Ga growth rate of 0.76ML/sec.

3.4.2 Growth temperature: High growth temperature spacer layer

Previously it has been observed by several groups that the strain field from one QD layer affects the nucleation and physical structure of the QDs in the subsequent layers [18, 19 and 20]. This leads to the formation of defects and QD layers with different optical properties. Also the strain formed by one QD layer limits the number of stacked layers [21]. It has already been mentioned earlier that the solution to this problem is to increase the GaAs spacer layer width. But we in Sheffield also witnessed some defect related problems in the DWELL with a thick GaAs spacer layer. Previously we grew the 50nm thick GaAs spacer layer at a temperature of 510^0C, which was the growth temperature for the DWELL. This temperature is well below the optimum temperature for the growth of GaAs and the formation of threading dislocation was obvious. As the intermixing of In and Ga is unavoidable at higher temperature because of the volatility of InAs, the growth temperature for the GaAs spacer layer has to be low. AFM images from the uncapped samples grown with the spacer layer growth temperature 510^0C, exhibited the formation of several incoherent islands with irregular shape and the average size of the larger dots increased. This inhomogenity in size gives rise to a broader size distribution. Also it was observed that the surface morphology for these samples was rough and consisted of several 'mounds' and 'pits'. Cross sectional TEM of these samples showed several incoherent islands and threading dislocation in second and subsequent layers of the DWELL [22].

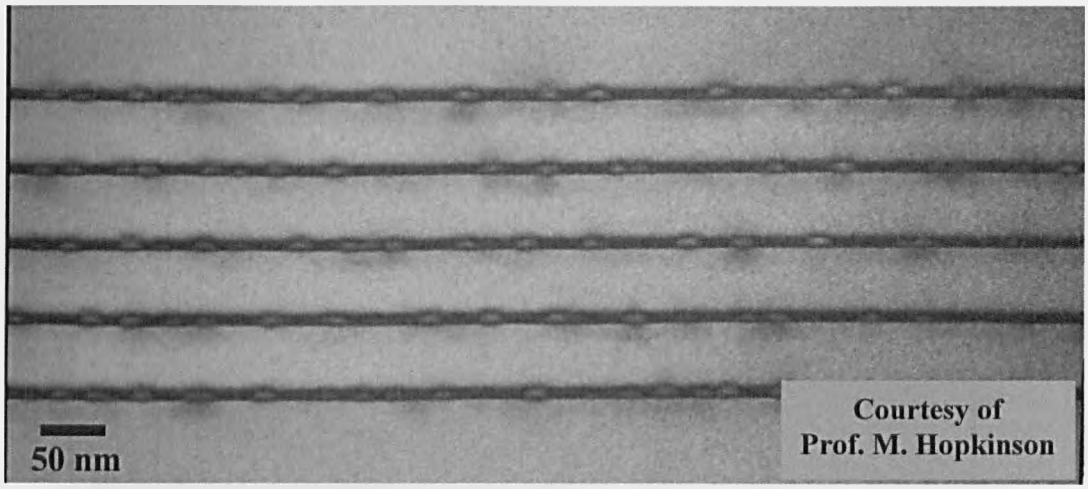

Fig. 3.2 Cross sectional TEM image of 5-layer InAs/InGaAs DWELL structure with high growth temperature GaAs spacer layer.

To overcome this problem a different growth temperature profile for the GaAs spacer layer was introduced by my co-workers at Sheffield. During the growth of the DWELL, immediately after the growth of the InAs QDs and InGaAs layer first 15nm of GaAs was grown at the same temperature (510^0C). The remaining 35nm of the GaAs spacer layer was deposited at a temperature of 580^0C. Before the growth of the next DWELL the temperature was brought back to 510^0C again. This is referred to as high growth temperature spacer layer (HGTSL) [22]. For these samples the InAs QDs have an average height of ~6.6nm and a similar density in each layer. No defects were observed by cross sectional TEM. From the cross sectional TEM (Fig. 3.2) no obvious vertical alignment of the QDs was observed, which indicates that 50nm GaAs spacer layer is thick enough to resist the strain field from one layer which could affect the nucleation of dots in subsequent layers. A high areal dot density of ~4 x 10^{10} was observed from AFM image of the uncapped layer.

The incorporation of the HGTSL resulted in a significant enhancement of the room temperature (RT) PL efficiency. The RT PL of the structure is shown in Fig 3.3. It has a ground state peak at 1.3μm with a reasonably narrow linewidth of ~30meV. Also the intensity for the samples with the HGTSL was ~3 times more than for samples without the HGTSL, indicating a lower number of nonradiative centres for the HGTSL samples. The detailed results of these studies are shown elsewhere [22]. The energy separation between the ground state and the first excited state was 50meV.

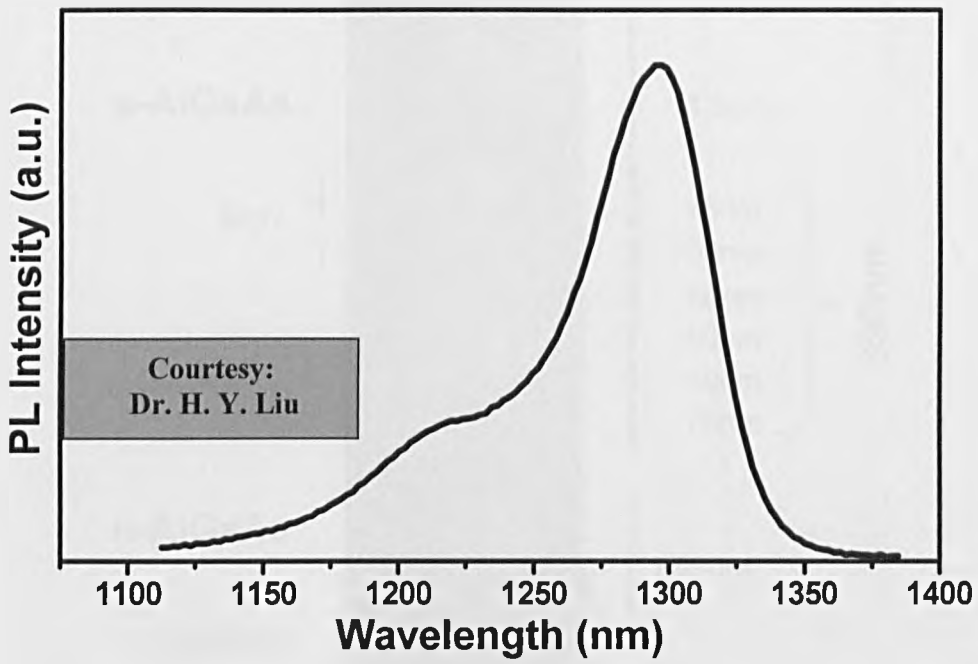

Fig. 3.3 Room Temperature photoluminescence spectra for a 5-layer DWELL structure with HGTSL.

3.5 Optimised growth conditions: Device structure

The quantum dot laser structures were grown on Si doped GaAs (100) substrate. Each dot-in-well layer consisted of 3.0 monolayers (MLs) of InAs grown on 2nm of $In_{0.15}Ga_{0.85}As$ and covered by 6nm of $In_{0.15}Ga_{0.85}As$ to give the DWELL structure. The five InAs/InGaAs DWELLs were separated by 50nm GaAs barrier layers and embedded between 150nm separate confinement heterostructure GaAs layers. Optical confinement was achieved using 1500nm $Al_{0.4}Ga_{0.6}As$ cladding layer. The upper p-cladding layer was doped with Be at 5×10^{17} cm^{-3} while the n-cladding layer was doped with Si at 5×10^{18} cm^{-3}. 125Å of short period superlattices were grown between each of the waveguide and cladding layer interface. Growth temperature for the AlGaAs layer was 620^0C and 510^0C for the In containing layer. The GaAs spacer layers utilised the HGTSL as discussed previously. The total thickness of the active region was 390nm. The schematic of the multi-layered structure of the sample is shown in the following figure.

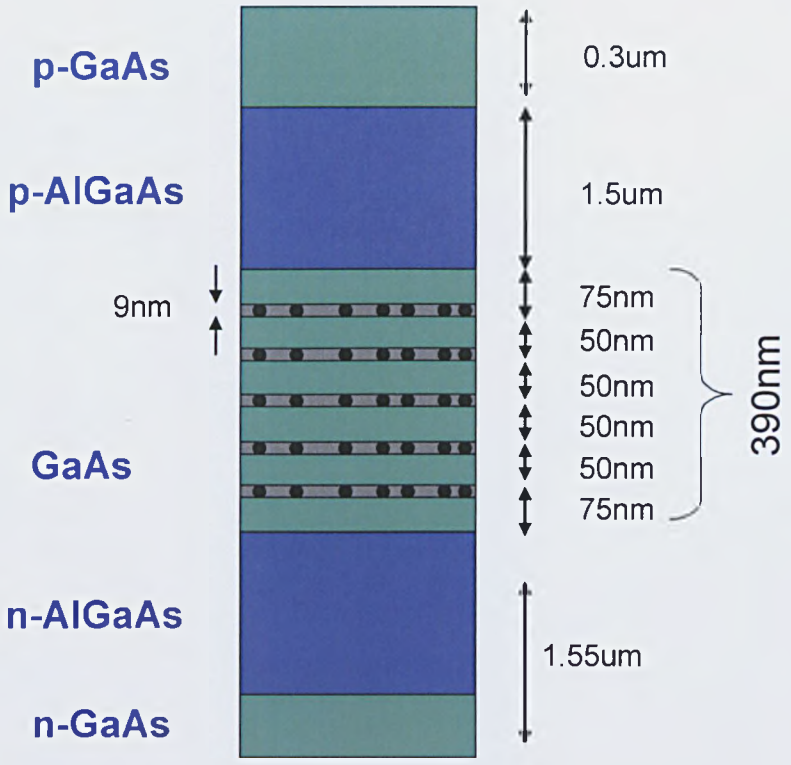

Fig. 3.4 Schematic of the cross section of a 5-layered DWELL InAs/GaAs QD laser

3.6 Device Fabrication

The wafer was processed into ridge waveguide lasers of 5, 8, 10, 15 and 20μm width. Au-Zn-Au contact was deposited to form front p-type contact and annealed at 360^0C. The ridge etch in this case involved the etching through the intrinsic region into the n-doped AlGaAs layer. This gave a total etch depth of 3.2μm. The etching was done using $SiCl_4$ based reactive ion etching (RIE). 500nm of Silicon Nitride (SiN_x) was deposited on top of the ridge. A contact window was opened on top of the ridge by reactive ion etching (RIE). Samples were subsequently thinned down to ~150μm. An n-type contact was formed by InGe-Au and annealed at 340^0C. Samples were cleaved into several lengths and measured by probing directly to the bondpads. The Scanning Electron Microscopic (SEM) image of the vertical cross section of a fabricated ridge waveguide laser device is shown in Fig. 3.5.

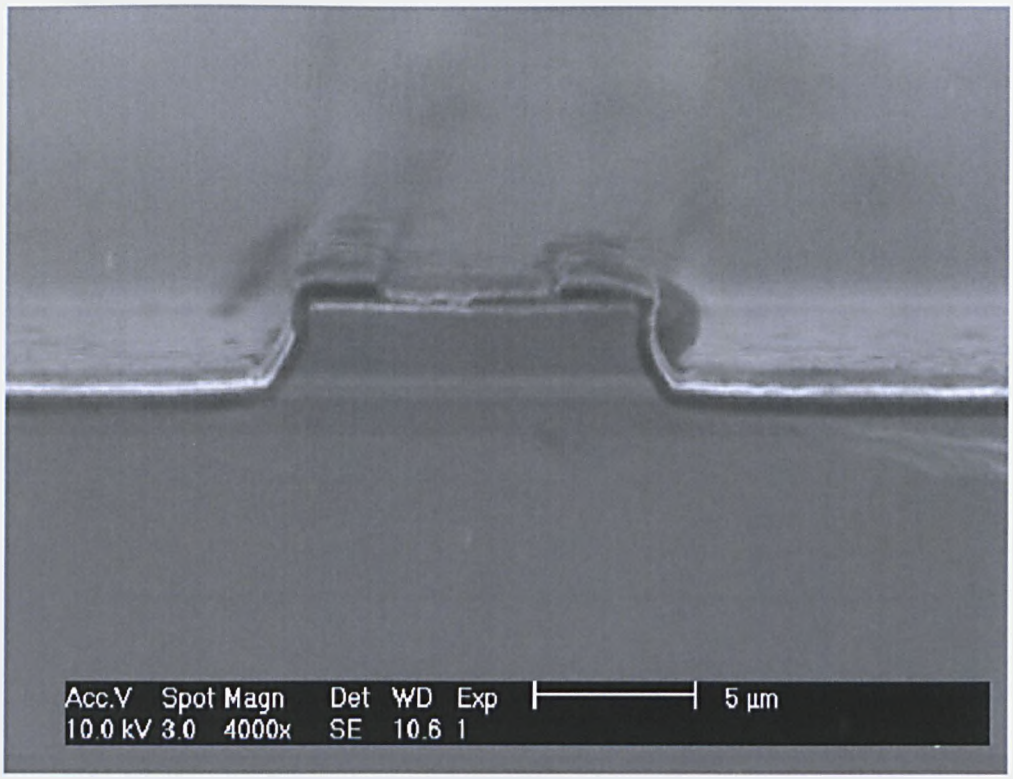

Fig.3.5 Scanning electron microscopic image of a 10μm wide facet. It was etched through the active region to the n-type AlGaAs layer.

3.7 Result and Discussion

3.7.1 1.3μm emission and low threshold current density

The ridge waveguide laser cavities were characterised for different lengths and widths. The continuous wave (CW) current-power characteristic at room temperature (~295K) of a 4mm long and 20μm wide laser cavity is shown in Fig. 3.6. The facets were as cleaved and a threshold current density of ~45A/cm^2 was measured. For a 2mm long, 20μm wide 3 DWELL cavity with HR/as cleaved facet a threshold current density of 23A/cm^2 was obtained [17].

These low threshold current densities are the direct result of the use of the high temperature growth step during the deposition of the GaAs spacer layer. In excess of 60mWs of power was observed at 400mA/cm^2 for the 4mm cavity. Rolling over was observed at a higher current density. The exact reason for this rolling over was attributed to the self-heating of the cavity due to high pump current.

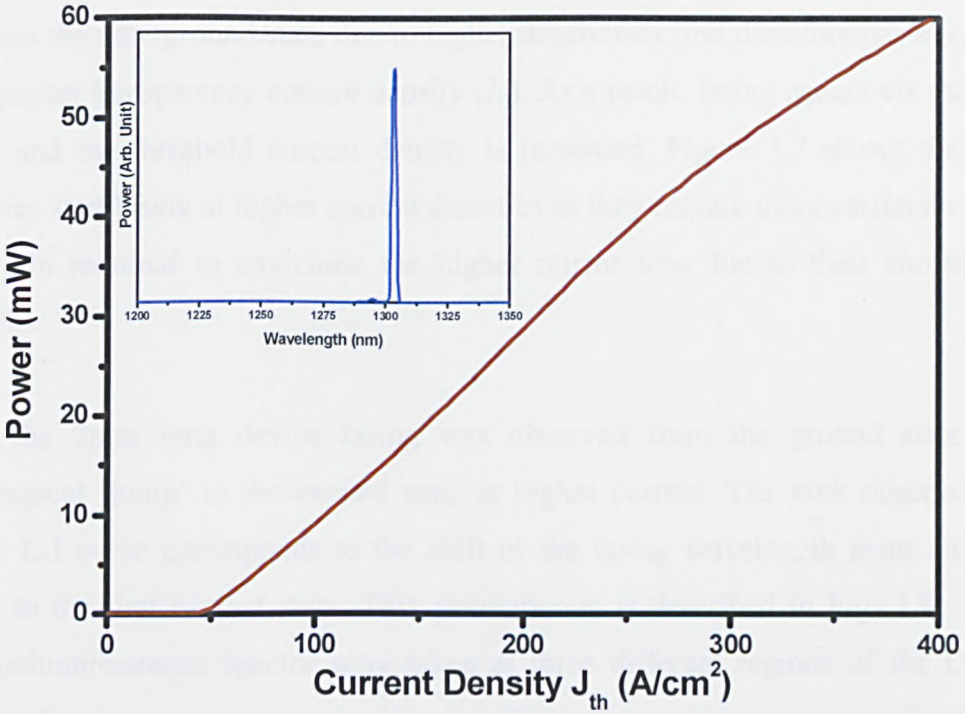

Fig. 3.6 Current-Power curve of a 1.3μm Quantum Dot laser cavity. Inset picture shows the corresponding electroluminescence spectrum.

The inset shows the CW electroluminescence spectra from the same device at a drive current (~150A/cm^2) sufficiently higher than the threshold current at room temperature (~297K).The peak emission wavelength was well above 1.3μm. No transition of the peak lasing wavelength from the ground state to the first excited state was observed at a higher drive current.

3.7. 2 Length dependent current-power characteristics

Current-power characteristic for different cavity lengths were measured to determine the shortest cavity which can provide sufficient gain to lase from the ground state at room temperature. Figure 3.7 shows the L-I curves for different cavity lengths. For 4, 3 and 2.5mm cavity complete ground state lasing was observed and the threshold current density increases only slightly. The 2mm cavity shows simultaneous lasing via the ground state and the first excited state. And the 1.5mm cavity lases entirely from the excited state and exhibits a very high threshold current density. We attribute this phenomenon to the gain saturation of the ground state. For shorter cavities the mirror losses are increased and finally the overall losses become more than the saturated gain (G_{th}) of the ground state. The excited state can accommodate more

carriers than the ground state due to higher degeneracy and therefore has a higher G_{th} and higher transparency current density (J_0). As a result, lasing occurs via the excited state and the threshold current density is increased. Figure 3.7 shows that shorter cavities start lasing at higher current densities as they require more carriers to achieve the gain required to overcome the higher mirror loss due to their shorter cavity lengths.

For the 2mm long device lasing was observed from the ground state with a subsequent 'jump' to the excited state at higher current. The kink observed in the 2mm L-I curve corresponds to the shift of the lasing wavelength from the ground state to the first excited state. This phenomenon is described in Fig. 3.8. The CW electroluminescence spectra were taken at three different regions of the L-I curve shown for 2mm long cavity in Fig. 3.7. Region A (~400mA), which is the linear region of the L-I curve shows complete ground state lasing at 1310nm. In region B simultaneous lasing or dual state lasing was observed both from the ground state and excited state. Dual state lasing occurs at around 600mA drive current at 1310nm and 1250nm corresponding to the ground state and first excited state respectively. A slight red shift in the ground state lasing wavelength is observed for the higher pump current. This is attributed to the self-heating of the cavity. The reason for this behaviour will be discussed later in this chapter.

The same phenomenon for QD lasers has been observed by other groups previously [23]. Both experimental and theoretical evidences showed that this phenomenon is the effect of finite life time of the carriers in the excited state. Markus *et al.*'s investigation suggested that the simultaneous lasing is the combined effect of the phonon bottleneck effect and Pauli blocking. With increasing drive current when the ground state reaches the lasing threshold all the carriers which relax into the ground state recombine quickly and with surplus supply of carriers the ground state carrier concentration saturates and clamps. However the excited state carrier concentration increases steadily until the threshold for lasing from the excited state is reached. This steady increase of the number of carriers occurs because of the finite lifetime of the carriers at the excited state due to the Pauli-Blocking of carrier relaxation from the excited state to the ground state. With further increase in drive current the excited state dominates the emission spectrum.

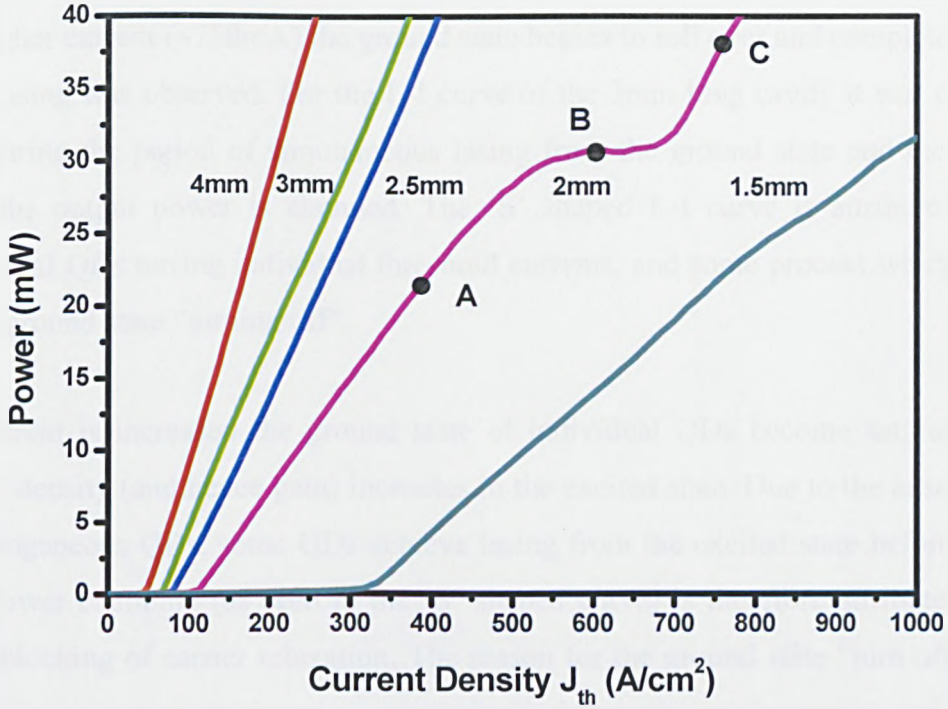

Fig.3.7 CW L-I curve at Room Temperature for different length 15micron Ridges

We observe the similar result experimentally. For the 2mm device up to a certain current the ground state lasing occurs. After a certain drive current the competition between the ground state and first excited state occurs.

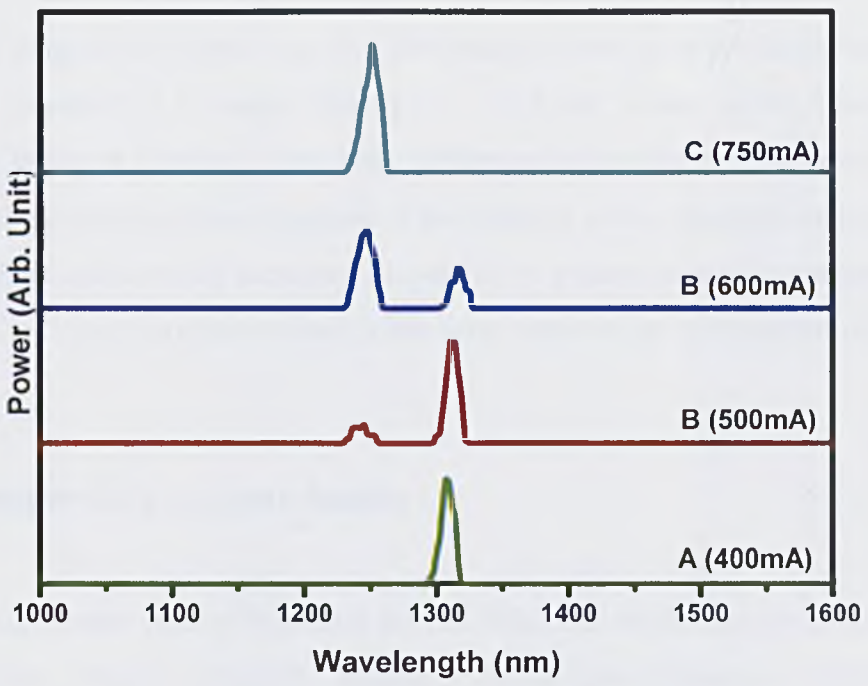

Fig. 3.8 Electroluminescence spectra taken at three different positions of the L-I curve of 2mm cavity.

At higher current (~750mA) the ground state begins to roll over and complete excited state lasing was observed. For the L-I curve of the 2mm long cavity it was observed that during the period of simultaneous lasing from the ground state and the excited state the output power is clamped. The 'S' shaped L-I curve is attributed to the individual QDs having individual threshold currents, and some process which results in the ground state "turning off".

As current is increased the ground state of individual QDs become saturated, and carrier density (and hence gain) increases in the excited state. Due to the ensemble of inhomogeneous QDs, some QDs achieve lasing from the excited state before others. The power clamping (as seen in the 'S' shaped curve) is therefore attributed to the Pauli-blocking of carrier relaxation. The reason for the ground state "turn off" is not clear. This has been attributed to a common hole population for the ES and the GS, and an increase in homogeneous line-width, reducing the peak gain of the ground state [2], or could be due to the self-heating. Further work is required to determine the exact mechanism. Nevertheless a clear switching is observed from the ground state (1.31μm) to the first excited state (1.45μm) for the 2mm cavity. The state switching observed for the 2mm cavity device occurs with no *hysteresis* and is attributed to gain saturation of the QD ground state, incomplete gain clamping, and subsequent lasing from the excited state [23].

The 1.5mm long device lases from the first excited state at room temperature and reaches the threshold at a current density of ~325A/cm^2 where as the 2.5mm long cavity starts lasing at 75A/cm^2. This large difference in the threshold current density in between these two cavities is because of the wastage of the injected carriers filling the ground state and possibly increased non-radiative process related to carrier-carrier scattering. For 0.5mm cavities no lasing has been observed up to a current density of 1000A/cm^2.

3.7.3 Transparency current density

The threshold current density is plotted for full ridge etched devices as a function of reciprocal cavity length in Fig.3.9. Strong deviation from linearity is observed for cavity lengths ≤ 2 mm and the threshold current density increases abruptly

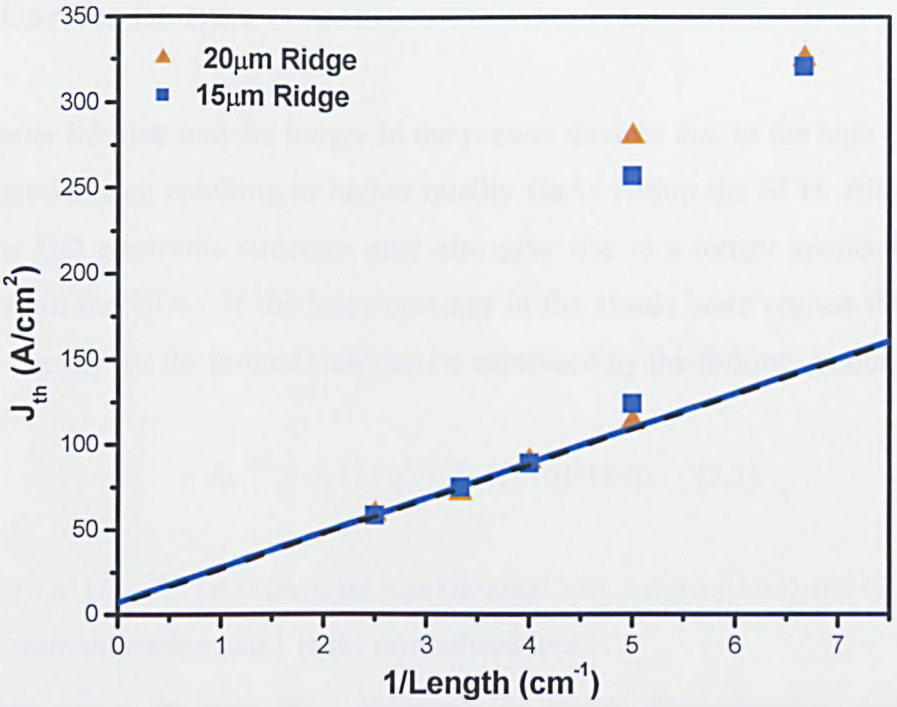

Fig. 3.9 CW room temperature threshold current density plotted as function of inverse cavity length for 15 and 20micron ridges. Intercept gives the transparency current density.

corresponding to the occurrence of wavelength switching described previously. We noticed that the threshold current density for the 2mm cavity increases abruptly. We attribute this effect to the ground state gain saturation. In this case the mirror loss increases as the cavity length decreases and finally overall losses become more than the saturated ground state of the ground state.

A very low transparency current density (J_0) is obtained from an extrapolation of the data, of ~1.5 A/cm^{-2} per QD layer. This value is ~1/5th that of the lowest previously reported transparency current density, while the present saturated gain per QD layer is ~2/3 of that in this previous report [24]. The present low transparency current is clearly due in part to a relatively low number of QDs participating in lasing. However, the fact that the saturated gain is only ~2/3 of that reported by Kovsh *et al.* suggests that the low dot density is not the sole reason for the very low transparency current. One possible explanation for this behaviour is either a more efficient use of injected carriers via a higher QD carrier capture cross section, which is possibly a consequence of the DWELL structure, or a longer carrier life time [26].

3.7.4 Carrier lifetime

The carrier lifetime may be longer in the present devices due to the high temperature GaAs growth step resulting in higher quality GaAs within the SCH. Alternatively a different QD electronic structure may also give rise to a longer spontaneous decay time within the QDs. If the laser operates in the steady state regime the threshold current density for the ground state can be expressed by the following equation [27]:

$$J_{th}^{GS} = J_1 (1+q) + J_2 \{(1+q)/ (1-q) \quad (3.1)$$

Where $q = \alpha / G_{GS}^{sat}$ {α is the total loss (internal loss + mirror loss) and G_{GS}^{sat} is the ground state saturation gain} is the normalised loss.

As the length of the laser cavity increases the ground state saturation gain increases and the mirror loss decreases. For an infinite long cavity the normalised loss (q) becomes zero. So, the transparency current density equals the sum of J_1 and J_2. The first term on the right hand side of equation 3.1 contributes to the QD ground state and the second term contributes to the QD excited state [27].

$$J_1 = (en_{QD})/\tau_{GS} \quad (3.2)$$

And

$$J_2 = J_1 (2\tau_0/\tau_{ES}) (1+ \tau_{GS}/ \tau_e) \quad (3.3)$$

Where, τ_0 is the intrinsic relaxation time for the unoccupied ground state, τ_{ES} is the recombination life time for the excited state, τ_{GS} is the recombination life time for the ground state and τ_e is the time for thermo ionic emission from the ground state. In equation 3.3 if the value of τ_e is neglected ($\tau_e \rightarrow \infty$), the value of J_2 becomes negligible and the transparency current density becomes almost equal to J_1. Thus from equation 3.2 the value of the recombination lifetime for the ground state can be calculated. In equation 3.2 putting, e= 1.602 X 10^{-19}, the determined transparency current and an assumed QD density of $2x10^{10}$ cm^{-2} (half the areal density as there is thought to be a bimodal QD size distribution) gives an estimated value of the recombination lifetime for the ground state emission. The calculated value of τ_{GS}

becomes ~2 ns. This lifetime has not been measured directly for the present QDs, but is not an unreasonable value [26].

3.7.5 External differential efficiency

The reciprocal differential efficiency is plotted in Fig. 3.10 as a function of cavity length for 15 μm and 20 μm wide ridges. For cavity lengths ≤ 2 mm a strong deviation from linearity is again observed, corresponding to devices lasing via the first excited state. Extrapolation of the linear region indicates an internal quantum efficiency of 65 ±5% and the gradient in this region gives internal losses of 2.2±0.5 cm^{-1} and 2.5±0.5 cm^{-1} for the 20 μm and 15 ridges, respectively.

Fig. 3.11 shows the dependence of the mirror loss on the cavity length for a Fabry-Perot laser. By calculating the mirror losses for 2mm and 1.5mm cavities the saturated gain of the QD layers may be estimated as 8~10cm^{-1}. This value is in agreement with previously published results where ~1 cm^{-1} of gain is obtained for each $1x10^{10}$ cm^{-2} of dot density [24, 25, 28, 29, 30]. The areal dot density in the present devices is $4x10^{10}$ cm^{-2} per layer but due to the bimodal dot distribution only

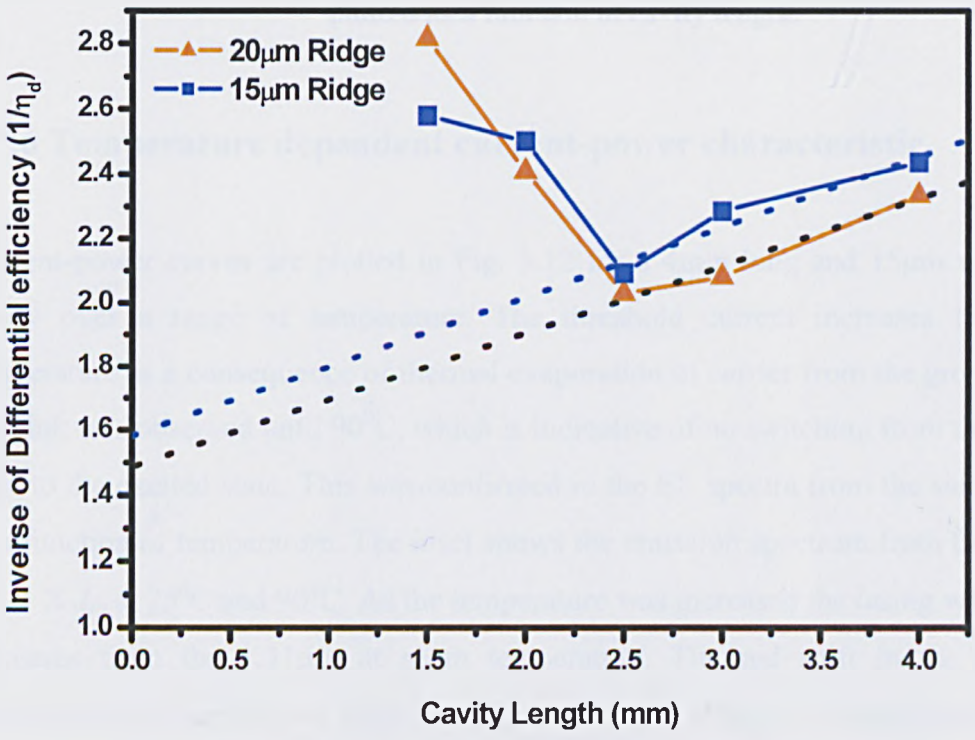

Fig. 3.10 Inverse differential efficiency plotted as a function of device length for 15 and 20 micron ridges

~1x10^{11} cm^{-2} is expected to participate in lasing at 1.31 μm. Detailed explanation is given elsewhere [30]. For the 0.5mm cavity the sum of the mirror loss and the cavity losses are ~ 25 cm^{-1}. The higher degeneracy of the excited state can be expected to result in the saturated gain of 26 -30 cm^{-1} as it is assumed that the ES has 4X the degeneracy of the GS. The fact is that no lasing is observed for this shorter cavity. This indicates the excited state saturated gain is $\leq$ 30 cm^{-1}.

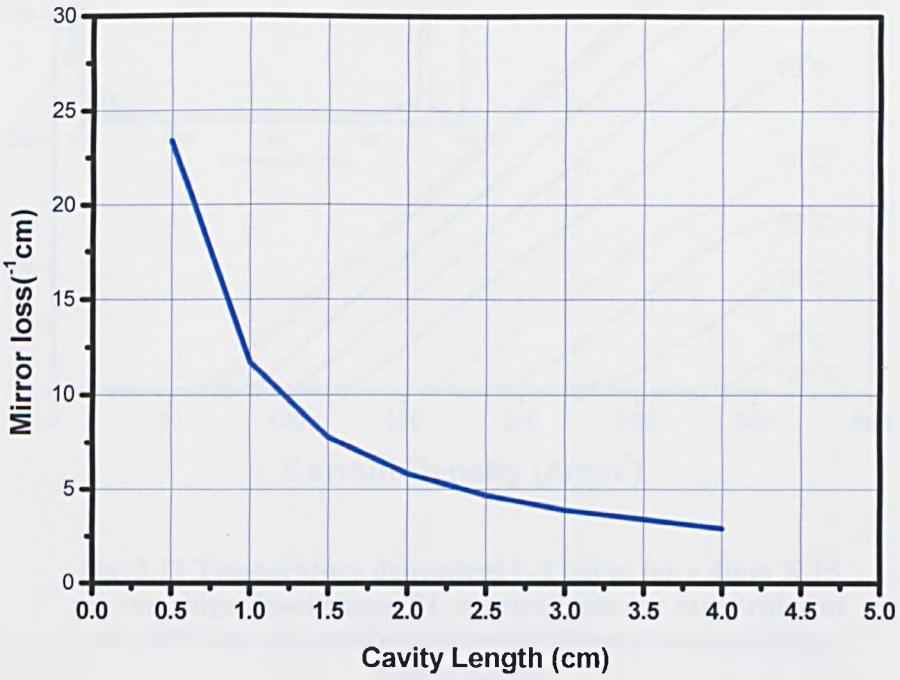

Fig. 3.11 Mirror loss of a Fabrey-Perrot laser plotted as a function of cavity length.

3.7.6 Temperature dependent current-power characteristic

Current-power curves are plotted in Fig. 3.12 for a 4mm long and 15μm wide laser cavity over a range of temperature. The threshold current increases for higher temperature as a consequence of thermal evaporation of carrier from the ground state. No kink was observed until 90^{0}C, which is indicative of no switching from the ground state to the excited state. This was confirmed in the EL spectra from the same device as a function of temperature. The inset shows the emission spectrum from this device at 1.1 X J_{th} at 25^{0}C and 90^{0}C. As the temperature was increased the lasing wavelength increases from the 1.31μm at room temperature. The red shift in the emission wavelength is observed due to the band gap reduction at higher temperatures. Lasing

was observed completely from the ground state at a temperature as high as 120^{0}C [31]. Above this temperature laser oscillation was not observed.

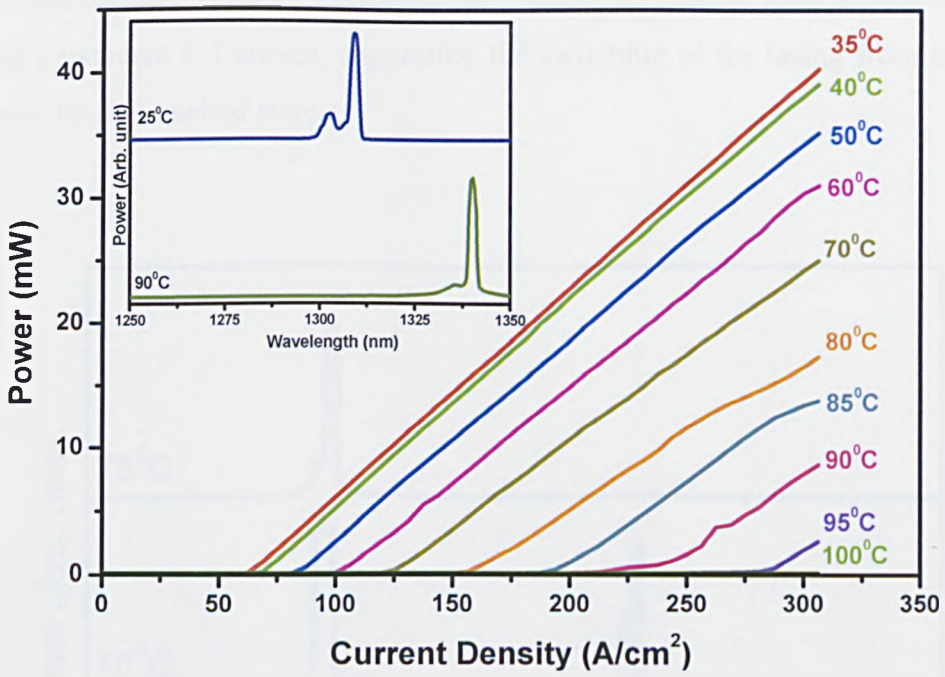

Fig. 3.12 Temperature dependent L-I curve for a 4mm X 15 micron ridge. Inset shows EL spectra from the same ridge at two different temperatures showing ground state emission with red-shift

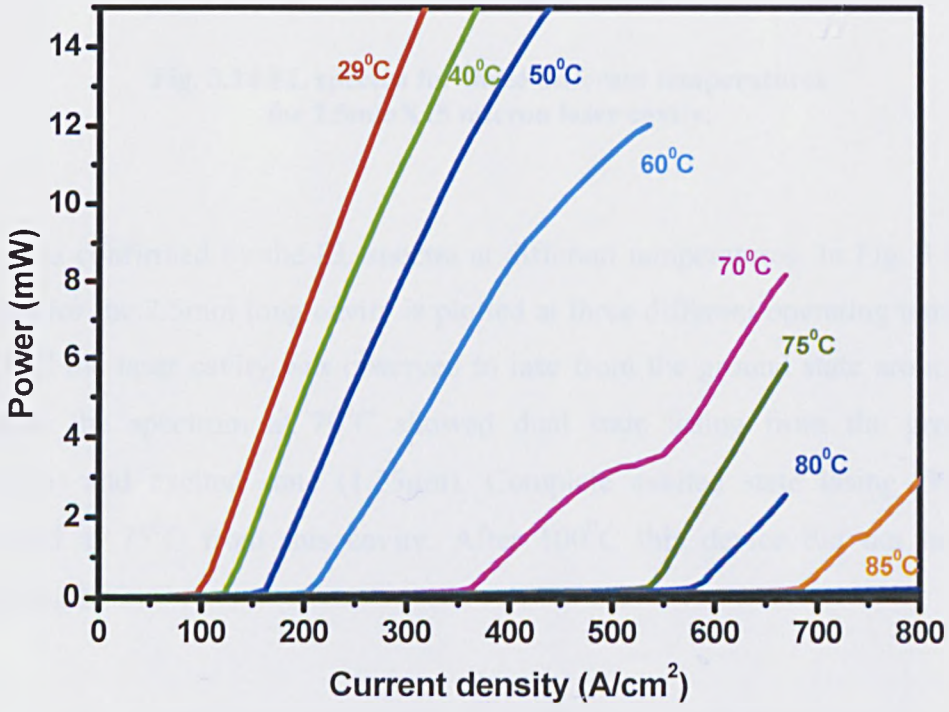

Fig. 3.13 Current-power characteristics as a function of temperature for a 2.5mmX15 micron laser cavity

Figure 3.13 shows the temperature dependent current-power characteristics of a 2.5mm long cavity. The threshold current density was observed to increase with the increase of temperature. The lasing was observed from the ground state until 70^0C. The current-power characteristics at 70^0C shows a similar kink as shown for the length dependent L-I curves, suggesting the switching of the lasing from the ground state to the first excited state.

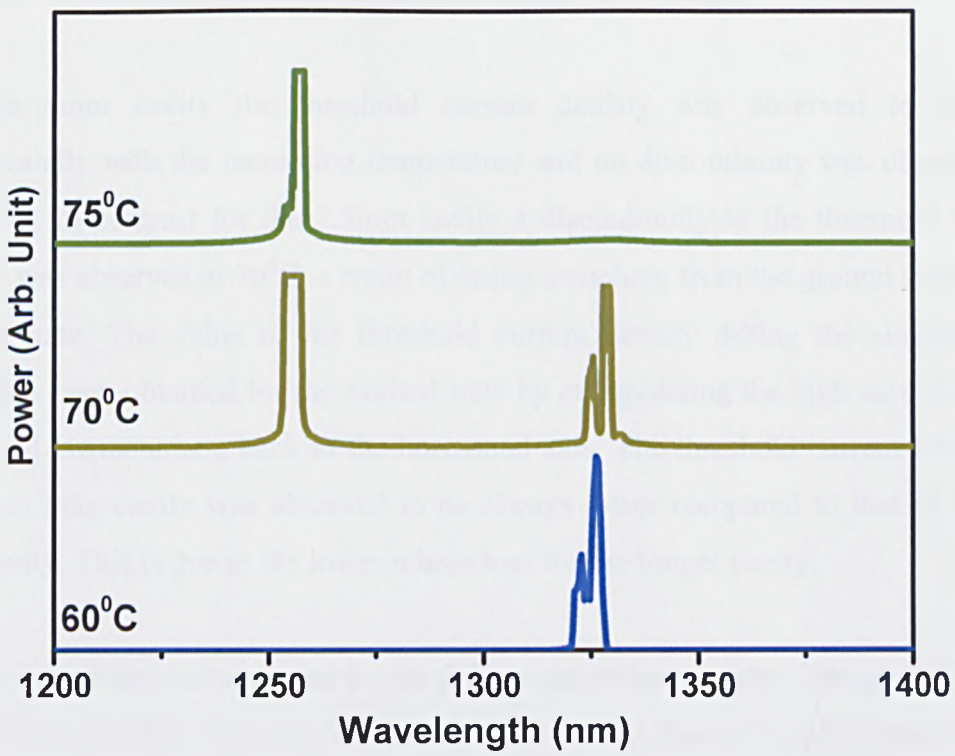

Fig. 3.14 EL spectra for three different temperatures for 2.5mmX15 micron laser cavity.

This was confirmed by the EL spectra at different temperatures. In Fig. 3.14 the EL spectra for the 2.5mm long cavity is plotted at three different operating temperatures. At 60^0C the laser cavity was observed to lase from the ground state around 1.32μm whereas the spectrum at 70^0C showed dual state lasing from the ground state (1.32μm) and excited state (1.25μm). Complete excited state lasing (1.25μm) is observed at 75^0C from this cavity. After 100^0C this device did not lase at any wavelength.

3.7.7 Comparative study of different figure of merits as a function of temperature

Various figures of merit have been extracted from the current-power characteristics and electroluminescence spectra for device with 4mm and 2.5mm long cavities. The ridge width for both of them was 15μm. The external differential efficiency (η_d), threshold current density (J_{th}) and peak wavelength of emission is plotted as a function of temperature for different cavity lengths in Fig. 3.15.

For the 4mm cavity the threshold current density was observed to increase exponentially with the increasing temperature and no discontinuity was observed up to 100^0C. In contrast for the 2.5mm cavity a discontinuity in the threshold current density was observed at 70^0C, a result of lasing switching from the ground state to the excited state. The value of the threshold current density during the simultaneous lasing has been obtained for the excited state by extrapolating the high current region of the L-I characteristic back to the horizontal axis. The threshold current density of the 4mm long cavity was observed to be always lower compared to that of 2.5mm long cavity. This is due to the lower mirror loss for the longer cavity.

Similar behaviour was observed for the differential efficiency plot. The plotted values of the external differential efficiencies are from two as cleaved facets of the cavities. At lower temperature the differential efficiency of the 2.5mm cavity showed greater efficiency in converting the electron-hole pairs into photons. But after 45^0C the 2.5mm cavity was seen to be less efficient than the 4mm long cavity. This is attributed to Pauli-blocking and gain saturation leading to carriers contributing to gain at the ES rather than photons within the lasing mode.

For the 4mm long cavity only a small change in the value of the threshold current density and the differential efficiency was observed up to 100^0C. In contrast the 2.5mm cavity exhibited a more pronounced reduction in the external differential efficiency together with a large increase in the threshold current density. The spectra for these two devices were taken at $1.1J_{th}$. The emission wave length for the 2.5mm long device switches from 1.33 to 1.26μm at 70^0C. The similar wavelengths and the

rate of change of wavelength with temperature in Fig. 3.15 indicate that the dominant process affecting the lasing wavelength is the temperature, with carrier density effects making a smaller contribution.

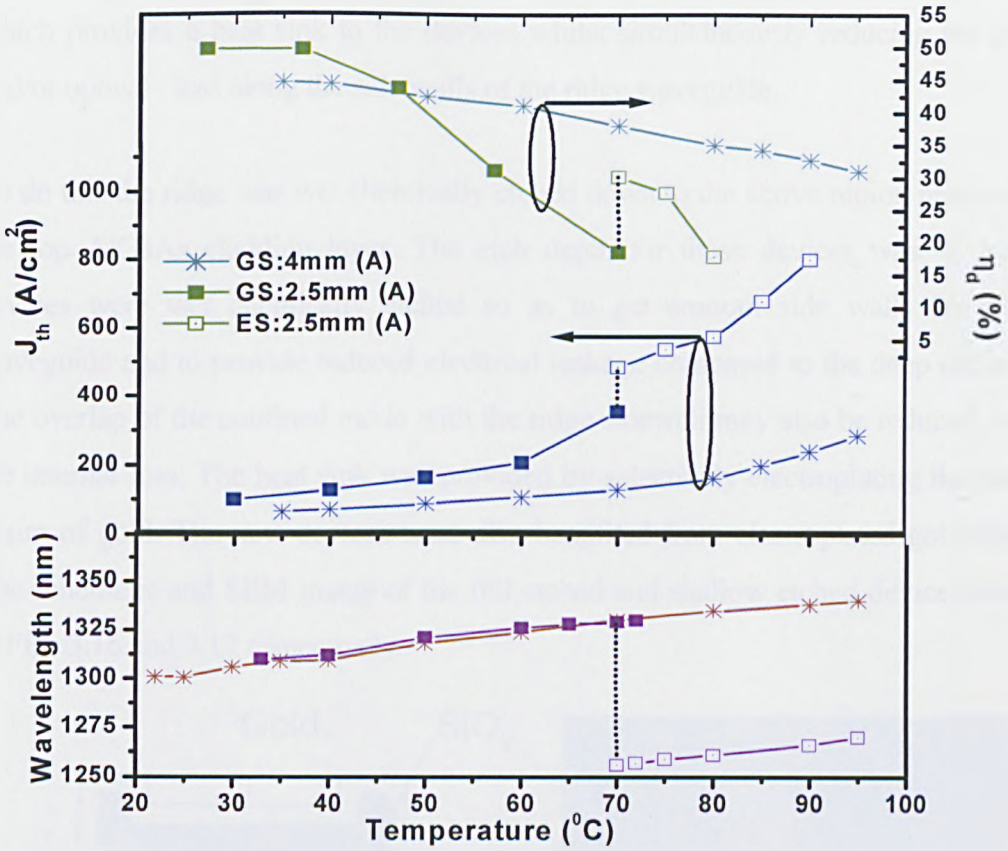

Fig. 3.15 Threshold current density and external differential efficiency of a 2.5mm and a 4mm long ridge plotted as a function of temperature. The bottom curve shows the change in peak wavelength of emission with temperature

The increased temperature sensitivity of 2.5mm-long cavity device is attributed to a comparatively higher excited state carrier population. The average dot carrier occupancy increases with decreasing cavity length, as a higher threshold gain is required. Even for ground state lasing, with the majority of carriers in the ground state, there will be a significantly higher occupation of the excited state in shorter cavity devices. This is due to a reduction in the carrier capture time of the ground state due to Pauli blocking. As carriers in excited states are more likely to be lost from the dots by thermal excitation, increased excited state carrier occupancy can be expected to result in increased temperature sensitivity of the device.

3.8 Improved Temperature characteristics: New device fabrication method

In order to reduce the temperature sensitivity of the device a technique was adopted which provides a heat sink to the devices whilst simultaneously reducing the electrical and/or optical loss along the side walls of the ridge waveguide.

To do this the ridge was wet chemically etched down to the active region removing only the top AlGaAs cladding layer. The etch depth for these devices was ~1.7μm. The devices were wet chemically etched so as to get smooth side walls for the ridge waveguide and to provide reduced electrical leakage compared to the deep etched ridge. The overlap of the confined mode with the ridge sidewall may also be reduced, reducing the internal loss. The heat sink was provided by selectively electroplating the device by ~3μm of gold. The new devices were also benefited from electroplated gold bondpads. The schematic and SEM image of the full etched and shallow etched devices are shown in Figs.3.16 and 3.17 respectively.

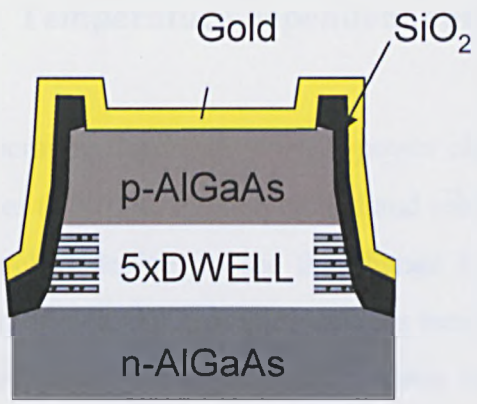

Fig. 3.16(a) Schematic diagram of the cross sectional view of a fully etched device

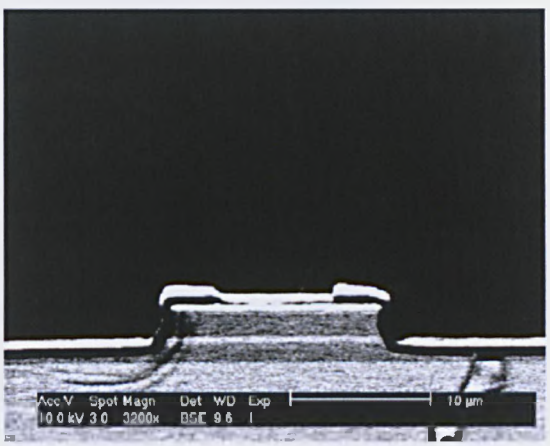

Fig. 3.16(b) SEM image of a ridge of VN61B

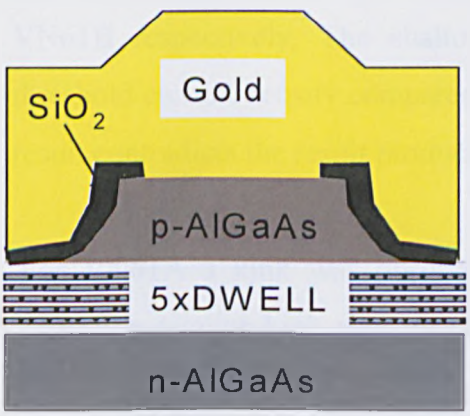

Fig. 3.17(a) Schematic diagram of the cross sectional view of a shallow etched and selectively electroplated ridge

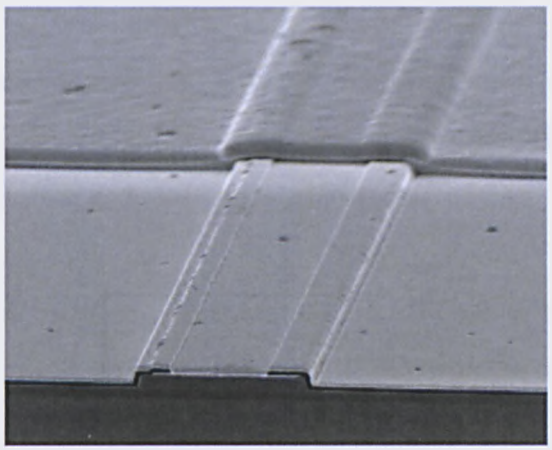

Fig. 3.17(b) SEM Image of a VN61A ridge, shows shallow etch and selective gold electroplating

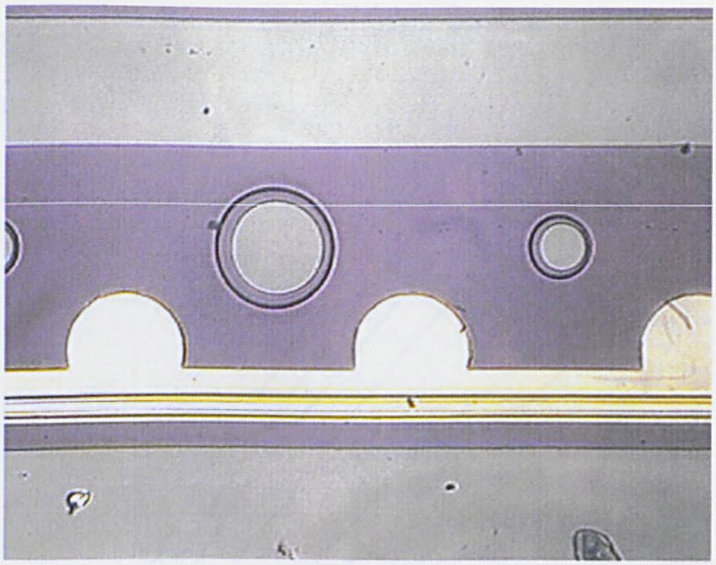

Fig. 3.18 Microscopic image of the fabricated VN61A laser ridge. Image shows the gold bond pads and mesa structures.

SEM inspection of the devices allowed the ridge widths and lengths to be measured precisely, and the selection of devices with good facets. Figure 3.16 shows a poor facet cleave, which leads to poor and unreliable laser characteristics.

3.8.1 Temperature dependent current-power characteristics

Temperature dependant current-power characteristic were measured for both types of devices (VN61A, shallow etched and selectively electroplated device and VN61B, the full etched device) to see the change in operating characteristics of VN61A. Two 2.5mm long and 15μm wide devices were chosen for each type of devices which were representative of devices on the same bar with good cleaved facets. The operating temperature was increased and the L-I was taken from the as cleaved facet. During the measurement the temperature was observed to vary slightly by $\pm 2^0$C. The corresponding graphs are shown in Fig 3.19(a) and Fig. 3.19(b) for VN61A and VN61B respectively. The shallow etched device had always exhibited a lower threshold current density compared to the fully etched device at any temperature. This result contradicts the result produced by another group in 2003. [16].

For VN61A a kink was observed at an operating temperature of 80^0C. For the VN61B a similar kink was observed at 70^0C corresponding to a transition to the

excited state [26]. The kinks occurring at different temperatures are characteristics of GS/ES switching.

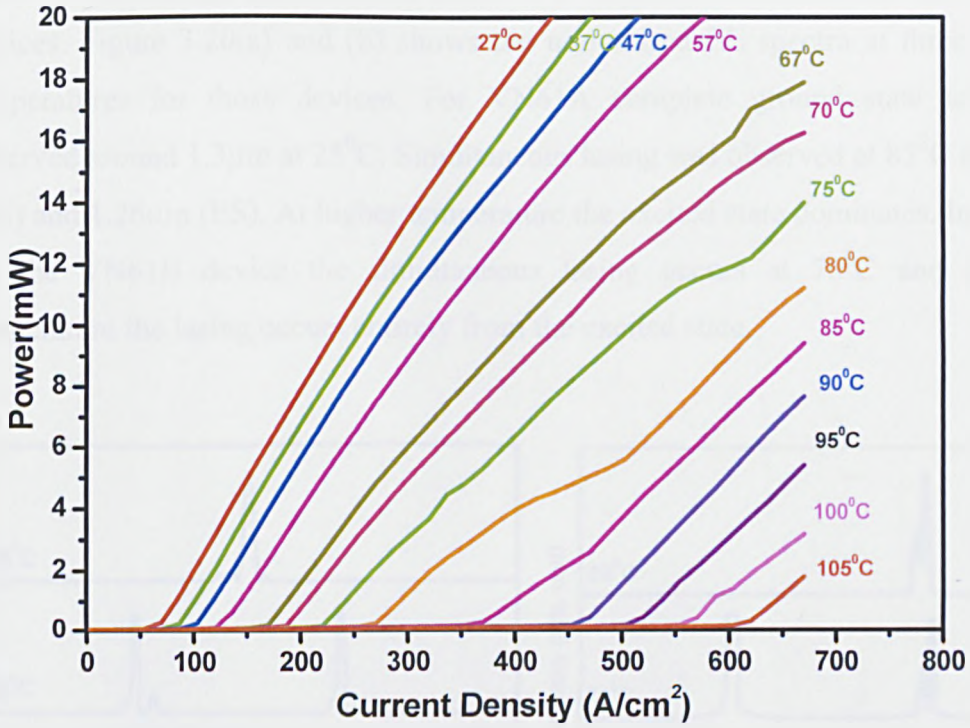

Fig. 3.19(a) Temperature dependent current-power curve for a 2.5mm X 15μm shallow etched and selectively electroplated laser.

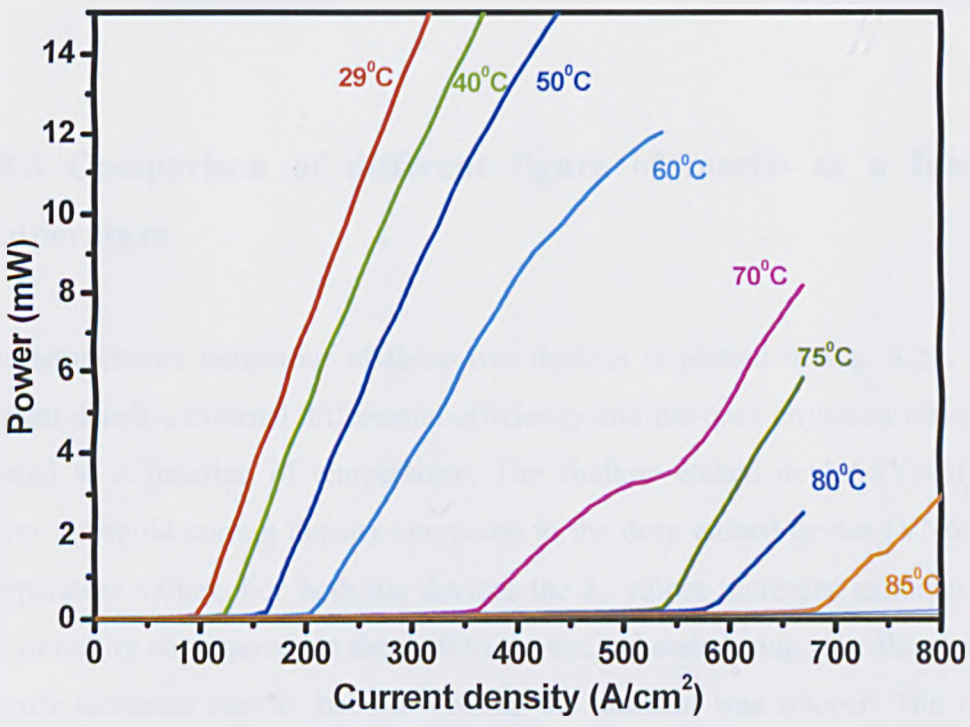

Fig. 3.19(b) Temperature dependent current-power curve for a 2.5mmX15μm deep etched laser.

3.8.2 Electroluminescence spectra at different temperatures

Electroluminescence spectra were taken as a function of temperature for the same devices. Figure 3.20(a) and (b) shows the normalised EL spectra at three different temperatures for those devices. For VN61A complete ground state lasing was observed around 1.3μm at 25^{0}C. Simultaneous lasing was observed at 85^{0}C at 1.33μm (GS) and 1.26μm (ES). At higher temperature the excited state dominates. In contrast, for the VN61B device the simultaneous lasing occurs at 70^{0}C and at higher temperature the lasing occurs entirely from the excited state.

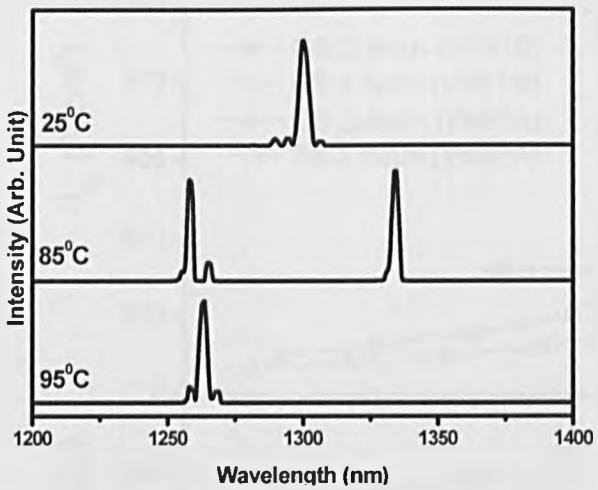

Fig. 3.20(a) EL spectra for a 2.5mm X 15μm VN61A laser at three different temperatures.

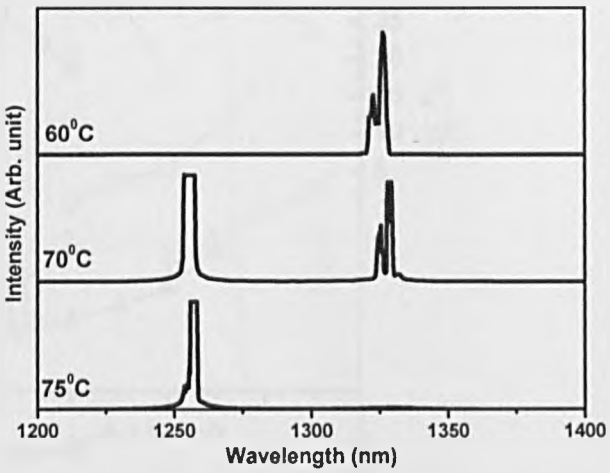

Fig. 3.20(b) EL spectra for a 2.5mm X 15μm VN61B laser at three different temperatures.

3.8.3 Comparison of different figure of merits as a function of temperature

The temperature behaviour of these two devices is plotted in Fig. 3.21. Threshold current density, external differential efficiency and the peak emission wavelength are plotted as a function of temperature. The shallow etched device (VN61A) shows lower threshold current density compared to the deep etched device (VN61B) for all temperature values. For both the devices the J_{th} values increases exponentially. The discontinuity corresponds to the shift to the excited state lasing. The threshold current density increases rapidly but for VN61B the gradient was steeper. The differential

efficiency for VN61A was observed to be higher at higher temperatures and switches to the excited state at 80^0C, where as that for VN61B switched at 70^0C.This phenomenon was evidenced from the peak emission wavelength plot as a function of temperature. The spectra for both the devices were taken at $1.1J_{th}$. Both devices were observed to emit at almost same ground-state and excited state wavelength, and the rate of red shift with the temperature was almost the same [30].

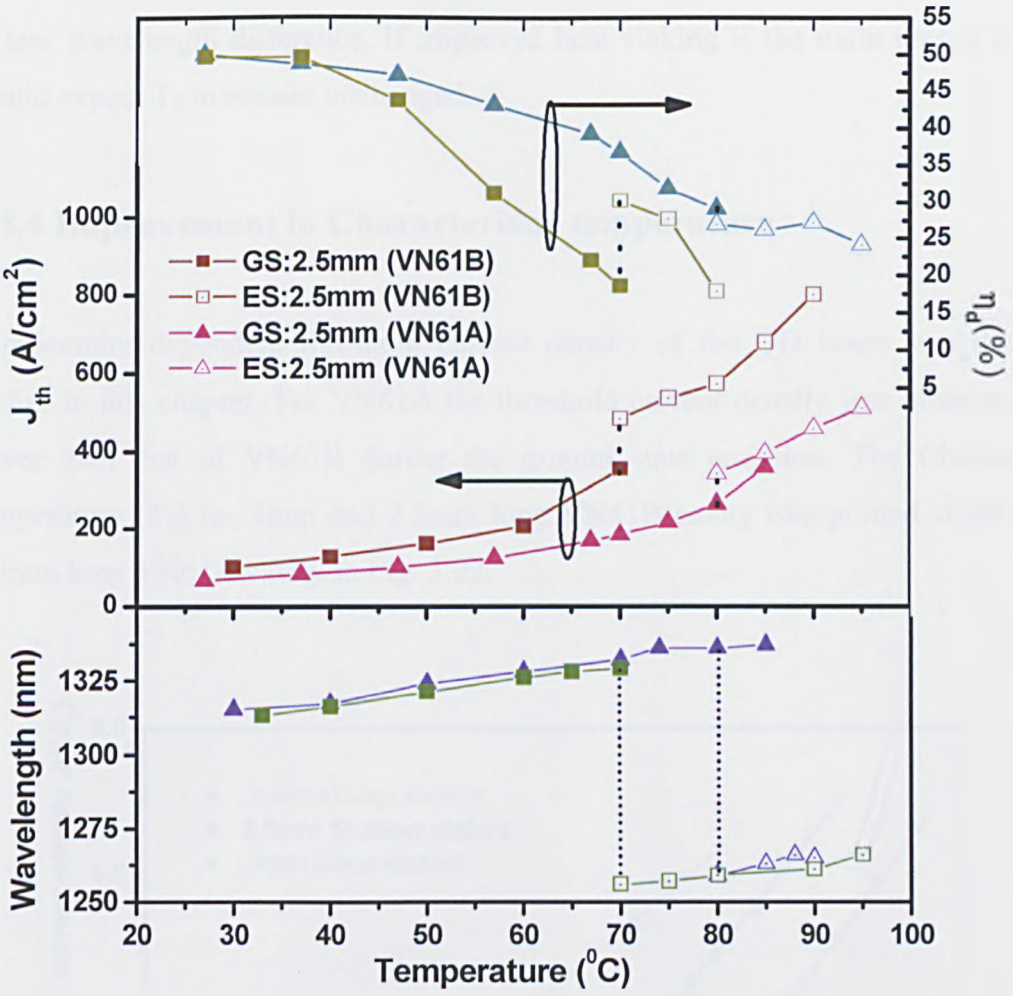

Fig. 3.21 Threshold current density, external differential efficiency and the peak wavelength of a 2.5mm long VN61A and VN61B cavity plotted as a function of temperature. Bottom curve shows the peak emission wavelength plot as a function of temperature.

It is evident from these results that the new device fabrication method allows the shallow etched and selectively electroplated device to lase from the ground state at a higher temperature. From this set of devices the relative effects of the different improvements expected is difficult to de-convolute. One key thing to notice here is that the devices don't switch to the excited state at a particular wavelength, which

could give the indication of switching occurring at identical cavity temperatures [26]. If this were the case, the improved heat sinking due to the electroplated gold bond-pad may be attributed to be the key factor in improved device performance. A ~10 degree difference in cavity temperature would be expected to result in a ~5nm difference in lasing wavelength. As is shown later, VN61B device exhibits lasing ~3nm shorter than VN61A, which is a shift in the wrong direction if entirely due to the heat sinking. Non uniformity of the QD wafer is more likely to cause the lower-to-lase wavelength difference. If improved heat sinking is the main reason then we would expect T_0 to remain unchanged.

3.8.4 Improvement in Characteristic temperature

Temperature dependent threshold current density of the QD lasers was discussed earlier in this chapter. For VN61A the threshold current density was observed to be lower than that of VN61B during the ground state emission. The Characteristic temperature (T_0) for 4mm and 2.5mm long VN61B cavity was plotted along with a 2.5mm long VN61A cavity in Fig. 3.22.

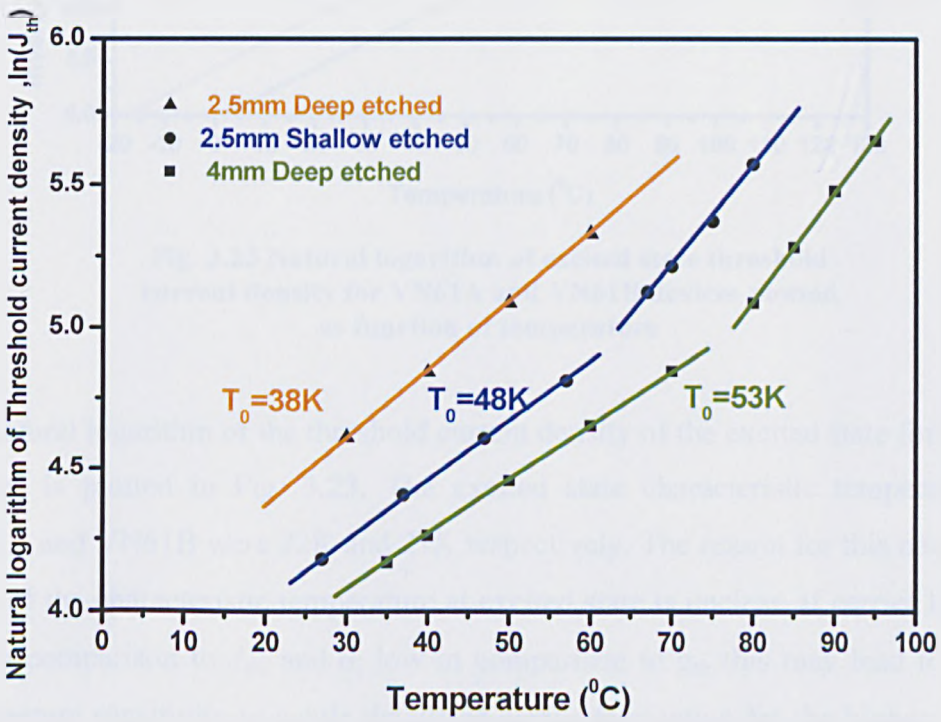

Fig. 3.22 Natural logarithm of threshold current density for VN61A and VN61B devices plotted as function of temperature to give the characteristic temperature (T_0)

The measured T_0 for the longer VN61B device was 53K and that of 2.5mm was 38K. A lower T_0 is generally associated with lasing from the excited state as the carrier loss due to thermal excitation is more efficient from the higher states. This explains the higher T_0 obtained for the 4mm long cavity. For VN61A device the characteristic temperature was 48K, which is 10K more than the VN61B device in the temperature range 20^0C to 70^0C and showed a clear improvement in the temperature characteristics due to the new fabrication method [26].

This is attributed to the reduced threshold current density due to reduced current leakage, optical loss (internal efficiencies) and the incorporation of better heat sink.

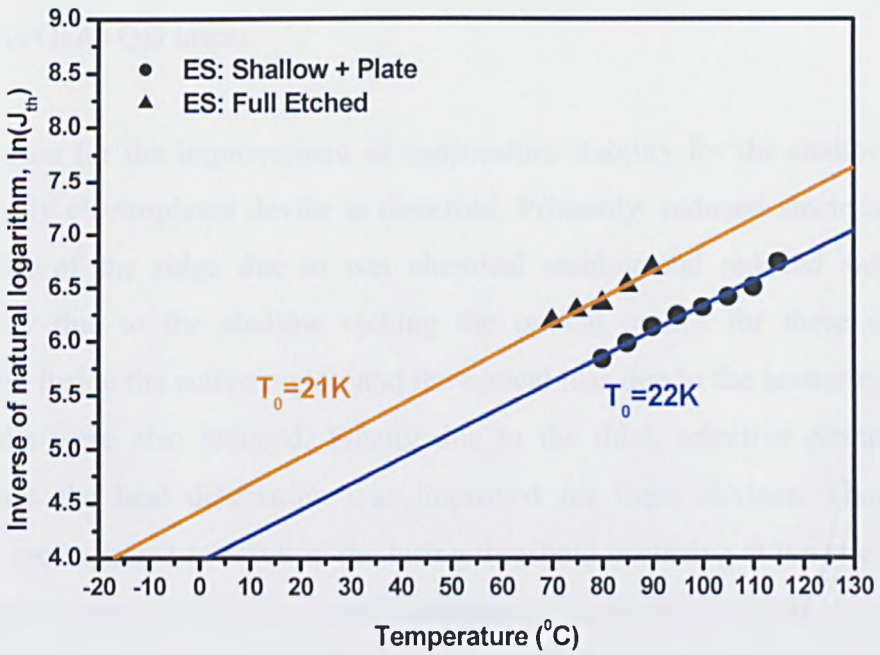

Fig. 3.23 Natural logarithm of excited state threshold current density for VN61A and VN61B devices plotted as function of temperature

The natural logarithm of the threshold current density of the excited state for the same devices is plotted in Fig. 3.23. The excited state characteristic temperatures for VN61A and VN61B were 22K and 21K respectively. The reason for this nearly equal value of the characteristic temperature at excited state is unclear. If carrier leakage is low in comparison to J_{th}, and α_i low in comparison to g_{th} this may lead to reduced temperature sensitivity to subtle details of device fabrication for the higher J_{th} , high g_{th} excited state emission.

3.9 Conclusion

Through the study of different parameters characterising QD lasers, it has been realised that the incorporation of shallow ridge etch and selective gold electroplating has reduced the threshold current density at any temperature and in turn the external differential efficiency has also increased compared to deep etched device. Also it was observed that the rate of change of the J_{th} and η_d with increasing temperature both for ground state and excited state lasing was reduced. For the shallow etched and selectively electroplated device the characteristic temperature was increased to 48K and the temperature at which exclusively excited state lasing was observed was increased to 95^0C. These values clearly indicate reduced temperature sensitivity for the InAs/GaAs QD lasers.

The reason for the improvement in temperature stability for the shallow etched and selectively electroplated device is threefold. Primarily, reduced electrical loss at the sidewalls of the ridge due to wet chemical etching and reduced sidewall depth. Secondly due to the shallow etching the optical modes for these devices were confined inside the active region and the optical loss due to the scattering at the ridge sidewalls were also reduced. Finally due to the thick selective electroplated gold bondpads the heat dissipation was improved for these devices. These combined effects are expected to result in the lasing threshold occurring at lower carrier density and hence lower average dot carrier occupancy, at all temperatures. As a result there is a concomitant reduction of the occupancy of the excited state of the QDs leading to an improved tolerance to increasing temperature.

3.10 Further work

One key aspect worthy of further investigation is the process by which lasing from the ground state is quenched after dual state lasing takes place. The ground state emission was observed to be turned off completely at a higher drive current when the excited state emission dominates. According to theory, the ground state component should get clamped and the excess injected carriers should contribute to excited state

lasing, but in reality the ground state component becomes suppressed rapidly with increasing drive current. The reason for this is unknown and requires further investigation. A number of reasons have been put forward to explain this phenomena but no consensus exists. A strong increase in homogeneous broadening has been postulated, as has some ill-defined ground-state depopulation mechanism. If this switching mechanism can be understood, it may lead to new types of device utilising this phenomena. It is predicted that the gain measurement of a short cavity laser can shed some light on this issue.

References

1> M. Asada, Y. miamoto, Y. Suematsu ; IEEE J. Quantum Electron. QE-22 1915 (1986).

2> M. Sugawara, N Hatori, T Akiyama, Y Nakata, H Ishikawa. Jpn. J. Appl. Phys. 40, L488, (2001).

3> A. R. Kovsh, A. E. Zhukov, D. A. livshits , A. Yu Egorov, V. M. Ustinov, M. V. Maximov, Yu. G. Musikhin, N.N. Ledentsov, P. S. Kop'ev. Zh .I. Alferov, D. Bimberg. Electron. Lett. 35, 1161 (1999).

4> H. Y. Liu, M. Hopkinson, C. N. Harrison, M.J.Steer, R. Firth, I. R. Seller, D. J. Mowbrey and M. S. Skolnick, J.Appl.Phys. 93 2932 (2003).

5> N. Kirstaeder, N. N. Ledentsov, M. Grundmann, D. Bimberg, V. M. Ustinov, S. S. Rubimov, M. V. Maximov, P. S. Kop'ev, Zh .I. Alferov, U. Richter, P. Werner, U. Gosele, J. Heydenreich, Appl. Phys. Lett, 69, 1226 (1996).

6> P. B. Joyce, T. J. Krzyzewski, G. R. Bell, T. S. Jones, S. Mali, D. T. Childs, R. Murray, Phys Rev. B. 62, 10891 (2000).

7> K. Nishi, H. saito, S. Sugou, J-S Lee, Appl. Phys. Lett, 74, 1111 (1999).

8> A. E. Zhukov, A. R. Kovsh, A. Yu Egorov, N. A. Maleev, V. M. Ustinov, B. V. Volvik, M. V. Maximov, A. F. Tsatsul'nikov, N.N. Ledentsov, Yu. M. Shernyakov, A. V. Lunev, Yu. G. Musikhin, N. A. Bert, P. S. Kop'ev, Zh .I. Alferov, Semiconductors 33, 153 (1999).

9> L. F. Lester, A. Stintz, H. Li, T. C. Newell, E. A. Pease, B. A. Fuchs,K. J. Malloy, IEEE Phot. Tech. Lett. Vol 11, 931, (1999).

10> Q. Xi, A. Madhukar, P. Chen,, N. P. Kobayashi, Phys. Rev. Lett, 75, 2542 (1995).

11> N.N. Ledentsov, V. A. Shchukin, M. Grundmann, N. Kirstaedter, J. Bohrer, O. Schmidt, D. Bimberg, V. M. Ustinov, A. Yu Egorov, A. E. Zhukov, P. S. Kop'ev, S. V. Zaitsev, N. Yu. Gordeev, Zh .I. Alferov, A. I. Borovkov, A. O. Kosogov, S. S. Rubimov, P. Werner, U. Gosele, J. Heydenreich, Phys Rev B 54 8743 (1996).

12> Y. Arakawa, H. Sakaki Appl. Phys. Lett. 40 939 (1982).

13> T. Takahashi, Y. Arakawa, Optoelectronics-Devices & Technol. 3, 155 (1988).

14> O.B. Schekin, D. G. Deppe, IEEE Photon. Technol. Lett, 9, 1231 (2002).

15> O. B. Schekin, D. G. Deppe, Appl. Phys. Lett. 80, 3277 (2002).

16> D. Ouyang, N. N. Ledentsov, D. Bimberg, A. R. Kovsh, A. E. Zhukov, S. S. Mikhrin, V. M. Ustinov, Semicond. Sci. Technol. 18 L53-L54 (2003).

17> H. Y. Liu, M. Hopkinson, C. N. Harrison, M.J.Steer, R. Firth, I. R. Seller, D. J. Mowbrey and M. S. Skolnick, J.Appl.Phys. 93, 2932 (2003).

18> I. Mukhametzhanov, Z. Wei, R. Heitz, A. Madhukar, Appl. Phys. Lett 75, 85 (1999).

19> H. Y. Liu, B. Xu, Y. H. Chen, D. Ding, Z. G. Wang. J. Appl. Phys 88, 5433 (2000).

20> D. L. Huffaker, G. Park, Z. Zou, O. B. Shchekin, D. G. Deppe, IEEE J. Sel. Top. Quantum Electron. 6, 452 (2000).

21> J. X. Chen, U. Oesterle, A. Fiore, R. P. Stanley, M. Ilegems, T. Todaro, Appl Phys. Lett 79, 3681 (2001).

22> H. Y. Liu, I. R. Seller, M. Gutierrez, K. M. Groom, W. M. Soong, M. Hopkinson, J. P. R. David, R. Beanland, T. J. Badcock, D. J. Mowbray, M. S. Skolnick, J. Appl. Phys, 96 No 4, 15 (2004).

23> A. Markus, J. X. Chen, C. Parantheon, C. Platz, O Gauthier Appl. Phys. Lett. 82, 1818 (2003).

24> G. Park, O.B. Shchekin, D.L. Huffaker, D.G. Deppe. IEEE Photonics Technology Lett. 13, 230, (2000).

25> A. R. Kovsh, N. A. Maleev, A.E. Zhukov, S. S. Mikhrin, A. P. Vasil, E. A. Semenova, Yu. M. Shernyakov, M.V. Maximov, D.A. Livshits, V.M. Ustinov, N.N. Ledentsov, D. Bimberg, Zh. I. Alferov. Jrnl. Of Crystal Growth 251 (2003) 729-736.

26> S. K. Ray, K. M. Groom, R. A. Hogg, H.Y. Liu, I R. Sellers, M. Hopkinson, T. J. Badcock, A. J. Ramsay, D. J. Mowbray, M. S. Skolnick, Jpn. Jrnl. Of Appl. Phys. 44 (4B), 2520-2522, (2005).

27> A.E. Zhukov, A. R. Kovsh, D.A. Livshits, V.M. Ustinov, Zh. I. Alferov, Semicond. Sci. Technol, 18, 774-781, (2003).

28> I. N. Kaiander, R. L. Sellin, T. Kettler, N.N. Ledentsov, D. Bimberg, N. D. Zakharov, P. Werner. Appl. Phys. Lett. 84, 2992, (2004).

29> X. Huang, A. Stintz, C.P. Hains, G.T Liu, J Cheng, K.J. Malloy. IEEE Photon. Technol Lett. 12, 227, (2000).

30> A. Markus, J. X. Chen, C. Paranthoen, A. Fiore, C. Platz, and O. Gauthier-Lafaye, Appl. Phys. Lett. Vol. 82, 1818, (2003).

31> S. K. Ray, K. M. Groom, R. A. Hogg, H. Y. Liu, M. Hopkinson, T. J. Badcock, D. J. Mowbray, M. S. Skolnick, IEEE Photon. Technol. Lett. Vol. 17, No. 9, (2005).

Chapter 4: Publications came out of this work

Journal publications:

1> S. K. Ray, K. M. Groom, M. D. Beattie, H. Y. Liu, M. Hopkinson, R. A. Hogg *"Broad-band Superluminescent Light Emitting Diodes Incorporating Quantum Dots in Compositionally Modulated Quantum Wells"*. IEEE Photon.Technol. Lett. Vol. 18, Issue 1, 58-60. (Jan.1 2006).

2> S. K. Ray, K. M. Groom, R. Alexander, K. Kennedy, H. Y. Liu, M. Hopkinson, R. A. Hogg *"Design, Growth, Fabrication and Characterisation of InAs/GaAs 1.3μm Quantum Dot Broadband Superluminescent LED"*. Jrnl. Of Appl. Phys. (Accepted for publication).

3> S. K. Ray, K. M. Groom, H. Y. Liu, M. Hopkinson, R. A. Hogg *"Broad-band Superluminescent Light Emitting Diodes Incorporating Quantum Dots in Compositionally Modulated Quantum Wells"*. Jpn. Jrnl. of Appl. Phys., Vol. 45 No. 4A, (2006).

4> K. M. Groom, S. K. Ray, H. Y. Liu, M. Hopkinson, R. A. Hogg *"Flat-Topped Emission Centered at 1250nm from Quantum Dot Superluminescent Diodes"* (Submitted to Electron. Lett.).

5> K. M. Groom, S. K. Ray, T. Choi, B. Stevens, H. Liu, M. Hopkinson, R. A. Hogg, *"High-Power and Broad-Band Quantum Dot Superluminescent diodes Centred at 1250nm for Optical CoherenceTomography"*. (Submitted to Jrnl. Of Sel. Topics in Quant. Electron.).

Poster and conference presentation:

1> Oral presentation, European Semiconductor Laser Workshop (ESLW) *"Broadband InAs/GaAs QD Superluminescent LEDs"*. 22-23rd Sept. 2005, Glasgow, Scotland.

2> Oral presentation EPMDS 2006, *"Broadband Quantum Dot Superluminescent Diode"*. 4-6th January 2006, Kolkata, India.

3> Oral presentation CLEO/QELS *"Broadband and High Power Quantum Dot Superluminescent Diodes"*. 21st-26th May 2006, Long Beach,CA, USA.

Chapter 4: 1.3μm InAs/GaAs Quantum Dot Superluminescent Light Emitting Diodes

4.1 Introduction to Quantum dot Superluminescent Light Emitting Diodes

In this chapter a technique is discussed for broadening the emission and gain spectra of 1.3μm quantum dot superluminescent LEDs (SLEDs). Methods to tailor the emission and gain spectra of the devices by incorporating different amounts of indium in different wells of a multi dot-in-well (DWELL) are discussed. These techniques allow the overlap of the ground state of one DWELL with the excited state of another to achieve broader and flatter emission spectra compared to a SLED design comprising DWELL layers of constant quantum well indium composition. Due to the low internal loss of these structures, this broadening is achieved without a significant reduction in the output power of the device. I go on to discuss a related study to achieve a flat topped emission spectrum.

Superluminescent light emitting diodes (SLEDs) are the ideal optical sources for applications which require high output power and a broad emission spectrum. They are of increasing interest for a range of applications such as optical coherence tomography (OCT), fiber-optic gyroscopes, and wavelength division multiplexing system testing. Recently, interest has focused upon applications in OCT for which cheap, compact, broadband, high power optical sources are required in order to realize low cost point of care screening and diagnostics [1]. Due to strong multiple scattering in skin tissue, operating wavelengths in the region of 1050nm and 1300nm are required as these correspond to the minimum in dispersion and loss for skin tissue, respectively. By appropriate scanning, ultra-high resolution two- or three-dimensional cross-sectional images of tissue may be obtained non-invasively and *in situ* [2]. The axial resolution of an OCT system is governed by the optical source coherence length L_c, which is inversely proportional to the bandwidth of the optical source.

4.2 Optical Coherence Tomography and its requirements

Optical coherence tomography (OCT) is an imaging technique that produces high resolution cross sectional images of optical reflectivity [3, 4]. It is based on the principle of low-coherence interferometry where distance information concerning various tissue structures is extracted from time delays of reflected signals. The excellent optical sectioning capability of OCT is achieved by exploiting the short temporal coherence of broadband light sources like SLEDs. This light source enables the system to take the image of the microscopic structure of the tissues at a depth beyond the reach of bright field microscopic system [1]. The block diagram of a typical OCT system is shown in Fig. 4.1.

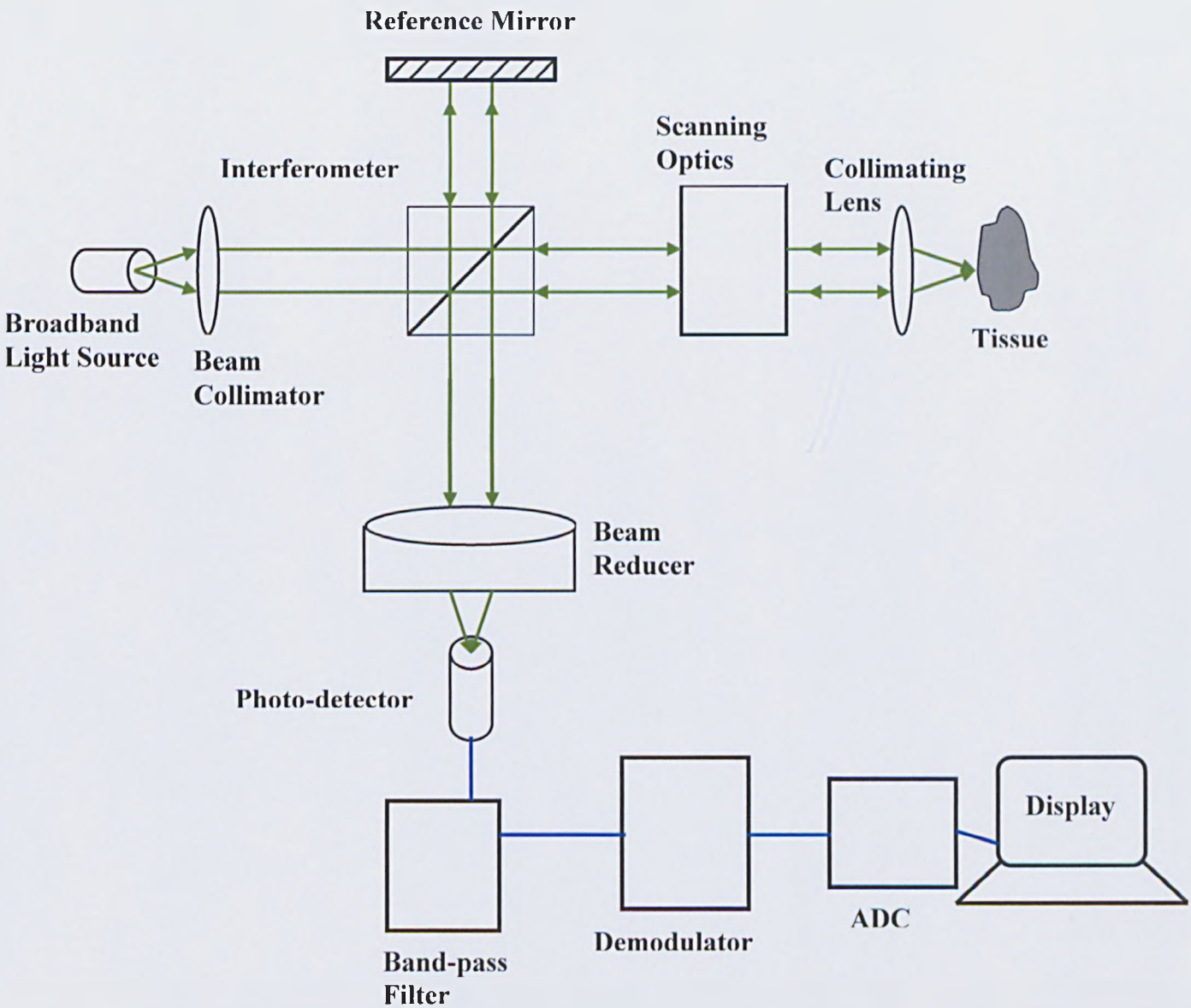

Fig. 4.1 Block diagram representation of a typical Optical Coherence Tomography system

In an OCT system the optical source should have a broad emission band and high output power. The light in the OCT system is split into two components. One arm of the interferometer focuses the light on the sample under observation and the second component is used as a reference through a movable mirror (In time domain OCT). The back scattered light from the sample and the reference arm combine at the photodetector to form an interference pattern. The amplitude of the interference fringes depend on a delay provided by the reference mirror [1] where translation interrogates a different depth within the sample under observation. Thus the interferometer acts as a cross correlator in between the reference signal and the sample signal and the amplitude of the interference signal generated after integration at the detector surface give the cross-correlation signal amplitude. Those portions of the sample which reflect strongly create a stronger interference envelope than the other portions. Any other light outside the short coherence length does not interfere. The cross-correlation signal is then separated from the dc component of the intensity of the source and the topographic map is obtained from the OCT system by a false colour scheme [3].

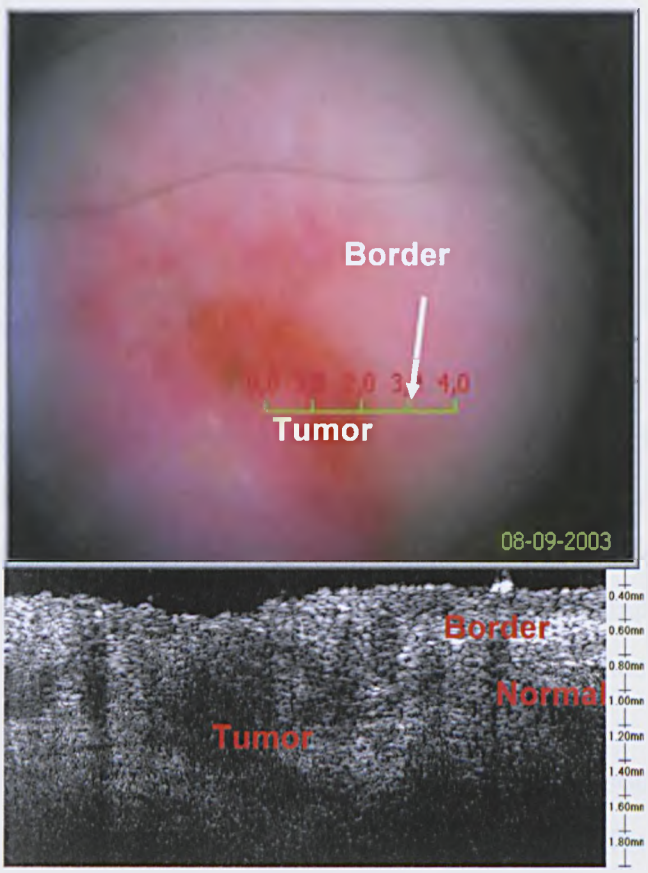

***Courtesy**: Peter E. Anderson, Riso National Laboratory, Denmark, for the OCT imag.*

Fig. 4.2 Real microscopic image of the cross section of a tumor and the OCT image of the same. Dark portion in the image indicates the tumor.

For cross-sectional images, bright colours correspond to areas of high reflectivity while darker colours correspond to areas of low reflectivity. For retinal thickness measurement, bright colours are assigned to areas with increased retinal thickening and darker colours are assigned to areas with less retinal thickness. An OCT image of a tumour is shown in Fig. 4.2. In this image the normal skin reflects maximum light to give a bright interference pattern and the abnormal growth portion reflects less light and observed in the dark portion of the OCT image.

4.2.1 Requirements of the optical source for OCT

There are three main requirements of the optical source for the OCT system. Firstly, the emission should be near infrared. The second requirement is the source should have a short temporal coherence length. Last of all high output optical power is required.

The reason for the wavelength to be in this region is the penetration depth of the light in the tissue. It has been observed that the deepest penetration has been achieved for the source emitting in between 1200nm and 1800nm [5, 6]. At wavelength greater than 2500nm the imaging to the similar depth is limited by the vibrational absorption by water. Also it is to be noted that at 1300nm the loss is minimised for the skin tissues. In this chapter the SLEDs are made to work around 1300nm for their minimum loss around this wavelength. This is also a convenient wavelength in terms of optical components and detectors.

The second requirement for the optical source is related to the contrast of the OCT image. More specifically, a shorter coherence length source is required (i.e. a broader emission bandwidth of the source). This gives better axial resolution and contrast of the OCT image. Also the shape of the spectra is also an important factor because it affects the dynamic range of the system near strong reflections [7].

The third requirement is a high output power of the optical source. This is required for the wide dynamic range and high detection sensitivity for the imaging of weak backscattered light [1].

4.3 Background theory

Superluminescence is the optical property of a semiconductor device, which is due to amplified spontaneous emission due to gain within the active region of the device. The structure of a superluminescent diode is almost the same as a ridge waveguide laser; the only difference being the ridge is tilted to a small angle to the facet so as to inhibit the regenerative feedback produced in the gain medium. The regenerative feedback is inhibited to prevent the device lasing and in turn the power increases superlinearly with the applied bias if gain and spontaneous emission are linear in current density. The current-power characteristics of such a SLED can be divided into three different regions. At low currents the spontaneous emission dominates and the power increases linearly with the drive current. With increasing current the power increases exponentially with the current as the stimulated emission combines with the spontaneous emission. Finally, at higher currents the spontaneous emission starts dominating and as the regenerative feedback is suppressed due to the tilted ridge waveguide structure the power starts increasing superlinearly with the drive current and no clear threshold like a laser diode is observed [8]. The output power for a SLED can be expressed as:

$$P=P_0/\beta\,(e^{\beta L}-1) \qquad (1)$$

Where, L is the length of the SLED, β is the net gain coefficient and P_0 is radiated spontaneous power in a small element of the material and has a linear relationship with the injected current by the following relationship:

$$P_0=\eta_{SP}(h\upsilon/q)\,J.2b.\Omega \qquad (2)$$

This equation is true for ideal QW structures where gain and spontaneous emission are well approximated by a linear relationship. In this equation η_{SP} is the spontaneous efficiency, J is the injected current density, b is the width of the excitation region and Ω is the ratio of the power captured by the waveguide provided by the heterostructure to the total spontaneous emission [8].

The expression in equation (1) shows an exponential dependence of the power with the injected current density J. Such a superlinear increase in power with drive current is characteristics of a superluminescent diode. For QD active regions, spontaneous emission and gain may be saturated at low currents. We may therefore expect the superlinear response of the device to be lost at high drive currents.

In addition to a broad emission band-width, a key requirement from these devices is a high output power. Many groups have suggested different methods to achieve high output power and those methods are discussed in chapter 5 of this thesis. One of the main problems encountered by several groups is the tendency of lasing of the SLEDs. At sufficiently high input currents the SLED structure can start lasing since the effective facet reflectivity is non-zero [8]. Once the effective mirror loss value is overcome by the gain provided by the gain media the device starts lasing. Besides the tilted ridge waveguide structure a tapered waveguide structure is another solution to this problem. The best method to stop the lasing and to extend the linear gain region of the L-I curve of the SLED is to provide an antireflective coating to the facets of the ridge. This has been proved to be an effective solution by several groups [9], but is problematic for broadband emitters

Another requirement for Superluminescent diodes for OCT is a large bandwidth. The Short coherence length for the device is required by many applications like OCT. The coherence length (L_c) of the SLED is related to the band width by the following relation:

$$L_c \approx \lambda^2/\Delta\lambda \qquad (3)$$

Where λ is the centre wavelength and the $\Delta\lambda$ is the bandwidth of the spectrum. In order to achieve a small coherence length for the light source the bandwidth should be large. In this chapter a method is discussed to achieve a broadband quantum dot superluminescent LED emitting around 1.3μm.

4.4 Previous work

The two important features for a superluminescent LED are broad emission bandwidth and the high output power. Large spectral width is important because it

corresponds to the low coherence length, which can significantly improve the spatial resolution in a coherence based system. Initially, the introduction of a QW as the active region exhibited promise to broaden the emission spectra of a SLED. These structures showed two to three fold increase in the spectral width of SLED compared to the conventional bulk double heterostructures [10].

Mikami *et al.* designed a structure of the SLED active region, which consisted of quantum wells of different bandgaps and obtained a spectral width of 80nm and 140nm for 1.3μm and 1.5μm devices, respectively. The same group proposed and exhibited a structure, which introduced the amplification of intrinsic spontaneous emission by n=1 and n=2 transitions simultaneously. A spectral width of 68 and 170nm were obtained for the AlGaAs SLED emitting at ~0.8μm and InGaAsP SLED emitting at ~1.5μm respectively [11, 12, 13]. There were some limitations of this design. The wide spectrum was obtained only for certain current densities, when the gains at n=1 and n=2 transitions were equal.

Another approach was made by Lin *et al.* [14] to broaden the spectra of a QW SLED structure. They designed an active region for the SLED with multiple quantum wells of different widths. The active region of those devices consisted of 4 chirped quantum wells. A spectral width of 91.5nm was obtained with the emission peak at 0.8μm. But the maximum spectral width reported so far is nearly 300nm [15]. In this work two $In_{0.53}Ga_{0.47}As$ QWs and three $In_{0.67}Ga_{0.33}As_{0.72}P_{0.28}$ QWs were used and a spectral range from 1.3μm to 1.585μm was covered, though the output power was not mentioned.

In recent years quantum dot lasers have drawn more attention for their potential for the high speed modulation, comparatively temperature insensitive behaviour and low threshold current density [16]. Also as a potential SLED material Quantum dots (QDs) have attracted attention due to their naturally broad emission spectrum from the ground state of the QDs [17-20] resulting from size fluctuations of the order of ~10%. A natural spectral broadening of tens of meV can be obtained due to the size fluctuation of the quantum dots. Several approaches were made the in last few years to widen the emission spectra of the quantum dot superluminescent LEDs. One of those approaches was to increase the dot size distribution [17] but to date the exact

control over the QD size is not possible and hence not reproducible. Other methods like single quantum wells [14] or the use of bulk material as the active regions [21] are other techniques which have been proposed in last few years. Also, for QD SLED devices, InAs and InGaAs QDs have been introduced into the same multi-QD layer structure [22] and chirped strain reducing layers have been utilised [23] to yield a broader emission spectrum. However, for these techniques, the resultant emission spectrum is a multi-gaussian, which is expected to impact upon the dynamic range of an OCT imaging system due to the presence of sidelobes in the interferogram [2]. For OCT system applications, a single Gaussian or flat topped emission spectrum is required.

In this chapter a novel concept for the broadening of the 1.3μm InAs/GaAs QD SLED emission band is described. The SLED device design relies upon a multi- dot-in-well (DWELL) structure with each DWELL having a *different* indium composition. These structures rely on the use of both excited state and ground state and the overlap of these bands for different [In] DWELLs. These structures are termed dots in compositionally modulated well (DCMWELL) structures. I describe the design, growth, fabrication, and operating characteristics of such SLED devices, which exhibit 85nm wide; almost flat emission spectrum while operated CW at room temperature with output powers of 2.5 mW. I also discuss the operating characteristics of laser devices fabricated from the same epitaxial material. Such lasers fabricated from these structures exhibit a gain spectrum of ~100nm. An extension of the concept is presented, where careful design allows a flat-topped emission spectrum to be realised.

4.5 Novel Idea for a Broadband Quantum dot SLED

In previous chapter it has been discussed that to achieve high quality 1.3μm QD laser material we have incorporated InAs QD in InGaAs quantum wells using a high temperature growth step during the formation of the quantum dots [24]. Also, in order to optimise the quality of the InAs quantum dots during the high temperature growth step we utilise two indium cells to deposit the InGaAs wells and the InAs dots separately [25]. This results in a very low threshold current density and very low transparency current density [26, 27, 28].

In order to tune the emission wavelength of our DWELL structures the indium composition in the QW of the DWELL is altered, with $In_{0.15}Ga_{0.85}As$ wells giving QD emission at 1.3μm [25]. Room temperature photoluminescence (PL) spectra for different DWELL samples are shown in Fig. 4.3. Emission spectra are normalised and plotted as a function of incorporated indium percentage.

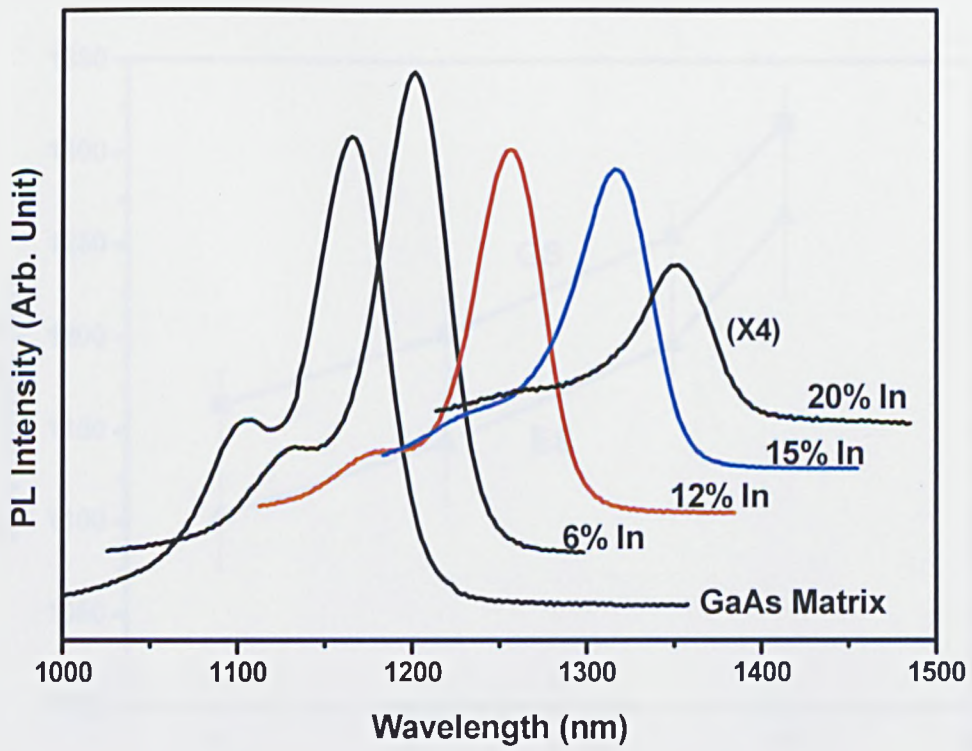

Fig. 4.3 Normalised PL spectra from different DWELL samples with different amount of indium incorporated in it

A gradual increase in ground state and excited state emission wavelength with increasing indium composition is observed. It is to be noted that the ground state emission wavelength for 15% and 12% In containing DWELLs are centred at 1.31μm and 1.26μm, respectively.

Figure 4.4 shows the results of line-fitting of the excited and ground state emission from the PL results of Figure 4.3. From this plot it is clearly observed that the ground state emission of the 12% In QW clearly overlaps the excited state emission of the 15% In QW. The error bars correspond to the full width at half maximum (FWHM) for each emission. The concept of our new device structure is derived from these intrinsic characteristics of the quantum dots, and relies upon a multi-layer DWELL

structure where the indium composition of each well is varied to vary the emission wavelength of the QDs. Inspection of Fig. 4.4 shows the excited state emission peak (~1.23μm) for the 15% DWELL almost overlaps with the ground state emission peak (~1.25μm) of the 12% DWELL. We utilise this overlap of the ground state emission from the 12 % In QW to the excited state emission from the 15% In QW at higher current regimes, to provide significant broadening of the emission.

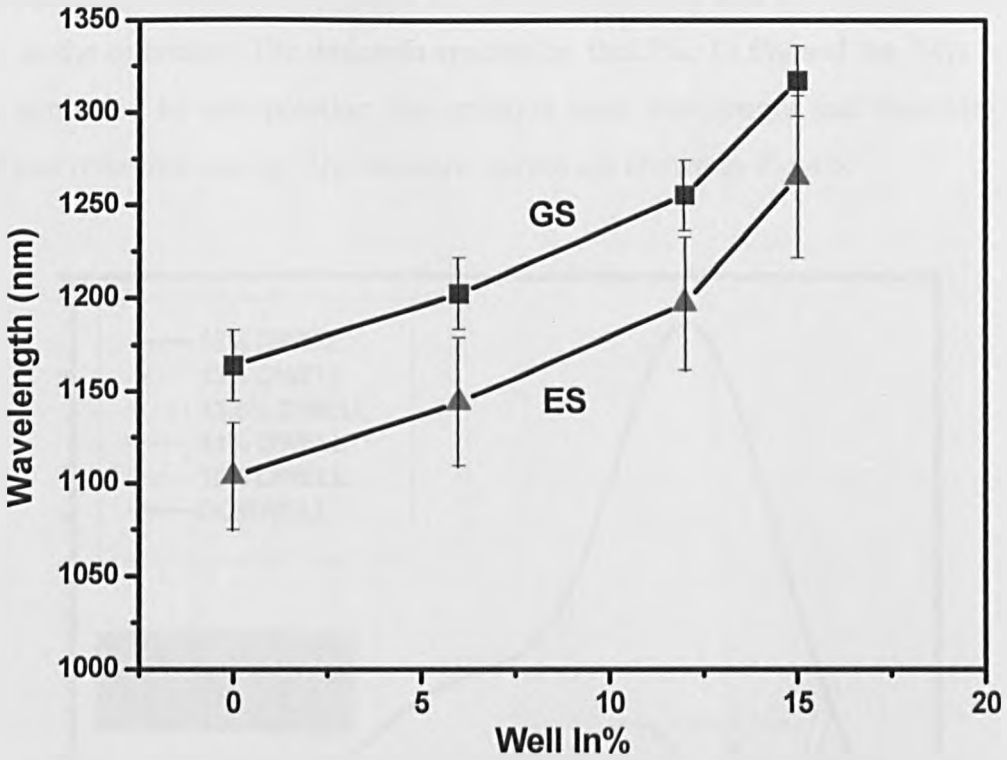

Fig. 4.4. Line fitting curve of the ground sate and excited state for the PL emission spectra of different DWELLs. The error bar corresponds to the FWHM of each emission.

For the new broad band SLED device the concept is to fill in the gap in between the GS and ES emission peaks of the 12% and 15% In well with other Gaussian emission peaks to obtain a broad emission spectra. Of further interest is the significant broadening of the excited state emission with increasing indium composition within the well. Our device design consists of 5 DWELL layers of 12%, 13%, 13.5%, 14%, and 15% indium respectively.

4.6 Modeling of Broadband SLED

4.6.1 Different In containing wells comparison of the EL spectra and the modeled data

Some basic modeling was performed so as to predict the nature and shape of the emission spectra of the proposed broadband superluminescent LED. The experimentally obtained PL spectra for the 12% In well and the 15% In well were taken as the reference. The emission spectra for the13%, 13.5% and the 14% In well were generated by interpolating the emission peak wavelength and linewidth from these two reference curves. The modeled curves are shown in Fig 4.5.

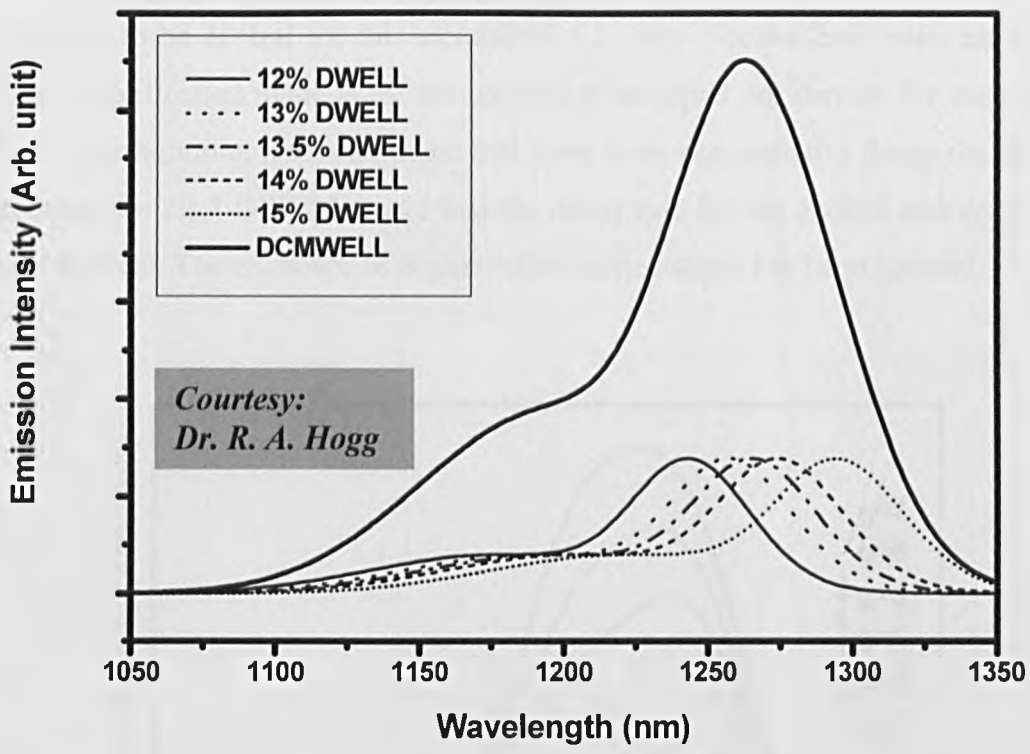

Fig. 4.5. Modeled emission spectra for DWELL structures with different amount of Indium incorporated in it. The large curve is the expected emission spectrum of a DCMWELL structure.

All the five different curves from each DWELL were plotted and the sum of all of them was generated to give the expected emission spectrum of a 5 DCMWELL structure. This model has a number of assumptions. The emission spectra from all the wells were assumed to be Gaussians. Also it was assumed that the FWHM and the peak emission wavelength for the modeled spectra maintain a linear relation ship with

the amount of In incorporated in the well. In this simulation the effect of the excited states were excluded. The FWHM for the resultant curve was ~80nm. The peak emission wavelength of the resultant spectra is equal to the emission peak for 13.5% In well.

4.6.2 Modelling of the electroluminescence spectra using the theory of random population of quantum dots.

Using the theory of random population of QDs proposed by Grundmann *et.al*, [29] the electroluminescence behaviour of this DCMWELL structure was modelled so as to determine the nature of state filling for the structure. The simulated emission spectra as a function of average dot occupancy, *g*, is shown in Fig. 4.6. All the dots were assumed to be neutral for this simulation, i.e. only electron-hole pairs are captured. One simplification made is the assumption of an equal dot density for each DWELL layer. Furthermore, it was assumed that there is no non-radiative decay (or that this is constant for all 5 DWELLs) and that the decay rate for the excited and ground states are identical. The existence of higher order excited states has been ignored.

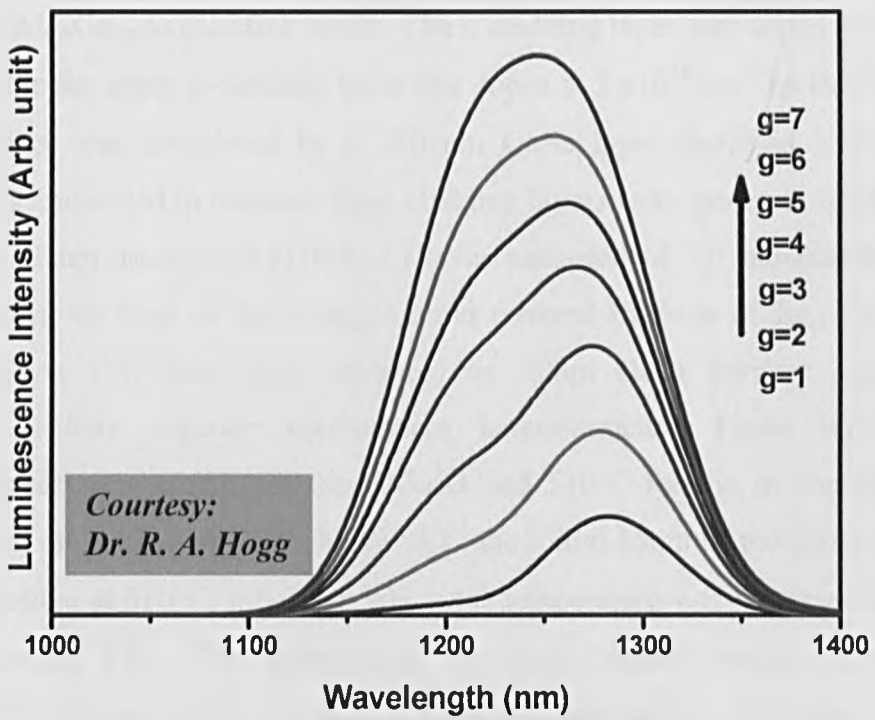

Fig. 4.6 Modeled unamplified electroluminescence spectra for different electron occupancies per dot

For g<6, there is no significant population of the second excited state, resulting in the second excited state transition being highly absorptive, rather than contributing gain to the system. Due to the edge emitting geometry of the device, it was therefore considered that the second excited state will not contribute significantly to the emission spectrum at the carrier densities used here. Absorption into the state can be expected to affect the short wavelength side of the modelled spectrum. For the modelled emission spectra, a blueshift of the emission peak is observed due to the overlap of the ground and excited states.

4.7 Growth and Initial results

The growth conditions of the Quantum Dot SLED structures were almost the same as those of the quantum dot lasers mentioned in the last chapter. Some of the growth conditions and growth parameters are mentioned in this section briefly for the ease of describing the changes made to grow the new DCMWELL structures.

A solid-source VG Semicon V90H molecular beam epitaxy system was used to grow the Quantum Dot SLED structures. The samples were grown on a Si doped GaAs (100) substrate by Dr Hui-Yun Liu. The optical confinement was achieved using 1500nm $Al_{0.4}Ga_{0.6}As$ cladding layers. The n cladding layer was doped at 5 $x10^{18}$ cm^{-3} by Si while the upper p-cladding layer was doped at 5 $x10^{18}$ cm^{-3} by Be. The upper p-doped layer was completed by a 300 nm GaAs layer doped at 1 $x10^{19}$ cm^{-3}. 5 DWELLs embedded in between these cladding layers were grown to form the desired structure. Each dot-in-well (DWELL) layer consisted of 3.0 monolayers (MLs) of InAs grown on 2nm of $In_{0.15}Ga_{0.85}As$ and covered by 6nm of $In_{0.15}Ga_{0.85}As$. Five InAs/InGaAs DWELLs were separated by 50nm GaAs barriers and embedded between 150nm separate confinement hetero-structure GaAs layers. Growth temperatures were 620°C for the AlGaAs and 510°C for the In containing layers. Following the deposition of each DWELL, the initial 15nm of the GaAs spacer layer was deposited at 510°C, following which the temperature was increased to 580°C for the remaining 35nm. The temperature was then decreased back to 510°C for the growth of the next DWELL. To reduce the detrimental effects associated with the low growth temperature we utilise two indium cells [25]. One cell is used to deposit the InAs QDs with low growth rate of ~0.092ML/sec, while the second cell is used to

deposit the InGaAs quantum well structure with a Ga growth rate of 0.8ML/sec. This flexibility in decoupling the well and QD epitaxy is key in achieving our new device design. For the DCMWELL samples, the five DWELLs of the structure contain 12%, 13%, 13.5%, 14% and 15% of indium respectively with the 12% In containing well on top of the stack. This change in indium composition was achieved by changing the temperature of the cell while the barrier layers were grown. Areal dot densities of $3.1x10^{10}$ cm^{-2} and $3.5x10^{10}$ cm^{-2} per layer were measured by atomic force microscopy on uncapped structures for indium compositions of 12% and 15%, respectively [25]. The cross sectional schematic of a DCMWELL structure is shown in Fig. 4.7.

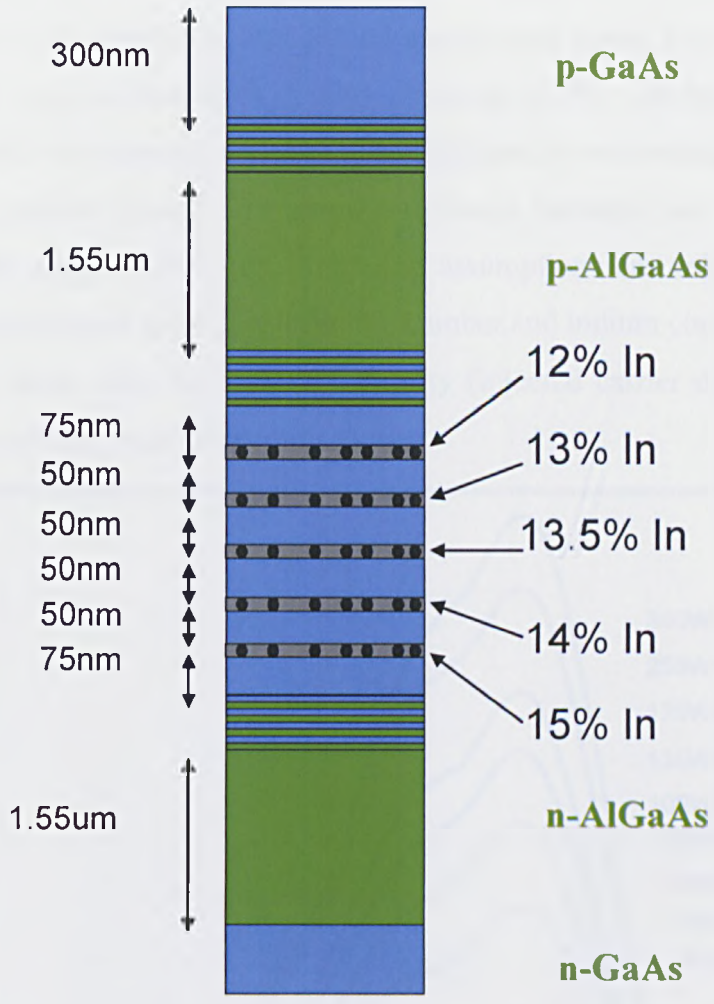

Fig. 4.7 Schematic diagram of the cross sectional view of the DCMWELL structure.

4.7.1 Room temperature Photoluminescence spectra of DCMWELL structure

The room temperature photoluminescence spectra as a function of excitation density for the DCMWELL structure are shown in Fig. 4.8. The excitation wavelength was 532nm, and the maximum excitation power density was limited by the maximum output power of the pump source. The upper cladding layer was etched off for PL measurements. Comparing the modelled emission spectra (Fig. 4.6) with experimentally obtained results a number of similarities are observed. There is good agreement between the state filling demonstrated in the photoluminescence spectra under low excitation density, and the simulated electroluminescence spectra for $g<6$ electrons per dot. For the modelled emission spectra, a blue shift of the emission peak is observed due to the overlap of the ground and excited states. For low excitation power densities, such a blue shift is also observed in PL. At higher excitation densities, a red shift is observed, which may be attributed to the heating of the sample due to higher incident power. The good agreement between our modelled and experimental data suggests that our model and assumptions are valid. In terms of tailoring our emission (and gain) spectrum, the number and indium composition of the DWELL layers, along with the excitation density (injected carrier density) may be varied to achieve a wide range of spectral shapes.

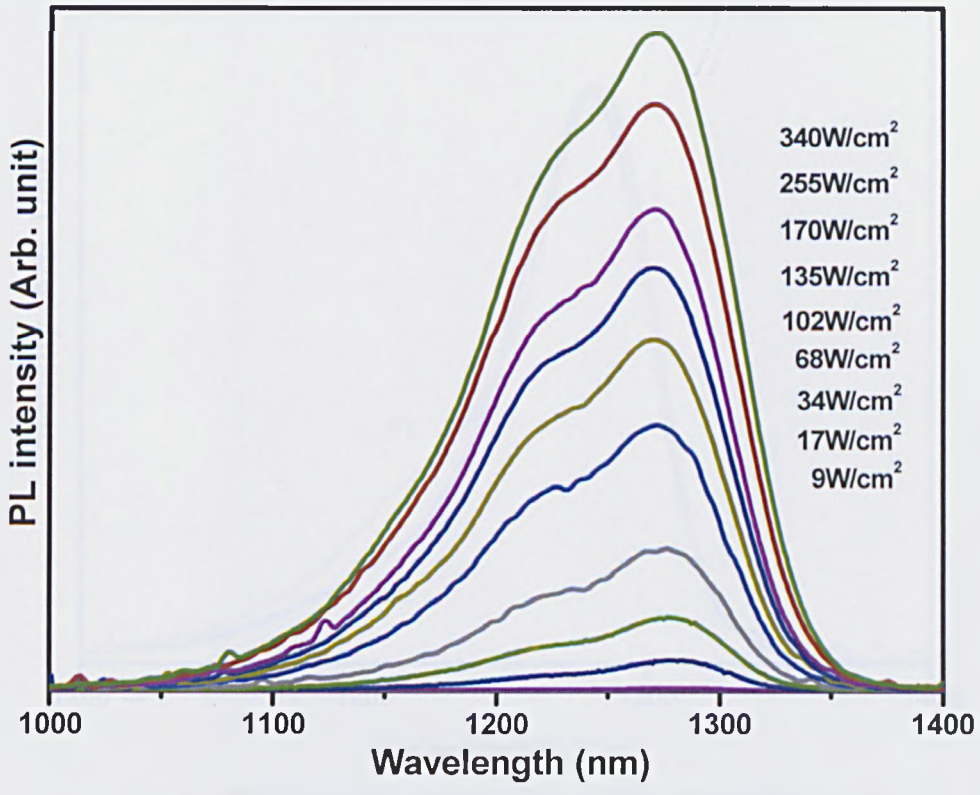

Fig. 4.8 Room temperature photoluminescence spectra of a DCMWELL sample as a function of incident power

4.7.2 Equal carrier distribution schematic and EL-PL comparison.

One possible problem with the control of the emission spectrum for our DCMWELL structure is the possibility of an uneven carrier distribution between DWELL layers of different indium composition, resulting in the emission being dominated by particular DWELL layers. We are able to confirm whether this is an issue or not by comparing the emission spectrum obtained by different excitation schemes. The room temperature PL spectrum and the EL spectrum of a sample with the top AlGaAs cladding layer removed are shown in Fig. 4.9. The PL spectrum was obtained at an excitation power density of 12.75W/cm^2 power using a 570nm laser while the EL spectrum is obtained at a current density of 22A/cm^2. These excitation powers and current densities were selected arbitrarily to obtain high ratios of GS to ES emission. The normalized spectra show almost identical ground state emission linewidth, strongly suggesting an even carrier distribution through out the DWELL layers at a low injection current. In addition to the different excitation mechanisms, the emission is collected in different geometries in the two experiments. As a consequence, we can expect different selection rules for the emission. However, we are able to compare the lineshape of the ground state emission at low excitation densities for these two excitation methods. For photo excitation a roughly even distribution of carriers can be expected throughout the active region. The similarity in the EL and the PL suggests there is also a roughly even carrier distribution by electrical injection.

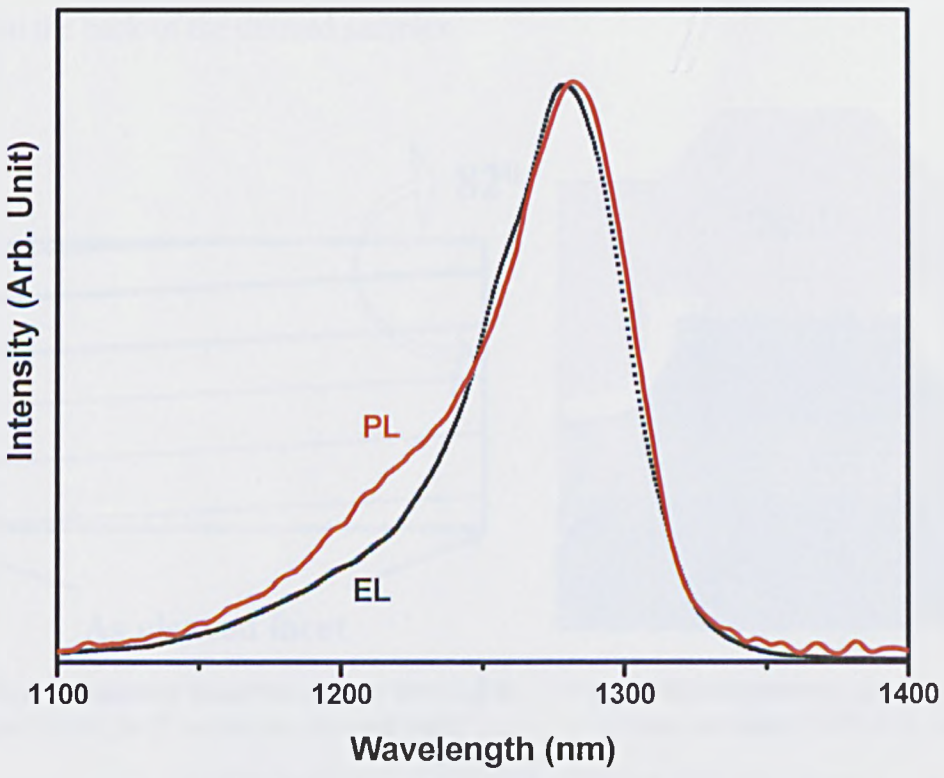

Fig. 4.9 Photoluminescence and electroluminescence spectra for a DCMWELL structure at low excitation density

4.8 SLED Fabrication

The SLED and laser structures studied here were fabricated in the same manner, as described in the previous chapter. The only difference being that the SLED ridges was tilted by 8^0 from the normal to the as-cleaved facet. In the previous chapter it was described and experimentally showed that the shallow ridge etch and selective electroplating of the ridges improves the overall characteristics of the DWELL lasers. For the SLED structures the same optimised fabrication technique was used. Both the DWELL and DCMWELL devices were formed with a shallow ridge etch after depositing Au-Zn-Au p-contact layer and annealing at 360^0C. Ridges were etched by wet chemical etching with the etching stopped at a depth of ~1.8μm after removing the upper GaAs and AlGaAs layer. For both types of device 500nm of SiN_x was deposited on the sample surface to minimise the leakage current flowing through the top AlGaAs layer. Contact windows were opened on the ridge top by reactive ion etching. Ti-Au bond pads were deposited and then the devices were selectively electroplated with ~3μm gold for the laser structures [27, 28] and ~1μm gold for the SLED structures. For the SLED structures it was observed that if the electroplated gold thickness is too thick (~3μm), some pieces of gold flaps cover the facet of the ridge after cleaving, due to the angled ridge structure it was impossible to ensure cleaving occurred through a non-gold-plated section of the device. We reduced the electroplated gold thickness to ~1μm for the SLED devices. InGe-Au n-contact was formed on the back of the thinned samples.

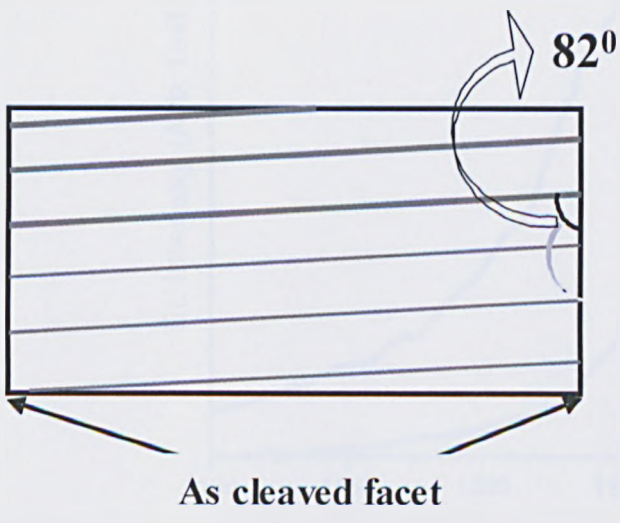

Fig. 4.10(a) Schematic diagram shows the SLED ridges tilted by 8^0 to the as cleaved facet

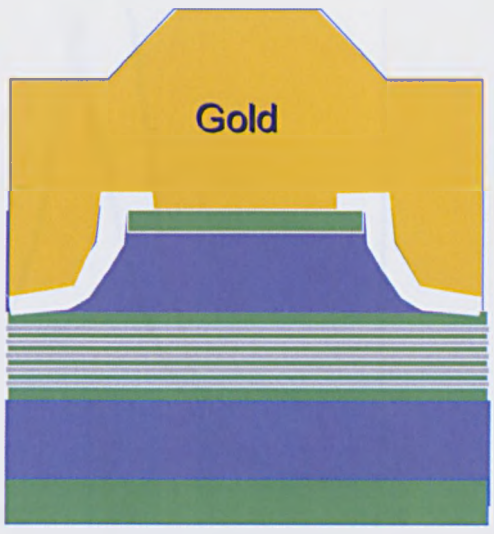

Fig. 4.10(b) Schematic diagram of the cross section of a SLED ridge

All the devices were mounted, and bonded on ceramic tiles. Both laser and SLED devices were cleaved into pieces of different lengths. The results obtained from all these devices are described and analysed in the following paragraphs. The schematic of the plan view of the SLED samples shown in Fig. 4.10(a) and the cross sectional view is shown in 4.10(b).

4.9 Results and discussion

4.9.1 Low current Electroluminescence spectra for DWELL and DCMWELL SLED

Figure 4.11 shows room temperature EL spectra of DWELL and DCMWELL SLED devices at a current density of 80 Acm^{-2}. This spectrum can be expected to correspond to unamplified spontaneous emission from the devices as the transparency current for such structures is ~50-100 Acm^{-2} and significant superluminescence was not observed below ~200 Acm^{-2}. Both the DWELL and DCMWELL SLED devices were 6mm long and 15μm wide. The emission spectra were normalised and a FWHM was obtained for the DWELL and DCMWELL of 44nm and 82nm, respectively. A clear broadening of the emission spectrum for the DCMWELL is observed compared to the DWELL. For the DCMWELL the emission peak is at 1266nm.

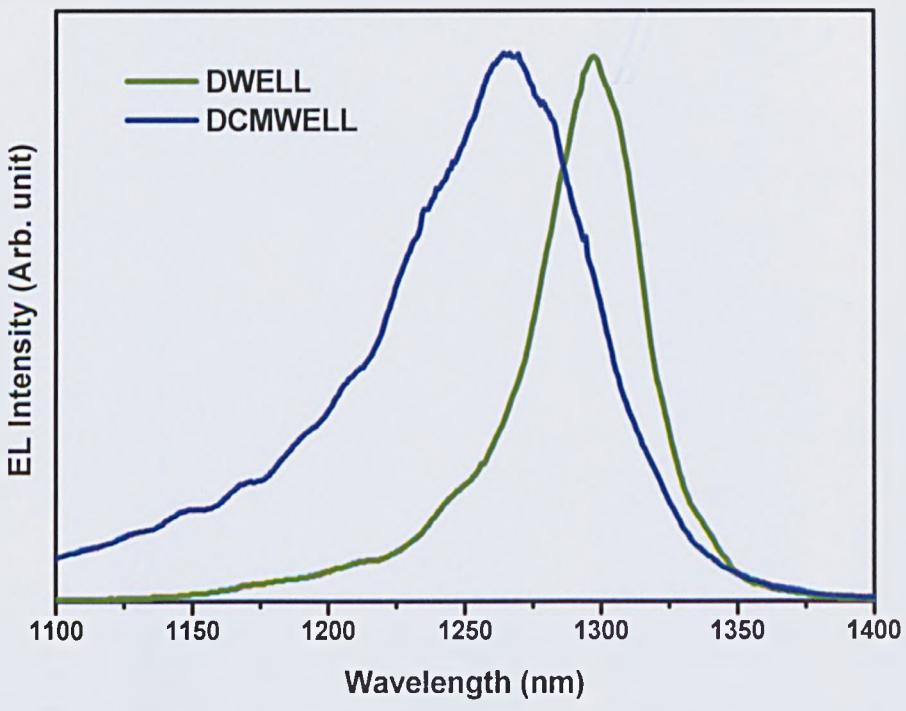

Fig. 4.11 Electroluminescence spectra of 6 mm long DWELL and DCMWELL SLED structures at a current density of 80A/cm^2

This shift in peak emission wavelength, compared to 1297nm for the DWELL device, corresponds to the expected interpolated emission wavelength centered around the ground state emission wavelength of the 13.5% DWELL layer. Both laser and superluminescent devices were fabricated from these two structures. The laser results are shown and discussed first and later in this chapter the SLED results are discussed.

4.9.2 Current-power characteristics and Electroluminescence spectra for DWELL and DCMWELL lasers

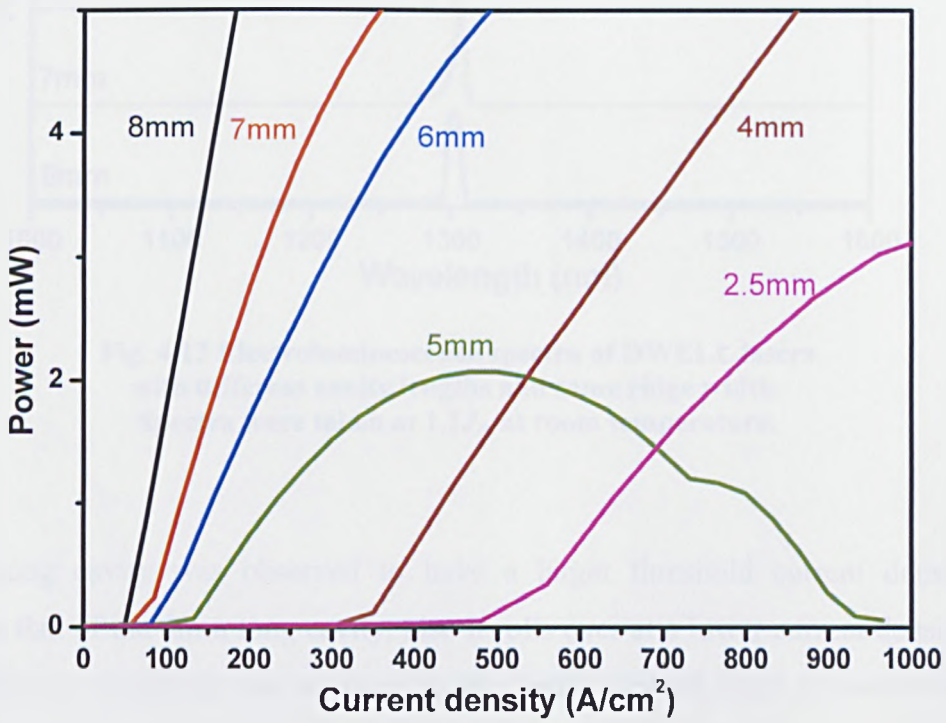

Fig. 4.12 CW Current-power characteristics for DWELL lasers with different cavity lengths and 5μm width

Current-power characteristics of the DWELL lasers of different lengths were taken at room temperature. The cavities were of different lengths and the ridge widths were 5μm. From Fig. 4.12 it is evident that the threshold current density is relatively independent up to 5mm long cavity. The current-power characteristic of the 5mm long cavity is observed to roll over after 400A/cm^2. This is most probably due to poor quality mounting of this particular device, resulting in inefficient heat extraction and early thermal roll-off. For the 4mm long and shorter cavities then threshold current density increases remarkably. This is suggestive that the 4mm cavity and the shorter cavities lase from the excited state as discussed and explained in the previous chapter.

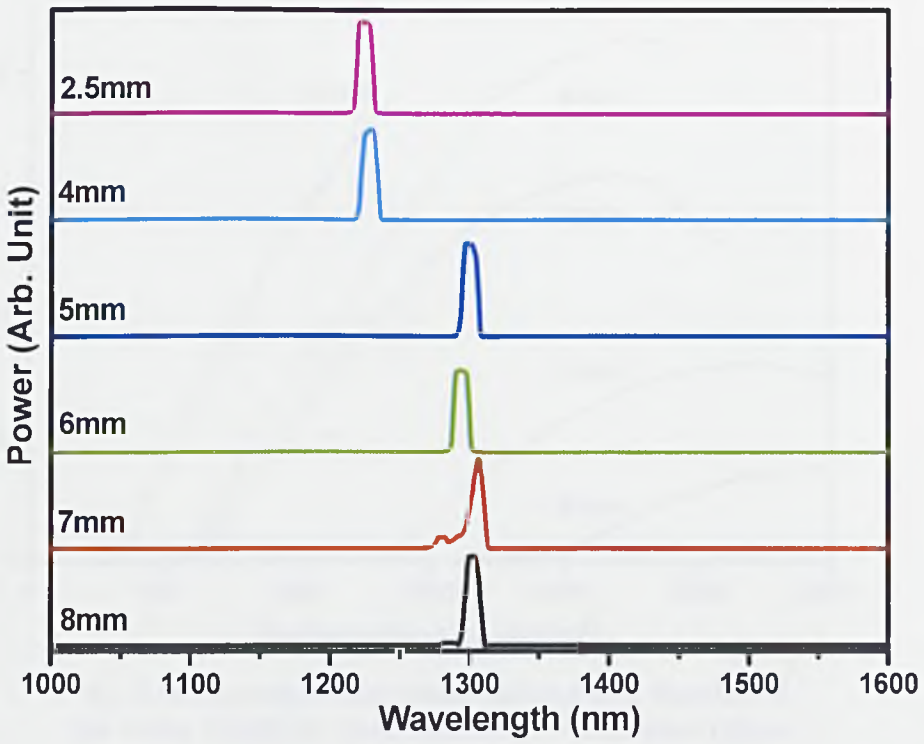

Fig. 4.13 Electroluminescence spectra of DWELL lasers with different cavity lengths and same ridge width. Spectra were taken at $1.1J_{th}$ at room temperature.

The 6mm long cavity was observed to have a larger threshold current density compared to that of the 5mm long cavity; also it rolls over at a lower current density. This behaviour is unnatural and attribute to the badly cleaved facet as mentioned earlier in the device fabrication section. This prediction was confirmed by taking the SEM image of the corresponding facet and some damage at one of the two facets was observed. The suspected switch in wavelength was supported by the electroluminescence spectra taken at room temperature at $1.1J_{th}$ of each cavity. The EL spectra in Fig. 4.13 clearly show that the cavities longer than 4mm emit from the ground state (~1300nm) and the 4mm cavity lases completely from the excited state (~1230nm). The 2.5mm long cavity also lases from the excited state.

The DCMWELL lasers were also characterized in a similar manner. The length dependent CW L-I characteristics for 5μm wide ridge taken at room temperature are shown in Fig. 4.14.

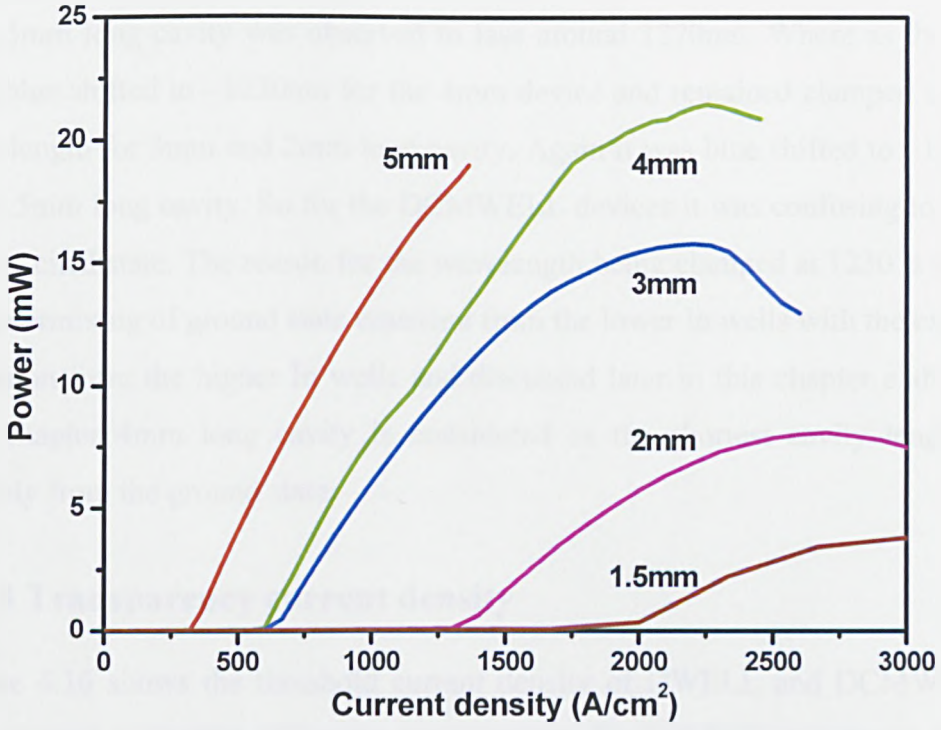

Fig. 4.14 Current density-power plotted as a function of the cavity length for 5μm wide DCMWELL laser ridges

It is clear from the curves that the threshold current densities for the 5mm, 4mm and 3mm long cavities are comparatively lower than that of 2mm long cavity. It seems that the cavities longer than 2mm lase from the ground state and the 2mm long and shorter cavities lase from the excited state. In order to investigate the lasing wavelength of the cavities of different lengths electroluminescence spectra of the devices were plotted. The electroluminescence spectra shown in Fig. 4.15 were taken at $1.1J_{th}$ of each cavity at room temperature.

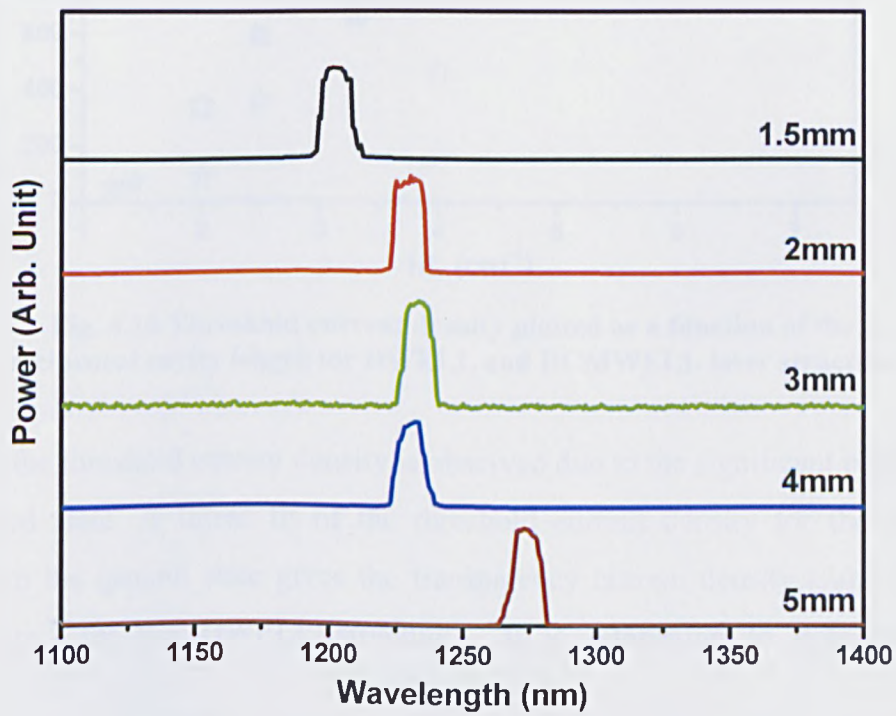

Fig. 4.15 Room temperature electroluminescence spectra for 5μm wide DCMWELL ridges of different lengths.

The 5mm long cavity was observed to lase around 1270nm. Where as the spectrum was blue shifted to ~1230nm for the 4mm device and remained clamped at the same wavelength for 3mm and 2mm long cavity. Again it was blue shifted to ~1200nm for the 1.5mm long cavity. So for the DCMWELL devices it was confusing to assign the first excited state. The reason for the wavelength being clamped at 1230 is attribute to the intermixing of ground state emission from the lower In wells with the excited state emission from the higher In wells and discussed later in this chapter elaborately. In this chapter 4mm long cavity is considered as the shortest cavity length to lase entirely from the ground state.

4.9.3 Transparency current density

Figure 4.16 shows the threshold current density of DWELL and DCMWELL laser structures as a function of inverse cavity length. The DWELL switches to the excited state for the cavity length shorter than 5mm.

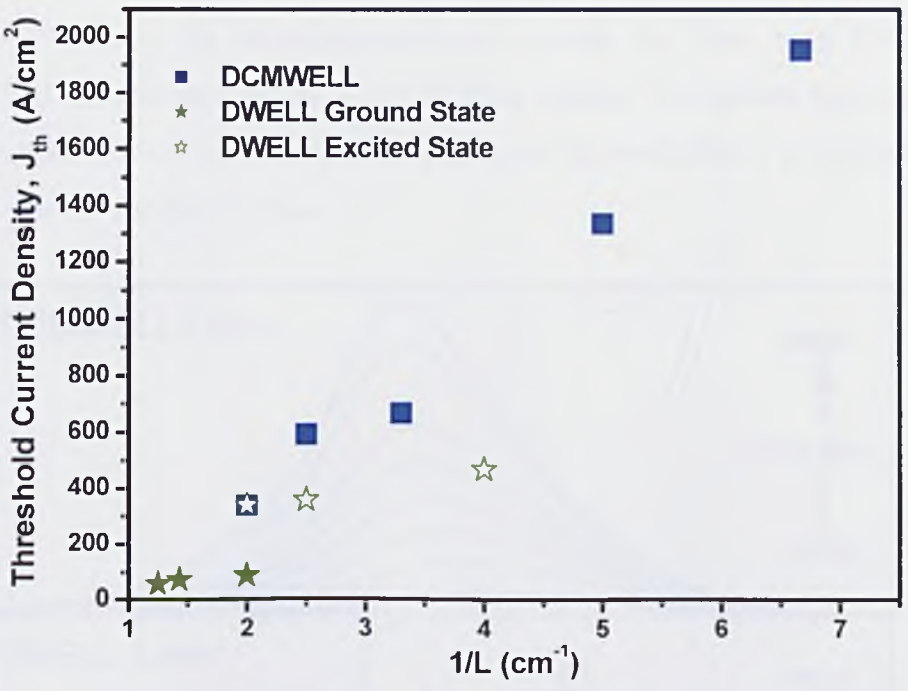

Fig. 4.16 Threshold current density plotted as a function of the reciprocal cavity length for DWELL and DCMWELL laser structure

A change in the threshold current density is observed due to the significant population in the excited state. A linear fit of the threshold current density for the devices emitting from the ground state gives the transparency current density (J_0). This is ~50-100 Acm^{-2} for the DWELL structure. It is interesting to note that the

extrapolation for infinitely long device gives almost identical transparency current density for both DWELL and DCMWELL lasers. If there were a non-thermal carrier distribution within the laser, this would be expected as there would be almost the same number of QDs taking part in lasing and transparency occurs when an average of 1 electron hole pair exists per QD [30]. Though the intercepts for the two set of data points at the y-axis give same values for the J_0, it is clearly observed that the gradient of the 1/L plot for the DCMWELL structure is larger than that of the DWELL lasers. This indicates a lower modal gain for the DCMWELL structure. In contrast, the Hakki-Paoli gain measurement (Fig. 4.19) gives very similar values of peak gain for both. This discrepancy is believed to be originated from the non-reproducibility of the cleaving of the DCMWELL devices.

4.9.4 Short cavity laser Electroluminescence comparison.

To observe the evolution of the emission spectrum with injection current for both types of devices, EL spectra of the short cavity laser structures were investigated. Figure 4.17 shows the electroluminescence spectra for 2mm long DWELL and DCMWELL devices as a function of CW drive current. The spectra were recorded at low injection currents (<200mA) so as to observe the evolution of ground and excited state occupancy for both devices.

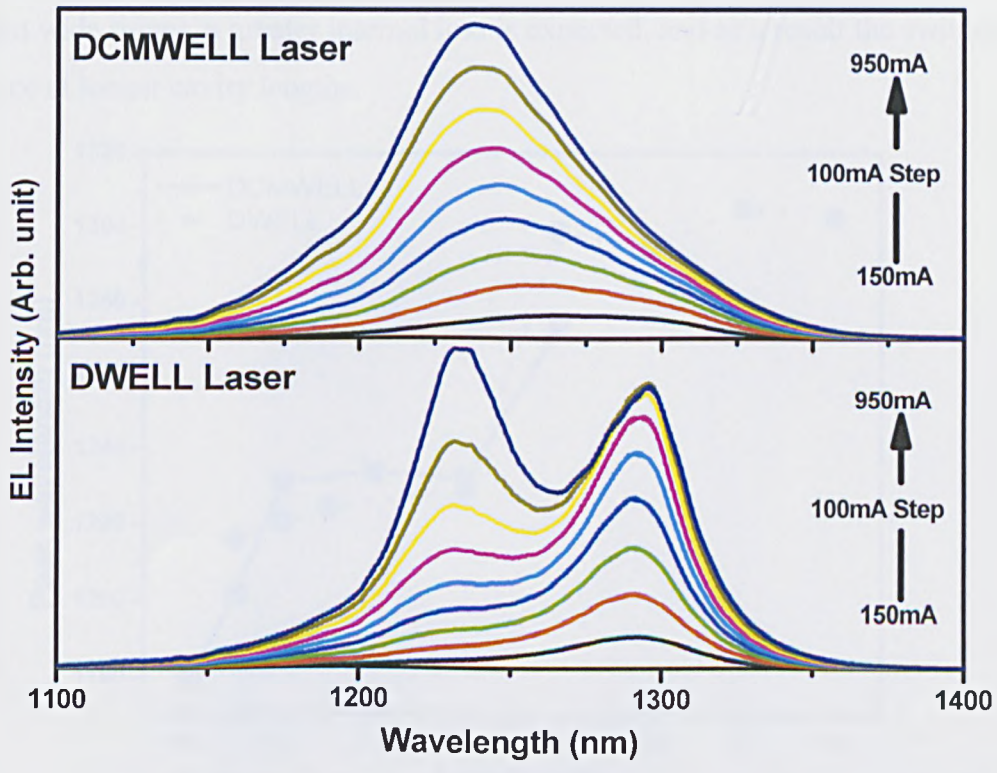

Fig. 4.17 Electroluminescence spectra for 2mm long, 5μm wide DWELL and DCMWELL laser cavities plotted as a function of CW drive current

Emission from the DWELL structure commenced via the ground state (1300nm) at low carrier density.With increased injected carrier density a saturation of the ground state was observed and also the excited state (~1230nm) was observed to build up. In contrast, initially the DCMWELL laser emits around 1270nm, which is the emission wavelength of a DWELL containing 13.5% In and no clear switching is observed for the emission spectra, rather a gradual blue shift was observed with increasing drive current. This is attributed to the gradual filling of the different DWELLs in the stack, and an overlapping of the ground and excited state emission of different DWELLs. This overlapping of states yields a single broad emission band from the DCMWELL, implying a broad single peak gain spectrum.

4.9.5 Peak emission wavelength for the cavities with different lengths

In order to investigate wavelength switching and the change in gain peak the lasing wavelength for cavities of different length was plotted. In Fig. 4.18 Peak wavelengths of the spectra at $1.1J_{th}$ for both the devices have been plotted as a function of the device lengths. A strong switch of the lasing wavelength was observed for the DWELL lasers of length 4mm [26] indicating shift from ground state (1300nm) to the excited state (1225nm). This switching is attributed to the saturation of the QD ground-state gain and incomplete gain clamping. Such switching was previously reported by me for 15μm wide ridges for cavity lengths of ~2-2.5mm [27]. For these 5μm wide ridges, a greater internal loss is expected, and as a result the switching takes place at longer cavity lengths.

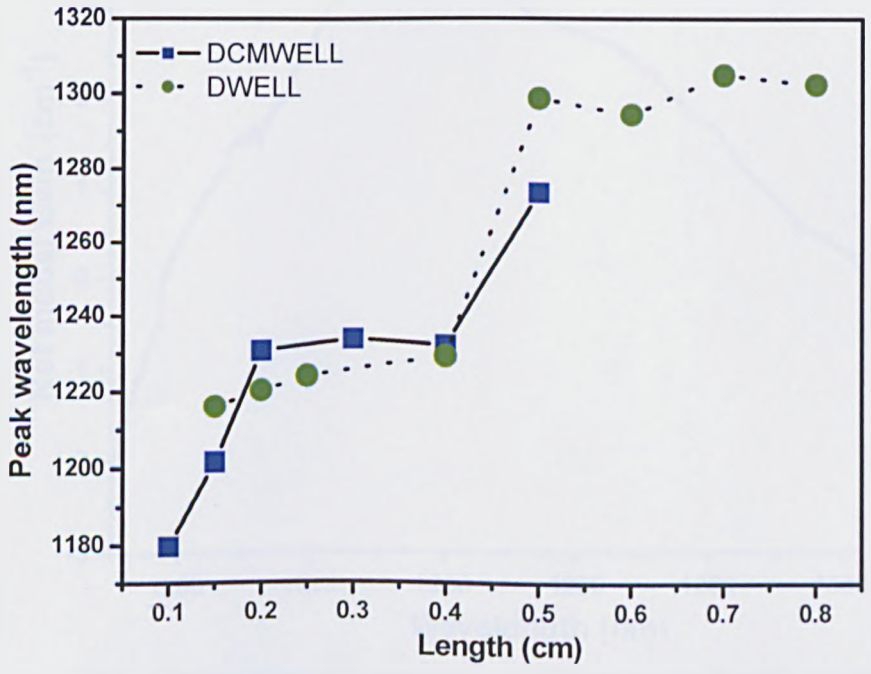

Fig. 4.18 Peak emission wavelength plotted as a function of cavity length for DWELL and DCMWELL laser devices of 5μm width

For the DCMWELL lasers the peak wavelength shifts continuously yet seems to be clamped around 1230nm for the devices shorter than 5mm and longer than 2mm. The probable reason for the lasing wavelength to be clamped at ~1230nm is the intermixing of excited state emission from the higher indium wells and the predominant ground state emission from the lower indium wells. This intermixing results in single peak broad electroluminescence spectra. Shorter emission wavelengths for cavities shorter than 2mm is most probably due to excited state emission from all the wells.

4.9.6 Gain spectra for DCMWELL lasers

Gain measurements for the DCMWELL lasers were performed using the Hakki-Paoli technique [31]. Figure 4.19 shows the gain spectra for a 2mm long DCMWELL laser at 0.9 J_{th} The figure demonstrates that the device exhibits gain over a bandwidth of 100nm with a peak wavelength of ~1230nm.

From the raw data the internal loss can be estimated as ~ 1-1.5 cm^{-1}, in good agreement with earlier work on DWELL lasers [27]. The occurrence of the peak gain around 1230nm is explained by the overlap of the ground state of the 12% DWELL and the first excited state of the 15% DWELL. In Fig. 4.19 it is observed that the peak gain for the DCMWELL laser is almost same as that of a DWELL laser though broadened (Fig. 2.10).

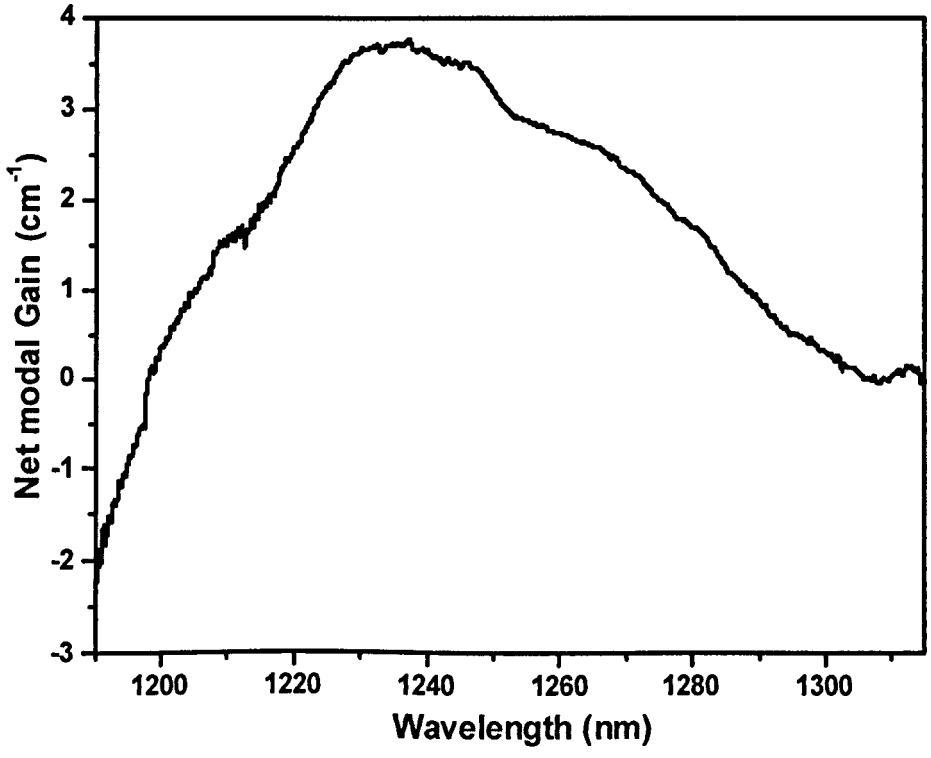

Fig. 4.19 Gain spectra for a 2mm long DCMWELL laser at 0.9 J_{th}

The reason for this high gain for the DCMWELL is attributed to the contribution of gain from the first excited state. As a result the peak emission wavelength of the DCMWELL laser is much less (~1230nm) than that of the DWELL laser (~1290nm).

4.9.7 Pulsed L-I curve for DWELL and DCMWELL SLED

Figure 4.20 shows the light-current density response measured from one facet of 6mm long DCMWELL and DWELL SLED devices. A pulsed current source with 1μs pulse width and 10 kHz repetition rate was used to minimise heating effects. Superluminescent behaviour is evidenced by the super linear increase in optical power with increasing current. The light - current behaviour is very similar for both DWELL and DCMWELL, but with the DWELL exhibiting slightly better performance. For the drive current >450Acm^{-2}, the superliner response of the SLED gives way to an almost linear response which is attributed to the non-linear gain-current relationship for QD actives. Slope efficiencies of 7.2% and 5.4% are obtained for the DWELL and DCMWELL devices are obtained, respectively. This difference in performance is attributed to a reduction in spectrally integrated gain for the DCMWELL structures, compared to the DWELL structure. Whilst the internal loss for structures such as these is of the order of 1-2 cm^{-1}, the saturated gain of the QD ground state is also low [27].

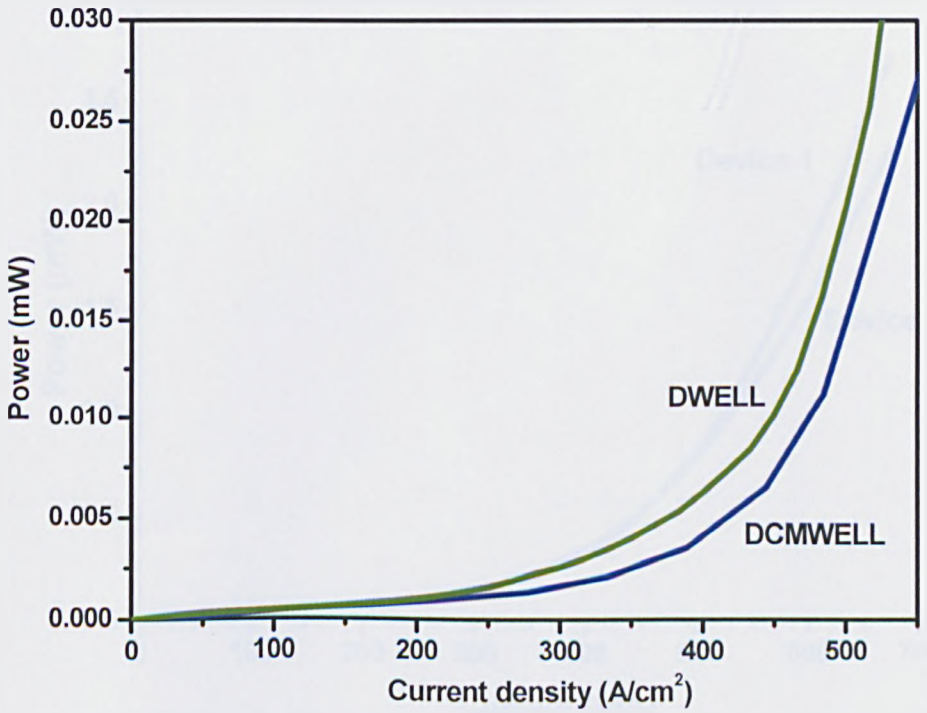

Fig. 4.20 Room temperature current density-power curve for DWELL and DCMWELL in the pulsed regime.

A concomitant broadening of the gain spectrum and reduction in peak gain for the DCMWELL structure, can therefore be expected to result in reduced optical power at a given drive current compared to the DWELL structure.

In addition, due to the smaller confinement energies of the DWELL layers with lower indium compositions, carrier confinement in the DWELL structure may be stronger than in the DCMWELL structure. If this is the case, we may therefore expect that for a given current density, the average dot occupancy of the DCMWELL structures will be lower than that of the DWELL structures

4.9.8 CW L-I curve for DCMELL

The CW room temperature (~24^{0}C) current-power characteristic for the 6mm long and 15μm wide DCMWELL devices is shown in Fig. 4.21. L-I characteristic of two different cavities from the same bar is shown here which have slight difference in output power. Maximum output power in excess of 2.5mW was obtained for one of these devices [31]. After 700mA the devices start to roll over and this is attributed to self-heating of the cavity at higher drive currents. Figure 4.22 plots the L-I characteristics for DWELL SLEDs under CW operation. The L-I characteristic curve for the DWELL SLED also starts rolling over after the same current.

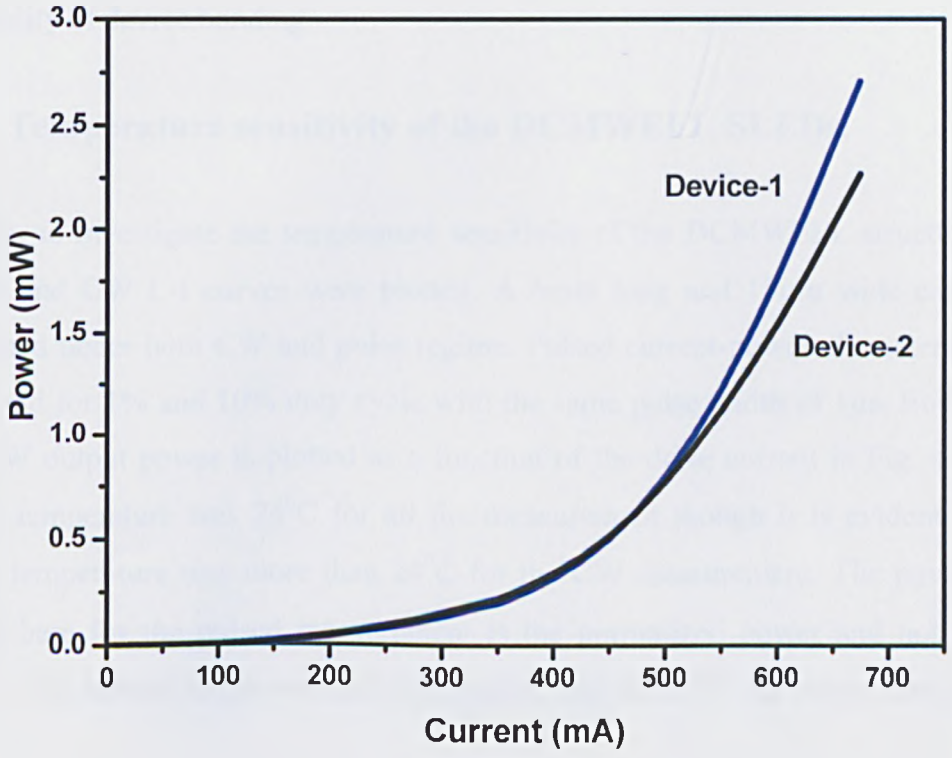

Fig. 4.21 Room temperature CW current-power characteristic curve for DCMWELL SLED

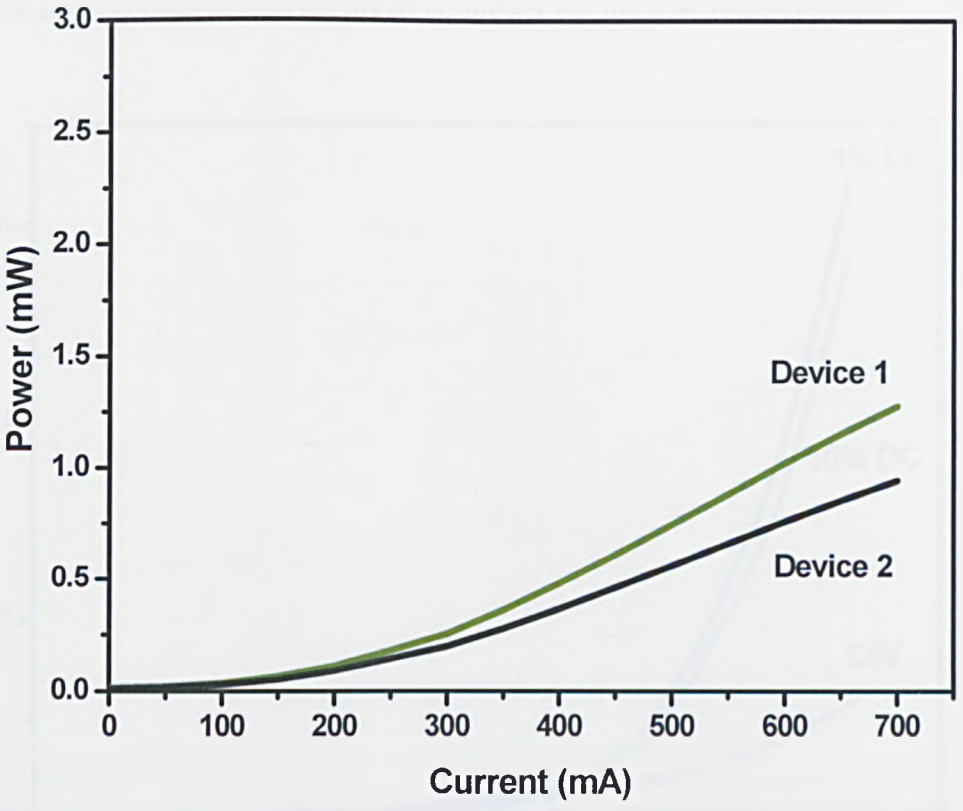

Fig. 4.22 Room temperature CW current-power characteristic curve for DWELL SLED.

The difference in CW response of these two devices is most likely due to differences in heat-sinking. This could be brought about by differences in substrate thickness or the quality of device bonding.

4.9.9 Temperature sensitivity of the DCMWELL SLEDs.

In order to investigate the temperature sensitivity of the DCMWELL structures both pulsed and CW L-I curves were plotted. A 6mm long and 15μm wide cavity was examined under both CW and pulse regime. Pulsed current-power characteristic was measured for 1% and 10% duty cycle with the same pulse width of 1μs. Both pulsed and CW output power is plotted as a function of the drive current in Fig. 4.23. The mount temperature was 24^0C for all the measurement though it is evident that the cavity temperature was more than 24^0C for the CW measurement. The power value shown here for the pulsed measurement is the normalized power and not the true power. The normalized power is always higher than the CW true output power for all

the drive currents >350mA, indicating strong self-heating effects within the device. Also, the turn on current also seems to be higher for the CW measurement.

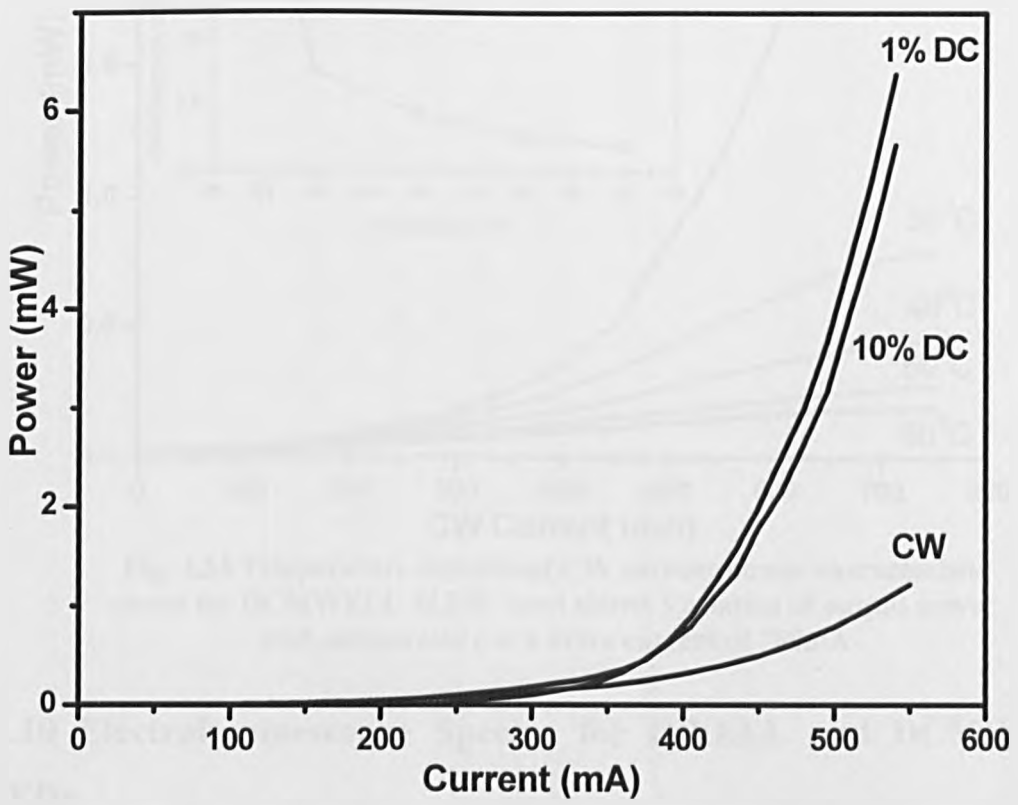

Fig. 4.23 Room temperature current-power characteristics for DCMWLL SLEDs in CW and pulsed regime for 1% and 10% duty cycles

The temperature dependent current power characteristic of the same device is shown in Fig. 4.24. The inset shows the output power at 700mA drive current as a function of the mount temperature. The plot shows a strong temperature dependence of the DCMWELL SLEDs with temperature. This behavior is attributed to the removal of thermally agitated carriers from the low indium containing wells and requires further improvement to increase the output power. In addition, non-radiative recombination rates may increase with increasing temperature. In chapter 5 of this thesis a method to increase the output power and bandwidth has been proposed and demonstrated. For those devices an improvement in the temperature characteristics was observed. These graphs allow an estimate of the self-heating induced by CW operation. At 500mA the output power is observed to reduce by ~75% when moving from 1% duty cycle to CW operation. Inspection of Fig. 4.24 indicates that this corresponds to an increase in cavity temperature of ~15 degrees.

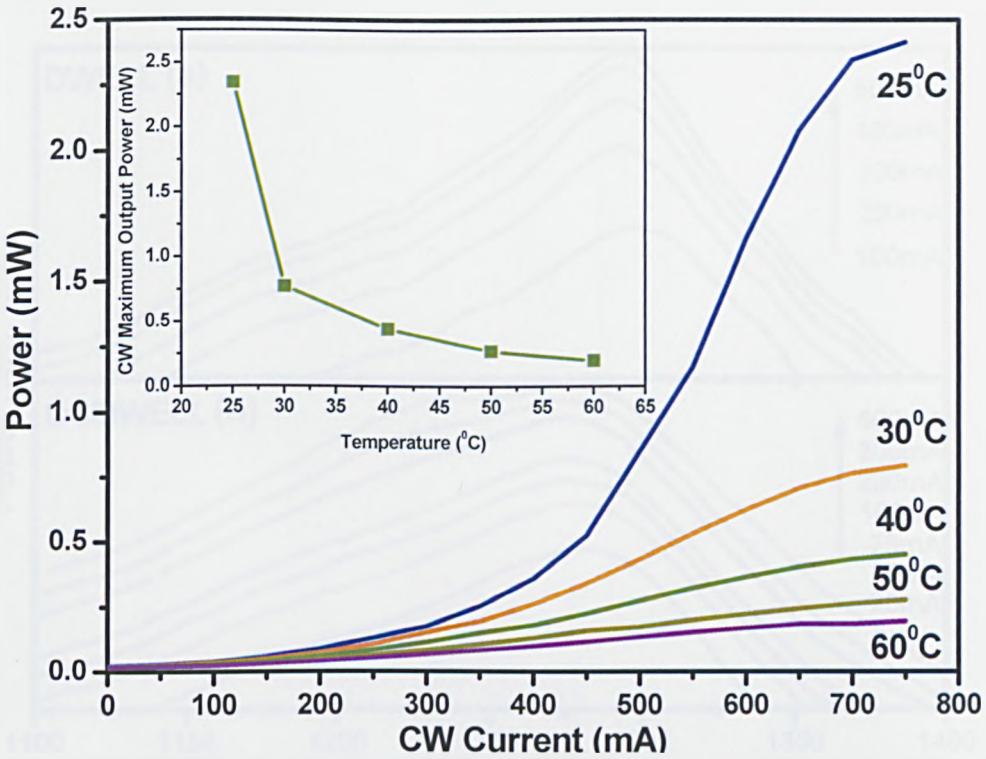

Fig. 4.24 Temperature dependant CW current-power characteristic curve for DCMWELL SLED. Inset shows Variation of output power with temperature at a drive current of 700mA

4.9.10 Electroluminescence Spectra for DWELL and DCMWELL SLEDs

Figure 4.25(a) shows the EL spectra of the 6mm DWELL device at room temperature as a function of drive current. The emission is dominated by the ground state of the quantum dots at 1.31μm. A narrowing of the emission linewidth is observed on increasing the drive current. Such a narrowing is the expected behaviour for a superluminescent LED where the spontaneous emission is convoluted with gain spectrum for the device.

Figure 4.25(b) shows the room temperature EL spectra for the DCMWELL device as a function of current. As noted previously, for low current densities, a larger linewidth than that of the DWELL device is observed. The peak wavelength at low currents is in good agreement with that predicted in Fig. 4.6. However, as the drive current is increased, the emission spectrum broadens and a slight blue shift was observed for the DCMWELL SLED [32] again in agreement with our model. This sharply contrasts the observed behaviour of the DWELL device for which the FWHM decreases with the increasing drive current.

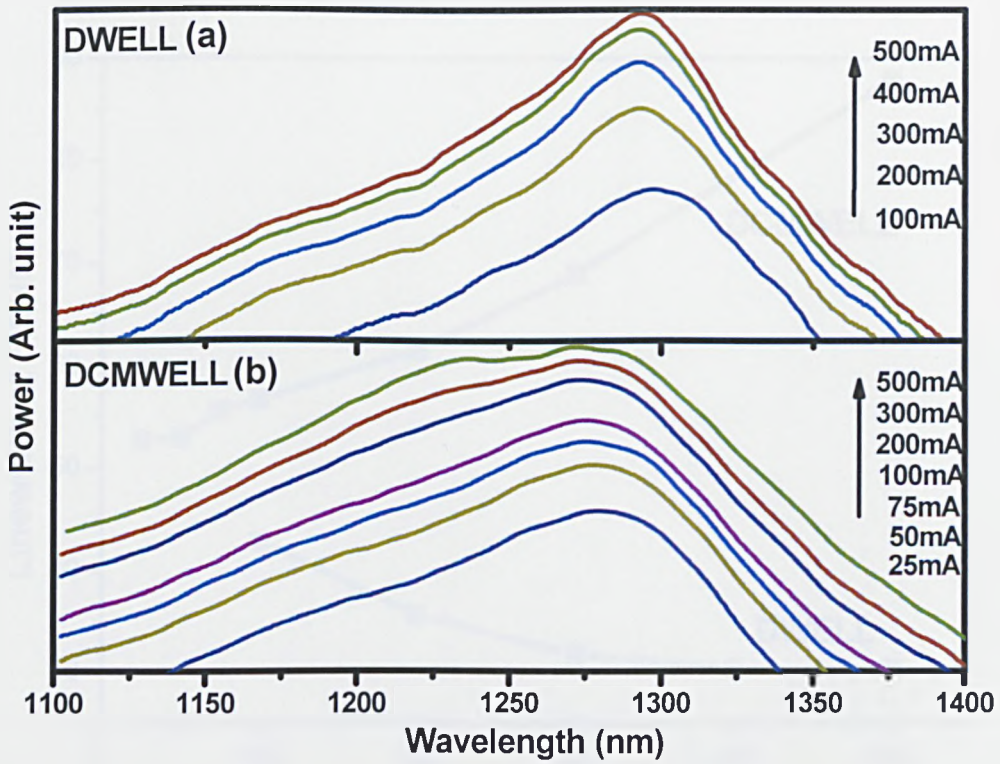

Fig. 4.25 Room temperature CW electroluminescence spectra for DWELL (a) and DCMWELL (b) SLED

From the figure it is clear that the spectra from the DCMWELL are broader than that of DWELL for all values of drive current. The DCMWELL spectrum at 500mA exhibits a small hump around 1230nm, which clearly indicates the onset of significant excited state population at this current and clearly overlaps with the ground state emission spectrum to give a broader emission. In contrast, at the same drive current the emission spectrum for the DWELL structure is single peaked and no existence of the excited state was observed. At a higher drive current the excited state for the DCMWELL becomes more prominent and at around 700mA of drive current the current-power characteristic starts rolling over.

The change in linewidth for the DWELL and DCMWELL as a function of CW drive current extracted from this data is shown in Fig. 4.26 and clearly demonstrates the broadening of emission for the DCMWELL structure, which is attributed to the appearance of excited state transitions.

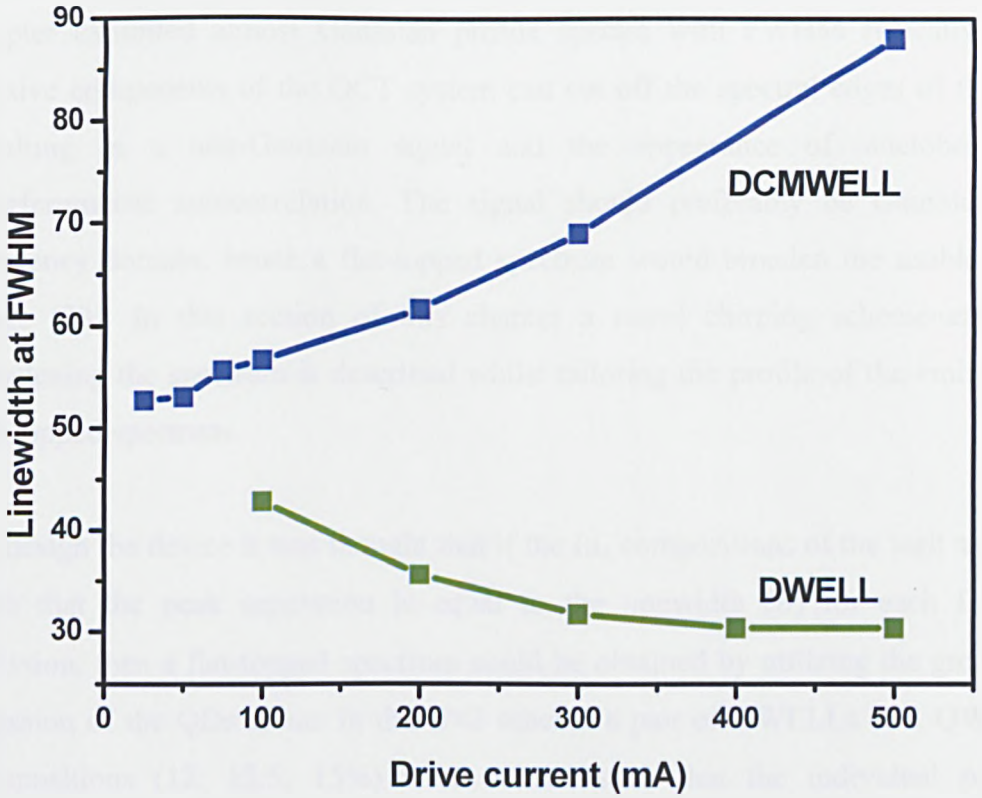

Fig. 4.26 Room temperature CW linewidth-current characteristic curve for DWELL and DCMWELL SLED

This occurs due to the broadening of the gain spectrum of the DCMWELL device, giving rise to a reduced stimulated emission rate for the ground state compared to the DWELL device. For a current density of 550Acm^{-2} a linewidth of >85nm is obtained, which is very close to that of the simulated spectrum we deduced [32]. This EL spectrum maintained an almost flat top. This spectral shape is quite different to the multi-gaussian spectra obtained for other broadband QD SLEDs [20] and is a result of the overlapping of excited and ground state transitions from different DWELLs within the structure, brought about by a careful choice of indium compositions for each DWELL in the DCMWELL device.

4.10 Further development of the DCMWELL structure

4.10.1 Concept for flat-topped emission

Another method of broadening the emission spectrum and to get a flat-topped emission from the QD SLED structure was based on the modification of the

DCMWELL concept. The DCMWELL described in the previous sections of this chapter exhibited almost Gaussian profile spectra with FWHM typically ~85nm. Passive components of the OCT system can cut off the spectral edges of the signal, resulting in a non-Gaussian signal and the appearance of sidelobes in the interferometric autocorrelation. The signal should preferably be Gaussian in the frequency domain; hence a flat-topped spectrum would broaden the usable spectral range [33]. In this section of this chapter a novel chirping scheme capable of broadening the spectrum is described whilst tailoring the profile of the emission to a flat-topped spectrum.

To design the device it was thought that if the In_x compositions of the well are chosen such that the peak separation is equal to the linewidth (σ) for each DWELL's emission, then a flat-topped spectrum could be obtained by utilizing the ground state emission of the QDs alone. In this 3×2 scheme a pair of DWELLs of 3 QW indium compositions (12, 13.5, 15%) were chosen such that the individual peaks are separated by their linewidth σ according to the schematic diagram in Fig. 4.27. For QDs with peak emission around 1250 to 1300nm σ was found to be ~38nm, hence the 3 different DWELL indium compositions were chosen to yield peak emissions separated by 38nm. This was achieved by interpolating from a plot of peak wavelength as a function of indium composition in the DWELL [25] to give indium compositions of 12, 13.5 and 15%. Additionally, 12 acceptors per dot p-type modulation doping were employed.

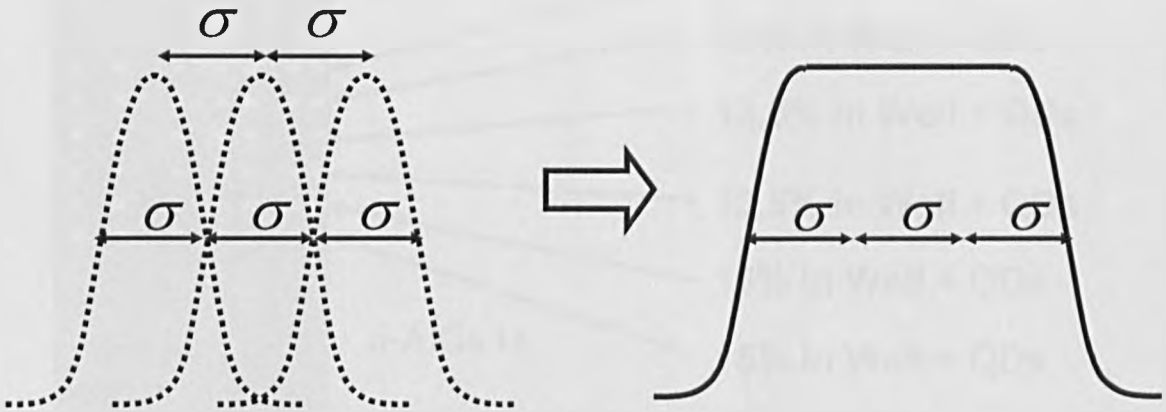

Fig. 4.27 The 3 × 2 arrangement, whereby the peak separation is equal to the linewidth, σ, for each DWELL, results in a flat-topped spectrum

4.10.2 Growth fabrication and device structure of the improved version of standard DCMWELL SLED

For the "standard" DCMWELL as demonstrated in ref [32] the five $In_xGa_{1-x}As$ wells contain x= 12%, 13%, 13.5%, 14% and 15% respectively, with the gain spectrum resulting from the 13, 13.5, and 14% DWELLs filling in the spectral range between the 12 and 15% DWELLs. This change in indium composition was achieved by changing the temperature of the cell while the barrier layers were grown. The new design provided here is a 6 DWELL structure and contains 2 DWELLs with 12% In, 2 DWELLs with 13.5% In and last two DWELLs contain 15% In. The DWELLS were arrayed in this order with the lowest In containing well closest to the p side of the structure. The schematic of the new structure is shown in Fig. 4.28.

One more structure with 6XDWELL was grown. Like the standard DWELL structure contained 15% In in all its 6 DWELLs (1X6 DWELL). The results of the 3X2 structure and the 1X6 structure were compared in the following sections. Like the previously mentioned SLED devices these SLEDs were also fabricated via a shallow ridge etch, with etching stopped after removal of the upper p-doped GaAs and AlGaAs layers at a depth of 1.8μm. 15μm wide ridges were mis-oriented by 8^0 to the facet normal

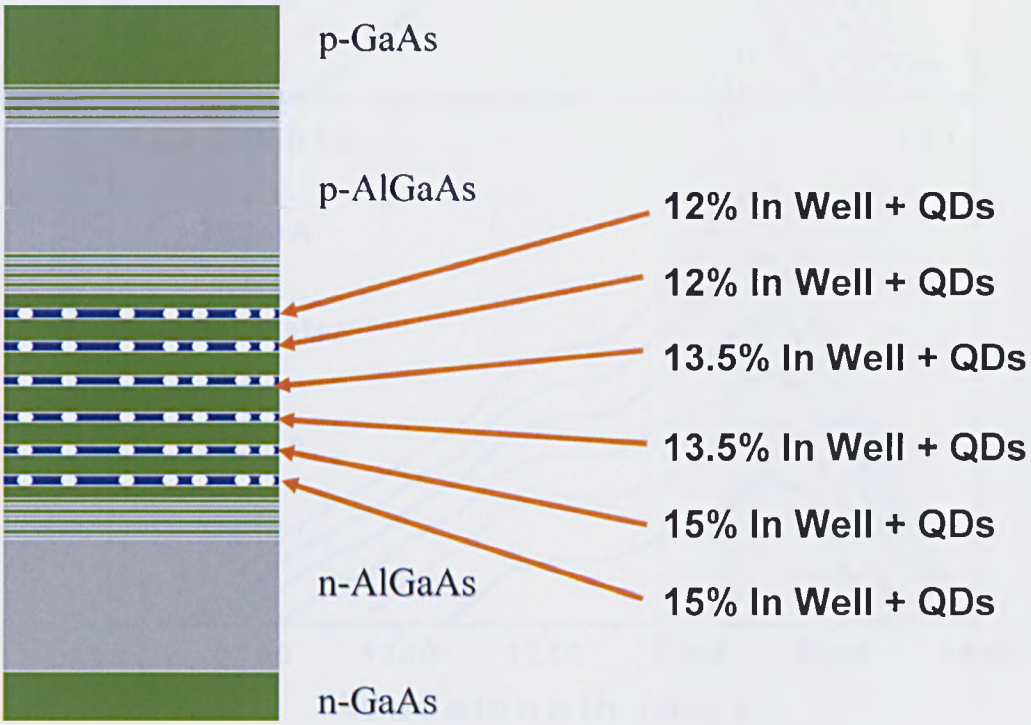

Fig. 4.28 Schematic device structure of the flat topped Superluminescent LED

Contact bondpads were electroplated with ~1.5μm of gold, and devices were of 6mm length, 15μm width, and were mounted on ceramic tiles, with no AR coating.

4.10.3 Result and discussion

4.10.3.1 Electroluminescence spectra

Room temperature electroluminescence spectra for the 3X2 DCMWELL and 1X6 DWELL structures, as a function of CW drive current are shown in Fig. 4.29 (a) and (b) respectively. The log of the EL intensity is plotted here as function of the wavelength. The drive current was varied form 100mA to 700mA in a step of 100mA. As mentioned previously, the SLED ridges are 6mm long and 15μm wide.

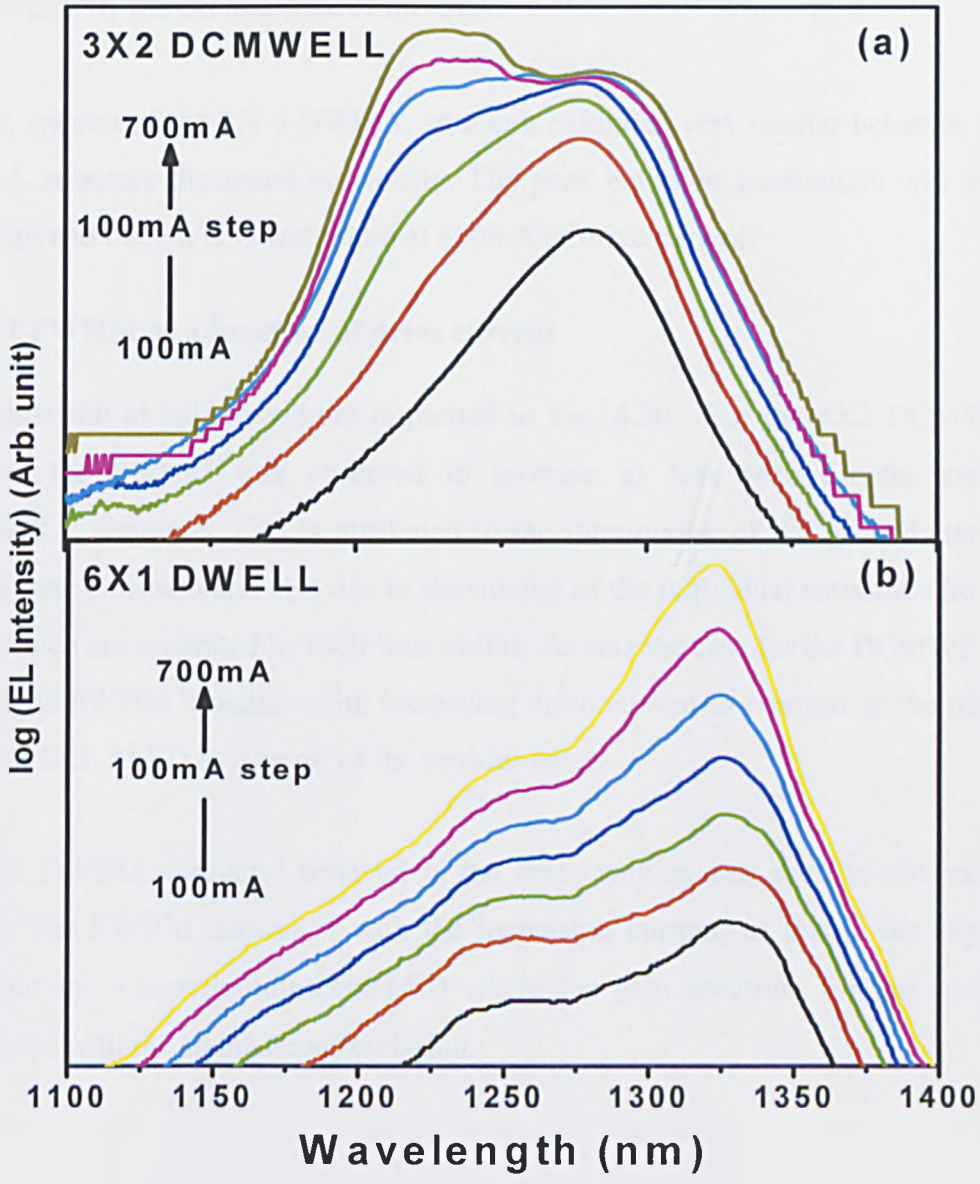

Fig. 4.29 Room temperature Electroluminescence spectra for a 3X2 DCMWELL and a 6X1 DWELL structure is plotted as function of drive current

The 3X2 structure was observed to emit between 1200nm and 1300nm. As the peak was observed to be flat topped no particular emission wavelength was assigned for this device. Collective "ground state" and "excited state" peaks, observed at lower and higher currents were ~1277nm and 1225nm respectively. At 600mA drive current the device exhibited a FWHM of ~95nm. After 600mA it was observed that the excited state starts dominating the emission spectra though no prominent excited state was observed and the spectrum remained single peaked. It must be noted that the flat topped emission spectrum is only obtained at one drive current. PL measurements for this structure also showed similar behavior. The RT PL for the 3X2 structure showed a FWHM of ~90nm with the ground state peak ~1271nm. The 95nm FWHM is consistent a theoretical 3σ prediction of 114nm, confirming the success of the design realisation. The narrower FWHM is possibly due to absorption of shorter wavelengths by the excited state of the QDs.

The EL spectra of the 1X 6 DWELL structure exhibited very similar behavior to the DWELL structure discussed previously. The peak emission wavelength was around ~1325nm and the FWHM was 30nm at 600mA of drive current.

4.10.3.2 FWHM as a function of drive current

The full width at half maximum is plotted in Fig. 4.30. For the 3X2 DCMWELL structure the FWHM was observed to increase as was seen for the standard DCMWELL structure. This is attributed to the intermixing of the ground state and excited state emission and also due to the mixing of the individual emissions from the wells, which are separated by their line widths. As was the case for the DCMWELL in ref [8], the FWHM broadens with increasing drive current in contrast to the narrow-band DWELL SLED as a result of the broader gain.

The 6x1 DWELL structure behaved in the same way as was seen in the previous section. The FWHM decreased with the increasing current, as this is the expected behaviour for a superluminescent LED where the gain spectrum for the device is convoluted with the spontaneous emission.

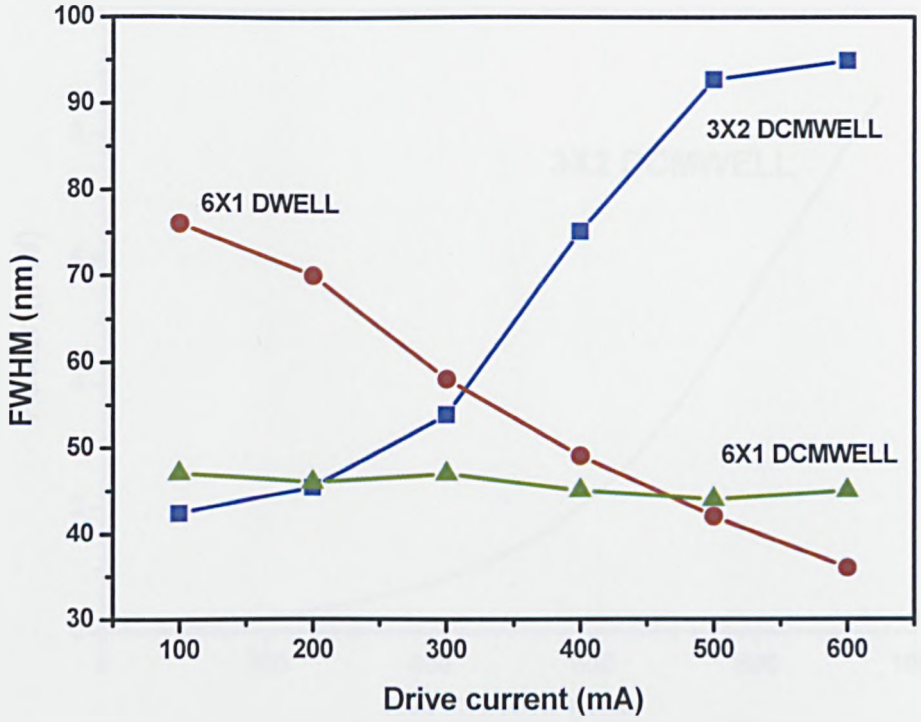

Fig. 4.30 FWHMs for three samples are plotted as a function of drive current.

Surprisingly the FWHM 6X1 DCMWELL structure remained almost same through out the current range. The reason for this behaviour was unknown and was predicted to be the effect of the p-type modulation doping at the active region.

4.10.3.3 Current-power characteristics

The CW current power characteristic for the 3X2 structure is shown in Fig.4.31 The device dimension was 6mmX15μm and operated without any active cooling. CW output power of more than 8mW was recorded from this device at ~950mA drive current. This high output power is attributed to the combined effect of p-type modulation doping and for having more wells in the active region compared to the standard DCMWELL structure.

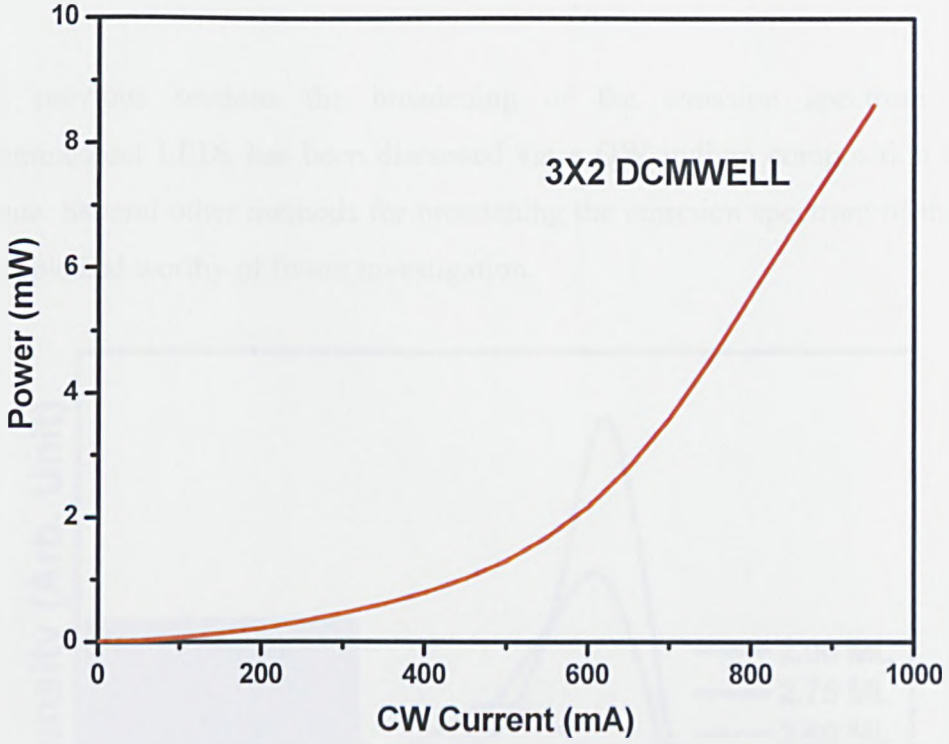

Fig. 4.31 Current power characteristic of an 6mmX15μm 3X2 DCMWELL structure at room temperature

4.11 Conclusion

In this chapter the design, fabrication and operating characteristics of QD SLED devices, which utilise an active region comprising DWELL layers with different indium composition has been discussed. Through the use of 5 DWELL layers with different QW indium compositions, a superluminescent LED operating CW at room temperature with peak wavelength of 1.27μm, FWHM of 85nm, and 2.5mW output power, and 100nm wide gain spectrum has been realised. The characteristics of both laser and SLED devices fabricated from this material have been discussed. Key to this design is the overlapping of the ground and excited state emission of different DWELL layers, resulting in an almost flat-topped emission spectrum. Further development of the DCMWELL structure resulted in ~95nm broad flat topped emission spectrum and more than 8mW of CW output power was achieved at room temperature. This structure was based on the same principle by overlapping the ground states of different In containing wells. Emphasis was placed on broadening the bandwidth of the quantum dot SLED structures but these devices were not capable of emitting high output powers. In the next chapter a method is proposed and exhibited the method of enhancing the output power of the quantum dot SLED devices.

4.12 Further work

In the previous sections the broadening of the emission spectrum of QD superluminescent LEDs has been discussed via a QW indium composition chirping technique. Several other methods for broadening the emission spectrum of the SLED are possible and worthy of future investigation.

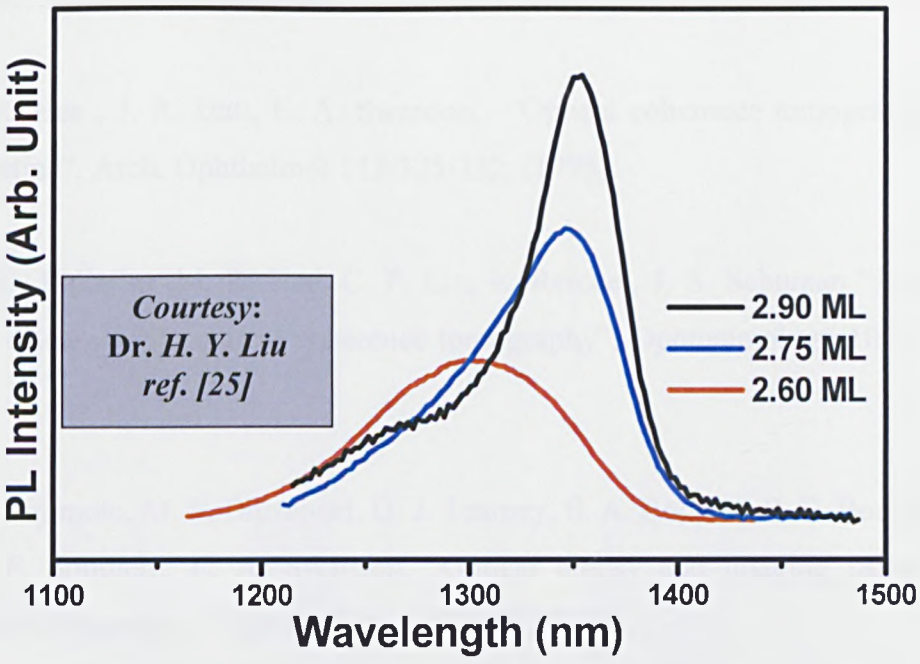

Fig. 4.32 Room temperature Photoluminescence spectra from three different samples with different InAs deposition rate

It has been observed that if the InAs deposition thickness is reduced there is a significant broadening of the emission spectrum [25]. Figure 4.32 shows the room temperature PL spectrum from three different uncapped samples with different InAs thickness. A broad emission peak at ~1300nm with a FWHM of 15.5nm was observed for the sample with 2.60ML of InAs. Increasing the InAs thickness to 2.75ML resulted in a narrower emission peak. The sample with 2.90ML InAs shows the narrowest linewidth while all three samples show roughly similar integrated intensities. This behavior represents the transition from emission dominated by smaller dots to the emission dominated by the larger dots due to the increased amount of InAs. QD SLEDs utilizing such 'immature' quantum dots would be an interesting route to broadband emission.

References

[1] J.M. Schmitt "Optical Coherence Tomography (OCT): A review" IEEE J. Sel. Top. Quantum. Electron. 5(4), 1205-1215, (1999).

[2] W. Drexler "Ultrahigh-resolution optical coherence tomography". J. Biomed. Opt. Vol. 9 no.1, 47-74 (Jan-Feb 2004).

[3] M. R. Hee , J. A. Izatt, E. A. Swanson, "Optical coherence tomography of the human retina". Arch. Ophthalmol 113:325-332, (1995).

[4] C. A. Puliafito ,M. R. Hee, C. P. Lin, E. Reichel, J. S. Schuman "Imaging of macular diseases with optical coherence tomography". Ophthalmology 102:217-229, (1995).

[5] J. G. Fujimoto, M. E. Brezenski, G. J. Tearney, S. A. Boppart, B. E. Bouma, M. R. Hee, J. F. Southern, E. A. Swanson, "Optical biopsy and imaging using optical coherence tomography," Nature Med., 1, 970-972 (1995).

[6] B. E. Bouma, L.E. Nelso, G. J. Tearney, D. J. Jones, M. E. Brezenski, J. G. Fujimoto, "Optical coherence tomographic imageing of human tissue at 1.55μm and 1.81μm using Er- and Tm-doped fibre sources," J. Biomed Opt. 3, 76-79 (1998).

[7] S. R. Chinn, E. A. Swanson, "Blindness limitation in optical coherence domain reflectrometry", Electron lett. 294, 2025-2027, (1993)

[8] T. P. Lee, C. A. Burrus, B. I. Miller. "A stripe geometry double heterostructure amplified-spontaneous emission (Superluminescent) Diode." IEEE Jrnl. of Quantum Electron. QE-9, 820, (1973).

[9] L. Burrow, F. Causa, J. Sarma, "1.3W Ripple free Superluminescent Diode" IEEE Photon. Technol. Lett. 17, 10, (2035-2037), (2005).

[10] T. R. Cheng, Y. H. Eng, A. Yariv, N. S. Kwong, P. C. Chen, Appl. Phys. Lett. 56 1345 (1990).

[11] S. Kondo, H. Yasaka, Y. noguchi, K. Magari, M. Sugo, O. Mikami, Electron. Lett. 28, 132, (1992).

[12] A. T. Semenov, V. R. Shidlovski, S. A. Safin, Electron. Lett. 29, 854, (1993).

[13] A. T. Semenov, V. R. Shidlovski, D. A. Jackson,, R. Willsch, W. Ecke. Electron. Lett 32,255, (1996)].

[14] C. -F. Lin, B. -L. Lee, P.-C. Lin "Broad-band superluminescent diodes fabricated on a substrate with asymmetric dual quantum wells." IEEE Photonics. Technol. Lett. 8, 1456, 1996.

[15] B. R. Wu, C. F. Lin, L. W. Laih, T. T. Shih, "Extremely broadband InGaAsP/InP supeluminescent diodes", Electron. Lett., 36, 2093-2095, (2000)

[16] D. Bimberg, M. Grundmann, F. Heinrichsdorff, N. N. Ledentsov, V. M. Ustinov, A. E. Zhokov, A. R. Kovsh, M. V. Maximov, Y. M. Shernyakov, B. V.Volvik, A. F. Tsatsulnikov, P. S. Kop'ev, Zh. I. Alferov. "Quantum dot lasers: breakthrough in optoelectronics", Thin Solid Films, 367, 235-249, (2000).

[17] Z.-Z. Sun, D. Ding, Q. Gong, W. Zhou, B Xu, Z.-G. Wang. "Quantum-dot superluminescent diode: A proposal for an ultra-wide output spectrum" Optical and Quantum Electron. 31, 1235-1246, (1999).

[18] D.C. Heo, J.D. Song, W.J. Choi, J.I. Lee, J.C. Jung, I. K. Han "High power broadband InGaAs/GaAs quantum dot superluminescent diodes" Electron. Lett. 39 (11), (2003).

[19] Z.Y. Zhang, Z.G. Wang, X.P. Jin, Z. Z. Sun, F.Q. Liu "High performance QuantumdotSuperluminescent Diodes" IEEE Photonics. Technol. Lett. 16, (1), 27-29, (2004).

[20] M. Rosseti, A. Markus, A. Fiore, L. Occhi, C. Velez. "Quantum dot superluminescentdiodes emitting at 1.3 um " IEEE Photonics. Technol.. Lett. Vol. 17, No. 3, 540-542 (2005).

[21] G. Du, C. Xu, Y. Zhao, H. Wang. " High-power broad-band superluminescent light source" IEEE J. Quantum. Electron. vol 39, no.1 (Jan 2003).

[22] IL Ki Han, Du Chang Heo, Jin Dong Song, IL Lee and Joo In Lee. "Study of Superluminescent Diodes Using InGaAs-InAs Chirped Quantum Dots" J. Korean Physical Society Vol. 45, No. 5, 1193-1195, (Nov 2004).

[23] L. H. Lee, M. Rossetti, A. Fiore, L. Occhi and C. Velez. "Wide emission spectrum from superluminescent diodes with chirped quantum dot multilayers" Electron. Lett., Vol.41 No. 1 41-43, (Jan 2005).

[24] H.Y. Liu, I.R. Sellers, D.J. Mowbray, M.S. Skolnick, K.M. Groom, M. Gutierrez, M. Hopkinson, J.S.Ng, J.P.R. David, R. Beanland. "Improved performance of 1.3μm multilayer InAs quantum-dot lasers using a high-growth-temperature GaAs spacer layer" Appl. Phys. Lett. 85(5), 704-706, (2004).

[25] H.Y. Liu, M. Hopkinson, C.N. Harrison, M.J. Steer, R. Frith, I.R. Sellers, D.J. Mowbray, M.S. Skolnick "Optimizing the growth of 1.3 um InAs/GaAs dots-in-well structure" J. Appl. Phys. 93 (5), 2931, (2003).

[26] H.Y. Liu, D.T. Childs, T.J. Badcock, I.R. Sellers, M. Hopkinson, R.A. Hogg, D.J. Robbins, D.J. Moqbray, M.S. Skolnick "High-performance three layer 1.3 um InAs-GaAs Quantum-dot lasers with very low continuous-wave room-temperature threshold currents IEEE Photonics. Technol.. Lett. 17(6), 1139-1140, (2005).

[27] S. K. Ray, K. M. Groom, R. A. Hogg, H. Y. Liu, M. Hopkinson, T. J. Badcock, D. J. Mowbray, M. S. Skolnick. "Improved Temperature Performance of 1.31μm Quantum Dot Lasers by Optimised Ridge Wavelength Design". IEEE Photonics. Technol.. Lett. Vol. 17, No. 9, September 2005.

[28] S. K. Ray, K. M. Groom, R. A. Hogg, H.Y. Liu, I R. Sellers, M. Hopkinson, T. J. Badcock, A. J. Ramsay, D. J. Mowbray, M. S. Skolnick. "Growth, Fabrication, and Operating Characteristics of Ultra-Low Threshold Current Density 1.3 um Quantum Dot Lasers". Jpn, J. Appl. Phys. 44 (4B), 2520-2522, (2005).

[29] M. Grundmann and D. Bimberg. "Theory of random population for quantum dots" Phys. Rev. B, 55 (15) 9740-9745 (1997).

[30] S. K. Ray, K. M.Groom, R. Alexander, K. Kennedy H.Y. Liu, M. Hopkinson, R. A. Hogg. "Design, Growth, Fabrication and Characterisation of InAs/GaAs 1.3μm Quantum Dot Broadband Superluminescent LED". Jrnl. of Appl. Phys. Lett. (Accepted for publication)

[31] B. W. Hakki and T. L. Paoli "Gain spectra in GaAs double heterostructure injection lasers" J. Appl. Phys, Vol 46, No. 3, March (1975).

[32] S. K. Ray, K. M. Groom, M. D. Beattie, H. Y. Liu, M. Hopkinson, R. A. Hogg Broadband Superluminescent Light Emitting Diodes Incorporating Quantum Dots in Compositionally Modulated Quantum Wells". IEEE Photonics. Technol.. Lett. Vol. 18, Issue 1, 58-60. (Jan.1 2006).

[33] B. Považay, private communication.

[34] S. K. Ray, K. M. Groom, H. Y. Liu, M. Hopkinson, R. A. Hogg "Broad-band Superluminescent Light Emitting Diodes Incorporating Quantum Dots in Compositionally Modulated Quantum Wells". Jpn. Jrnl. of Appl. Phys., Vol. 45 No. 4A, (2006).

Chapter 5: Publications came out of this work

Journal publications:

1> H. Y. Liu, S. L. Liew, T. Badcock, D. J. Mowbray, M. S. Skolnick, S. K. Ray, K. M. Groom, F. Hasbullah, C. Y. Jin, M. Hopkinson, and R. A. Hogg *"P-doped 1.3-μm InAs/GaAs quantum-dot laser with low room-temperature threshold current density and high different efficiency"*.Appl. Phys. Lett.(Accepted for publication).

2> S. K. Ray, H. Y. Liu, T. L. Choi, K. M. Groom, S. L. Liew, M. Hopkinson, R. A. Hogg "*Molecular Beam Epitaxial Growth of High Power Quantum Dot Superluminescent Diodes*" Jpn. Jrnl. of Appl. Phys. (Accepted for publication).

3> S. K. Ray, T. L. Choi, K. M. Groom, H. Y. Liu, M. Hopkinson, R. A. Hogg *"High Power 1.3μm Quantum Dot Superluminescent Light Emitting Diode with Thin Low Temperature GaAs Spacer Layer in the Active Region"*. (Accepted for publication, IEEE Photon. Technol. Lett.)

Poster and conference presentation:

1> Oral presentation CLEO/QELS *"Broadband and High Power Quantum Dot Superluminescent Diodes"*. 21st-26th May 2006, Long Beach,CA, USA

Chapter5: High Power Quantum Dot Superluminescent Light Emitting Diodes Grown by Molecular Beam Epitaxy

5.1 Introduction

One of the most important parameters for a Superluminescent light emitting diode is the output power. For some applications like optical coherence tomography high output power is required. In previous chapters methods for broadening the emission spectrum have been demonstrated. In this chapter a method for increasing the output power for QD SLEDs is demonstrated. By the incorporation of a thin low temperature grown barrier layer in between the DWELLs of the SLED/laser material, a high quality devices are obtained. The SLED, laser, and mesa diode structures fabricated from this MBE grown material exhibit enhanced performance compared to "conventional" devices with thicker low temperature grown barrier layers. In this chapter it has been shown that this method is effective to produce material with considerably reduced defect densities, as evidenced by the electrical and optical performance of the devices.

5.2 Previous work

Several methods have been used before to increase the output power of a SLED. Using a fiber power amplifier is one of those methods [1]. In this method the output of a SLED is amplified using an Er-doped fiber amplifier (EDFA) to get an optical source with high output power (20mW) emitting around 1550nm. Optical source realized using this method have a small spectral modulation depth and are good for applications like gyroscopes. Another method used to increase the output power of the SLED is a tapered optical semiconductor amplifier seeded by a SLED [2]. Later a combination of an edge emitting LED and a single transverse-mode semiconductor amplifier was used to achieve high power as well as high modulation bandwidth [3]. This device utilizes the broad emission bandwidth of the LED and the gain of the amplifier section. The emission peak for this source was around 1300nm. The main

disadvantage of these devices is the lack of compactness, because the amplifier is connected to the main optical source (SLED or LED) by a fiber or lenses. Monolithically integrated high power SLEDs were suggested and exhibited several years ago. The method to achieve a single chip high power SLED is to suppress the optical feed back from one facet of a laser chip. This was done in various methods. One of these methods is to suppress the lasing feedback by applying anti reflective coating to one facet of the laser [4]. Another method is to utilize a long unpumped region at the back of the ridge [5]. In recent years some other techniques like chirped quantum well (QW) or the tapered waveguide has been used to increase the emission band-width and output power of the SLED structure. High output powers of ~1W at 1550nm for an InGaAsP/InP SLED have been reported [6]. In this device a chirped quantum well active region has been used. Also the ridge structure was tapered.

In the last 10 years QD structures instead of QW structures have drawn attention because of the potential of high modulation speed over several gigabits, low temperature sensitivity; lower threshold current density, etc. [7]. One group in recent years has reported InGaAs QD SLED with 0.9W output power and 80nm of FWHM, but the peak emission wavelength is around 1000nm [8]. On the same material system another group also reported very high output power from their device but these devices also emit around 1000nm [9]. Very recently another group has reported InGaAs/InAs tilted ridge QD SLED with high output power of ~10mW at 10^0C and emitting around 1300nm [10]. Due to the low saturated gain of the quantum dot ground state, emission from the excited state of the QD s have been utilized to achieve high optical output power [10]. The high power InAs/GaAs QD SLEDs described in this chapter was grown by MBE by engineering the growth temperature of the spacer layer thickness. The detailed growth mechanism for these devices is described in the next section.

5.3 Growth of High Power Superluminescent LED

The 7-layer InAs/GaAs QD structures were grown by Dr Hui-Yun Liu and Dr Mark Hopkinson in a solid-source VG Semicon V90H Molecular Beam Epitaxy system on

3-in Si-doped GaAs (100) substrates. Each dot layer consisted of 3.0 monolayers of InAs grown on 2-nm $In_{0.15}Ga_{0.85}As$ and covered by 6-nm $In_{0.15}Ga_{0.85}As$ to give a dot-in-a-well (DWELL) structure. The 7-layer InAs/InGaAs DWELLs were separated by 50nm GaAs spacer layers [SPLs] and embedded between 150-nm GaAs layers, which were further confined by 50nm $Al_{0.4}Ga_{0.6}As$ layers. Within the GaAs barrier layers in the active region, 6nm thick regions doped with Be are grown 9 nm before each DWELL structure. The Be doping level corresponded to 12 acceptors per dot. Growth temperatures were 620^0C for the AlGaAs and 510^0C for the In containing layers. For sample VN519, following the deposition of the InAs/InGaAs DWELL, the initial 15nm of the LTG GaAs SPL was deposited at 510^0C, and then the temperature was increased to 580^0C for the remainder of the GaAs SPL. This is referred to as a high growth temperature spacer layer (HGTSL) step. For the second sample VN522, the LTG GaAs layer thickness is reduced to 2nm. The remaining 48nm is grown at the elevated temperature of 580^0C.

Another 6 layer DWELL structure, VN590 is grown keeping almost all other parameters same as the other two structures. The main difference for this structure is the low temperature barrier layer is grown at 580^0C. This structure is also doped by Be at 12 acceptors per dot.

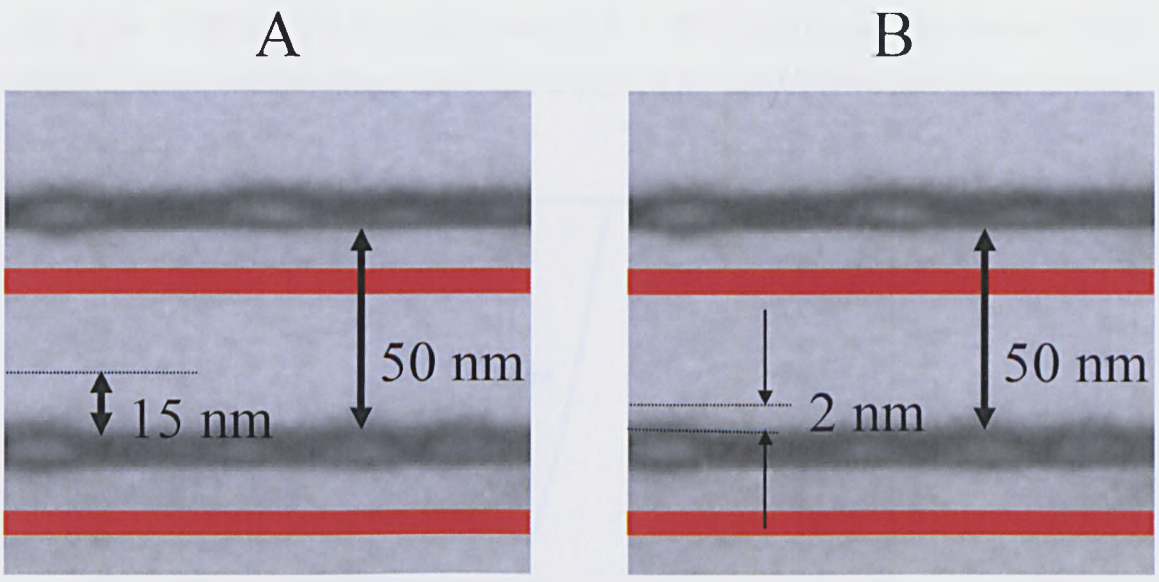

Fig. 5.1 Schematic cross sectional TEM image for the active regions of VN519 and VN522 samples showing the thickness of the low temperature grown barrier layers

5.4 Fabrication of the device

Both types of material were processed into narrow stripe lasers, SLEDs and mesa diodes. The fabrication methods are same as described in chapter 2. All the devices were shallow etched and selectively gold electroplated. The etch depth for all the devices is ~1.7μm. The laser devices are electroplated with ~2μm gold where as the SLED and mesa diodes are electroplated with ~1μm gold as there is problem with the thicker gold plating for the tilted facet ridges. This problem has been discussed in chapter 2. Laser devices were cleaved into pieces of different lengths. SLEDs are also cleaved into 6mm and 8mm long devices. The laser and SLED devices are mounted and bonded on the ceramic tiles. The mesa diodes are probed directly during the characterization.

5.5 Result and Discussion

5.5.1 Current Power characteristics of the SLED device

Pulsed current density-power characteristics for VN519 and VN522 SLED have been plotted in Fig. 5.2(a) and Fig. 5.2(b) respectively.The measurement was taken at room temperature and a pulsed current source was used with a maximum output of 500 mA. 1μm pulse width and 1% duty cycle was used for this experiment. The devices are of different length and the ridges are 15μm wide. All the curves have been taken at room temperature.

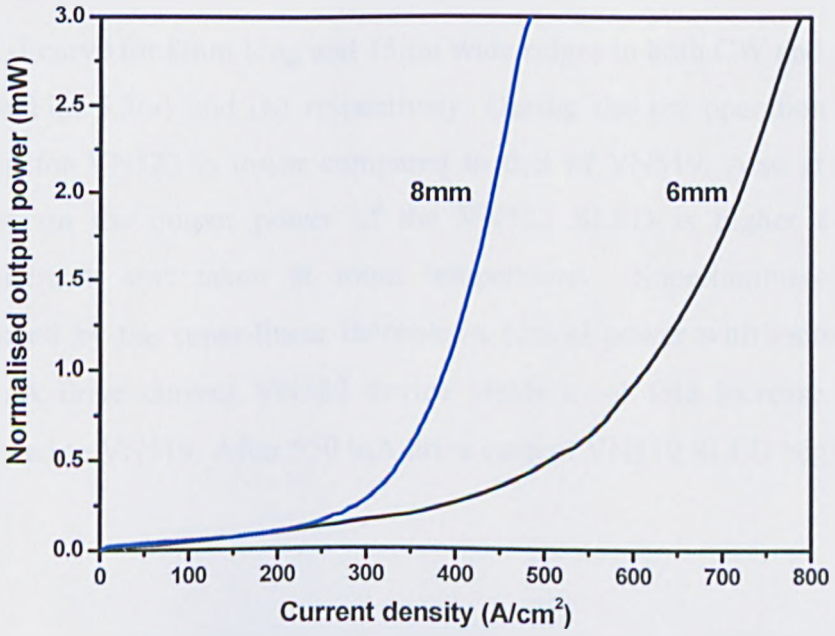

Fig. 5.2(a) Pulsed Current-power characteristics for two 15μm wide VN519 cavities of different length

It is clear from the graph that the behavior for these two devices is quite different with VN522 showing considerably enhanced performance compared to VN519. As the experiment is performed in the pulsed regime, the effect of temperature on the turn on current is removed and the value of output power is expected to depend on the spontaneous emission efficiency and the current-gain relationship for the material [11, 12]. These two aspects are discussed later in this chapter via the study of laser and mesa diode structures.

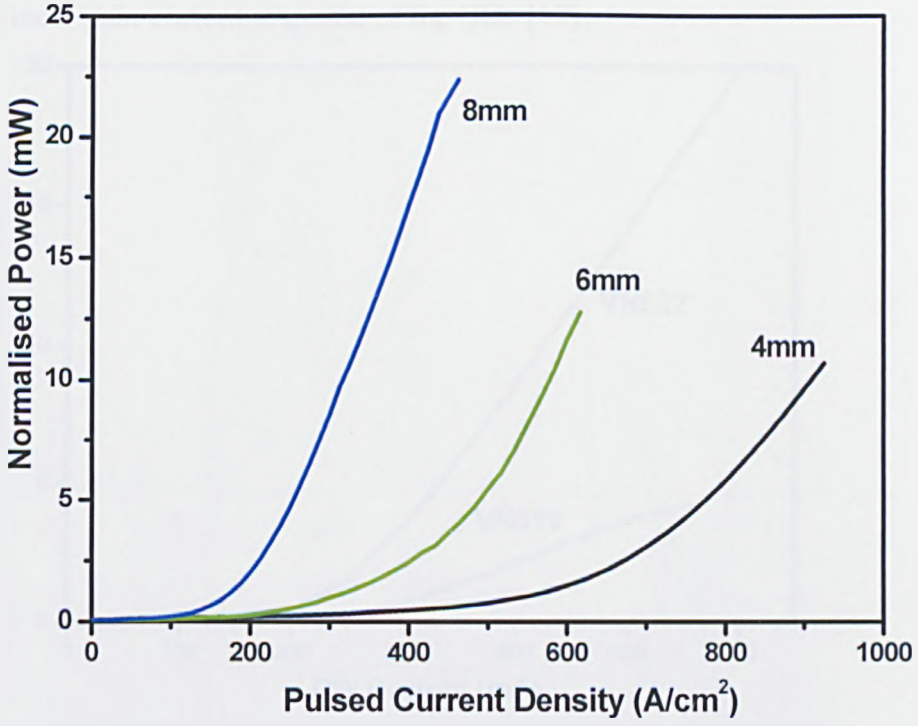

Fig. 5.2(b) Pulsed Current-power characteristics for 15μm wide VN522 cavities of different length

The L-I curve for 8mm long and 15μm wide ridges in both CW and pulsed regime are shown Fig. 5.3(a) and (b) respectively. During the cw operation also the turn on current for VN522 is lower compared to that of VN519. Also at any current after turning on the output power of the VN522 SLED is higher than VN519. The measurement was taken at room temperature. Superluminescent behaviour is evidenced by the super-linear increase in optical power with increasing current. At 500 mA drive current VN522 device yields a ~4 fold increase in output power compared to VN519. After 550 mA drive current VN519 SLED begins to exhibit roll-over.

The pulsed current power characteristics for SLED devices fabricated from samples VN519 and VN522 are plotted in Fig. 5.3(b). The same devices are used this time for the pulsed L-I measurement. The measurement was taken at room temperature and a pulsed current source was used with a maximum output of 500 mA. Super-luminescent behaviour is evidenced by the super-linear increase in optical power with increasing current from very low currents (transparency current density is $<25 Acm^{-2}$ for VN522). This is followed by an almost linear power-current response attributed to the non-linear gain-current response of the QDs [12].

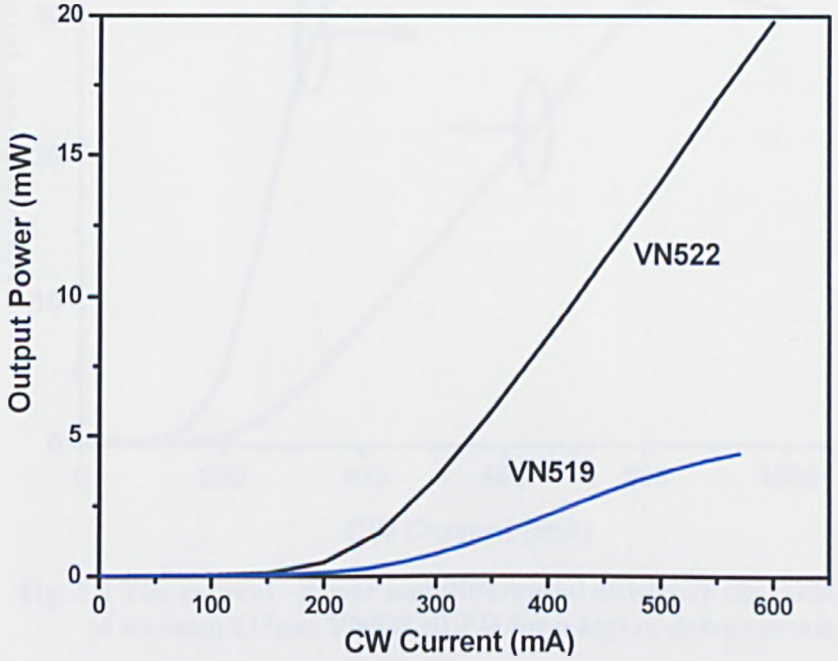

Fig. 5.3(a) CW Current-power characteristics for 8mmX15μm wide VN519 and VN522 cavities of different lengths

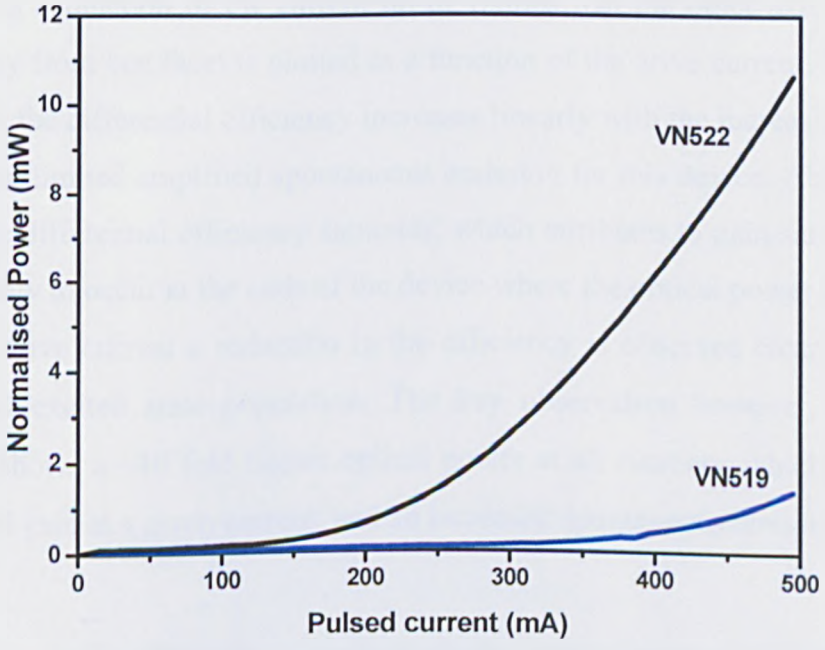

Fig. 5.3(b) Pulsed Current-power characteristics for 8mmX15μm wide VN519 and VN522 cavities of different lengths

Modelling of the output power for a SLED is not trivial because neither device shows strong amplified spontaneous emission at the same drive currents. The modelling of the emission requires detailed knowledge of the spontaneous emission efficiency, gain spectrum at each current, gain recovery times, etc.

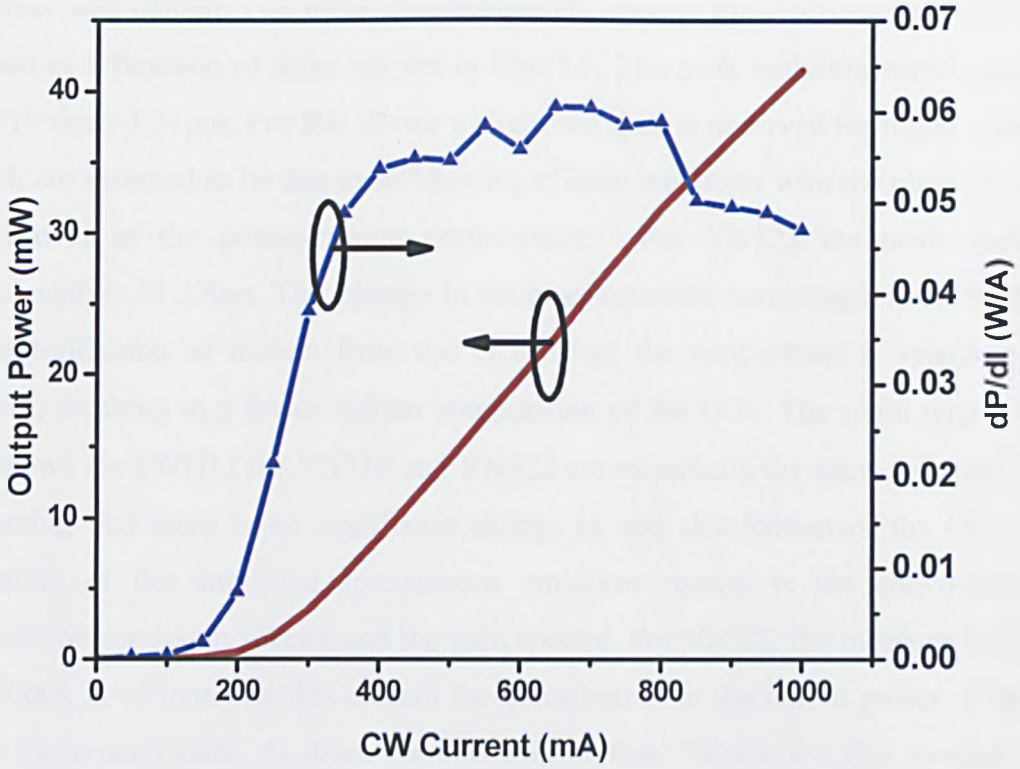

Fig. 5.4 The current –power and differential efficiency characteristics of an 8mmX15µm VN522 SLED for a higher drive current

In Fig. 5.4 the output power of the 8mm long, 15µm wide VN522 cavity has been plotted as a function of cw current up to 1Amps. On the other axis the differential efficiency from one facet is plotted as a function of the drive current. For the currents <350mA the differential efficiency increases linearly with the increasing drive current indicating limited amplified spontaneous emission for this device. Above that current value the differential efficiency saturates, which attributes to gain saturation which is more likely to occur at the ends of the device where the optical power is highest. After 800mA drive current a reduction in the efficiency is observed clearly indicating an increased excited state population. The key observation however, is that sample VN522 shows a ~10 fold higher optical power at all currents, which is attributed to increased gain at a given current, and an increased spontaneous emission efficiency.

5.5.2 Electroluminescence for VN519, 522

Electroluminescence spectroscopic measurements for both 8mm long and 15μm wide devices were performed under CW drive conditions. The resolution of the spectrum analyser was 0.06nm.The room temperature EL spectra for VN519 and VN522 are plotted as a function of drive current in Fig. 5.5. The peak emission wavelength for VN519 was ~1.31μm. For this device a slight red shift is observed for higher currents which are assumed to be due to self-heating effects consistent with the observation of a roll-over in the power-current performance. For VN522 the peak emission wavelength is ~1.27μm. This change in the peak emission wavelength is attributed to the out-diffusion of indium from the QDs when the temperature is raised during growth, resulting in a lower indium composition of the QDs. The room temperature EL shows the FWHM for VN519 and VN522 are essentially the same (~26nm) [13], indicating that there is no significant change in size distribution of the QDs. The linewidth of the amplified spontaneous emission spectra is the convolution of spontaneous emission spectra and the gain spectra. For VN522 the measured FWHM at 750mA is ~25nm. At this current the contribution to the output power is mainly from the ground state. At drive currents greater than 750mA the first excited state (~1.21μm) of VN522 begins to contribute to the output power, coincident with the step change in external efficiency observed in Fig.5.4.

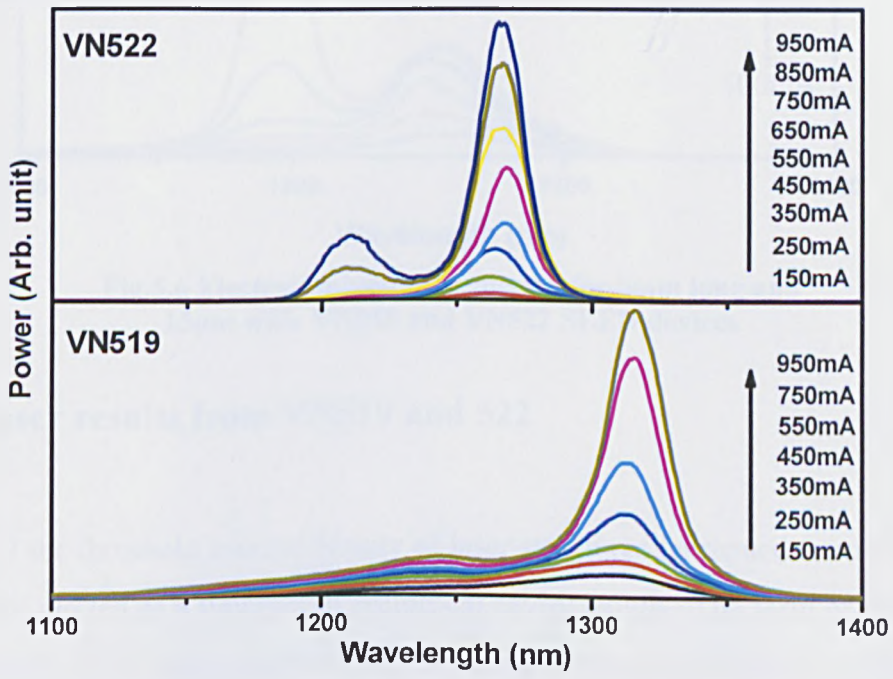

Fig.5.5 Electroluminescence spectra for 8mm long and 15μm wide VN519 and VN522 SLED devices

It is interesting to note that following the appearance of the kink in the P-I curve, the ground state emission continues to increase in intensity, and the excited state emission becomes significant. Such a kink in a laser would correspond to the saturation of ground state gain and the build up of a significant population of the excited state [14]. It is possible that the appearance of the kink corresponds to the saturation of ground state gain at the ends of the SLED ridge where the photon density is highest.

Figure 5.6 shows the room temperature CW EL spectra for 6mm long 15μm wide ridges of both the devices. The 500mA the spectra are very broad for VN519 (consisting of roughly equal ground and excited state populations), but the output power of this device is very low (<0.2mW). On the other hand for the 6mm long VN522 at 500mA the output power is >5mW.

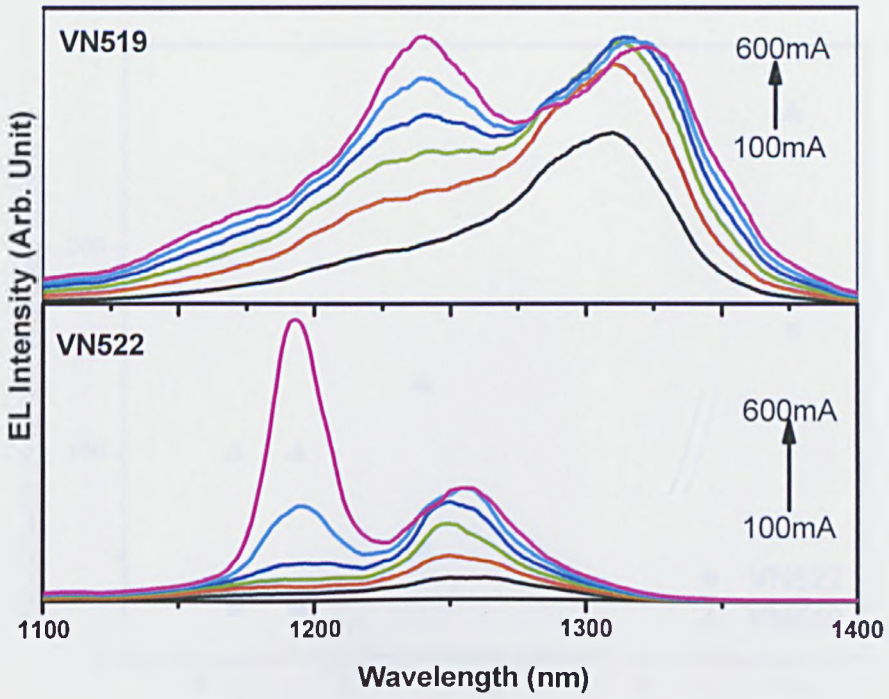

Fig.5.6 Electroluminescence spectra for 6mm long and 15μm wide VN519 and VN522 SLED devices

5.5.3 Laser results from VN519 and 522

In Fig. 5.7 the threshold current density of laser structures fabricated from VN519 and VN522 are plotted as a function of reciprocal cavity length. The form of this graph is characteristic of QD laser structures with a strong increase in threshold current density

for short cavities due to ground state gain saturation and the population of the excited states of the QDs [15].

From this graph a clear and dramatic reduction in the threshold current density of VN522 laser devices compared to VN519 lasers is observed. The threshold current density for VN522 with a 4mm long as-cleaved cavity is 23 Acm^{-2}. Previously we reported record low threshold current densities of 17 Acm^{-2} for HR/HR coated 3 DWELL materials [16] which with cleaved facets for identical cavity length and ridge width gave a threshold current density of ~60 Acm^{-2}. This indicates the very high material quality obtained by reducing the thickness of the low temperature GaAs capping layer, and the possibility for realisation of extremely low threshold current density lasers if these devices were also HR/HR coated.

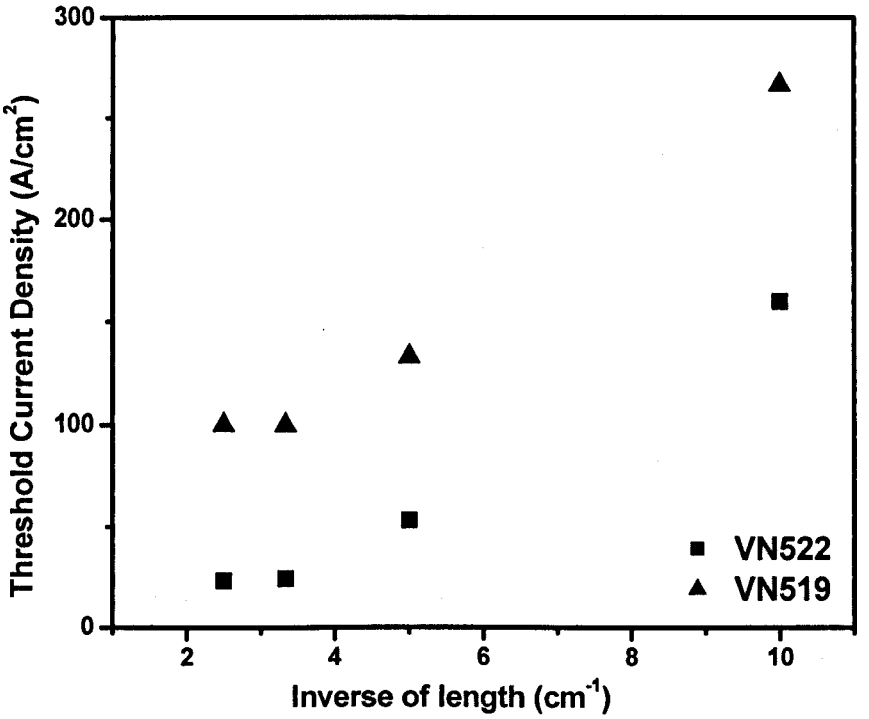

Fig.5.7 Threshold current density plotted as a function of inverse cavity length of VN519 and VN522 laser structures

The inverse of external differential efficiency is plotted as a function of the laser cavity length in Fig. 5.8. VN519 devices show a strong decrease in external differential efficiency for short cavity lengths (<2mm) which again is characteristic of

gain saturation of the QDs. Extrapolation of the linear region gives an internal quantum efficiency of ~40% and ~80% for VN519 and VN522 lasers, respectively. The internal loss is estimated to be ~ 1-2 cm^{-1} for both the VN519 and VN522 devices.

No significant change in the internal loss is observed indicating that improved device performance is not due to the reduced operating wavelength resulting in reduced inter-valance-band absorption. Though similar internal loss values are obtained for these two types of devices, the slopes for the line fitting, gives different values. It is observed that the 4mm long VN522 device exhibits higher threshold current density. This is attributed to the non-reproducibility of the cleaving. This could not be confirmed as only three points were available for the line fitting.

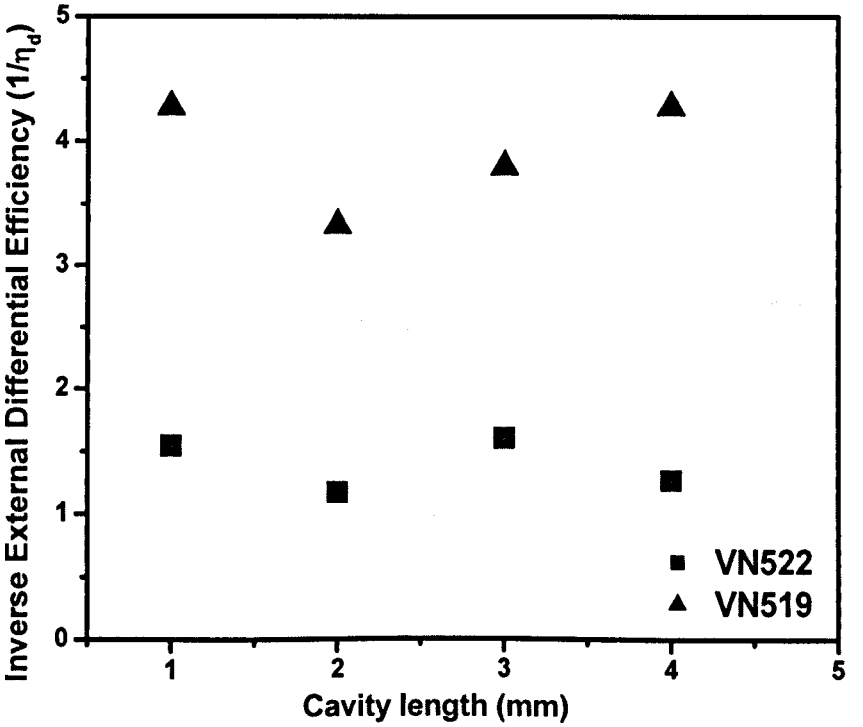

Fig.5.8 Inverse of External differential efficiency plotted as a function of cavity length of the VN519 and VN522 laser structures

These improvements in laser performance are attributed to two possible effects. Firstly, low temperature GaAs may be expected to be of higher defect density than high temperature GaAs. VN522 contains a smaller volume of low temperature GaAs. Secondly, annealing of the QD layers may reduce the number of dislocated QDs [13]. It is interesting to note that there is an almost constant difference between the threshold current densities of ~80 Acm^{-2} in Fig. 5.7. It is possible that this is the current required to saturate the additional non-radiative centers present in the GaAs grown at low temperature.

5.5.4 Reverse leakage current

The room temperature reverse leakage current was measured for both wafers fabricated into mesa devices with 100μm diameter. The measurement is taken in the dark so as to avoid photo generated carriers. The reverse leakage current for VN519 and VN522 is plotted in Fig.5.9. It is clear from the plot that the VN522 mesa diode has almost two fold breakdown voltage (~-23 volts) compared to that of VN519 (~-12 volts) mesa diode. It is clearly observed from the plot that the reverse dark current is also lower for VN522 at all reverse voltages. Also the breakdown knees for the VN522 mesa diodes are sharper than the breakdown knees for VN519 mesas. Such effects are symptomatic of a reduction in defect density within the active media directly resulting from reduction of the thickness of low temperature grown GaAs. The existence of fewer dislocations for the VN522 is discussed in detail later in this chapter with references of microscopic results.

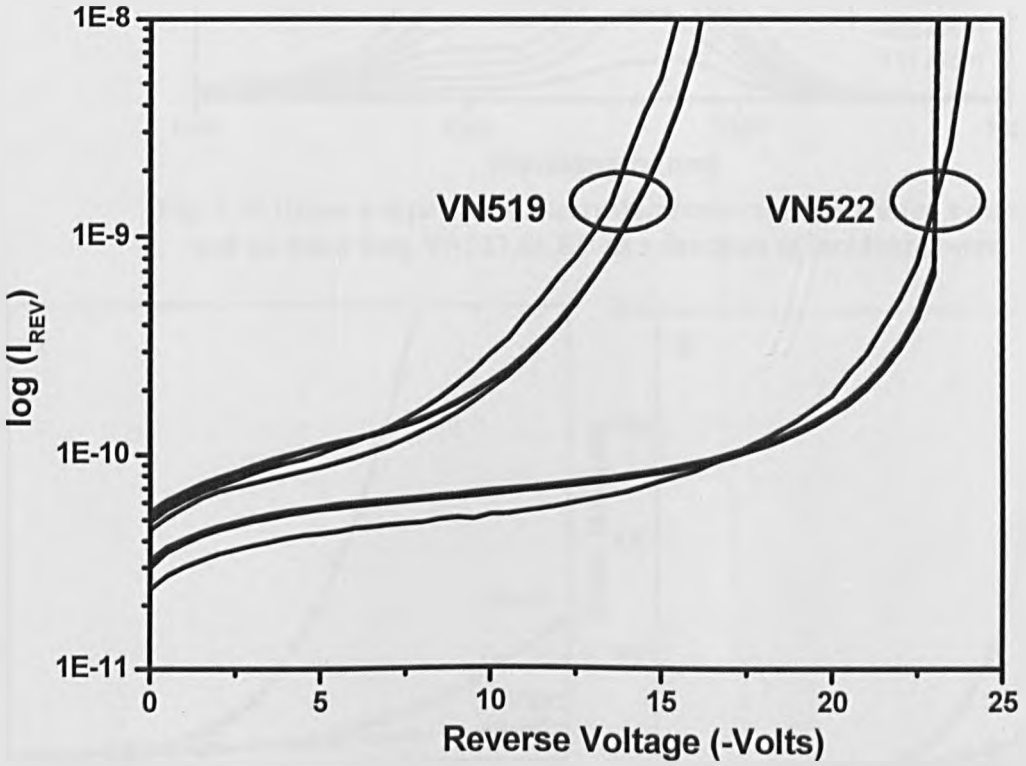

Fig.5.9 Reverse Leakage current plot for the VN519 and VN522 mesa structures at room temperature

5.5.5 Electroluminescence spectra for 6 and 8mm SLED device

The room temperature EL spectra as a function of cw drive current is plotted for 8 and 6mm long VN522 SLEDs in Fig. 5.10. The width of the ridge is 15μm and the spectra are taken at room temperature. For the 8mm cavity the excited state has significant intensity after a drive current of ~625A/cm^2 where as for the 6mm cavity it appears after ~444A/cm^2.

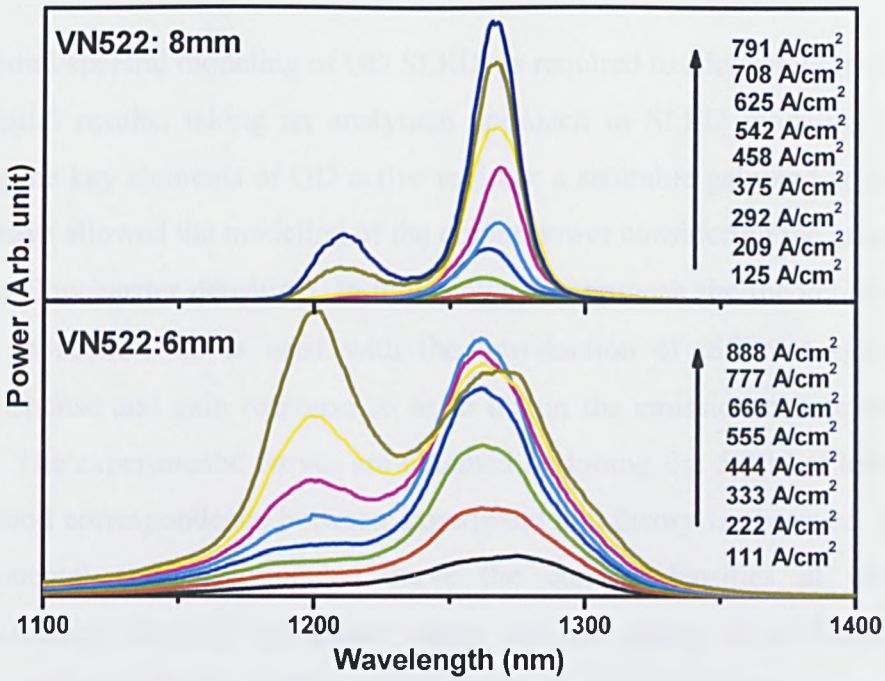

Fig. 5.10 Room temperature Electroluminescence spectra for a 6mm and an 8mm long VN522 SLED as a function of incident power

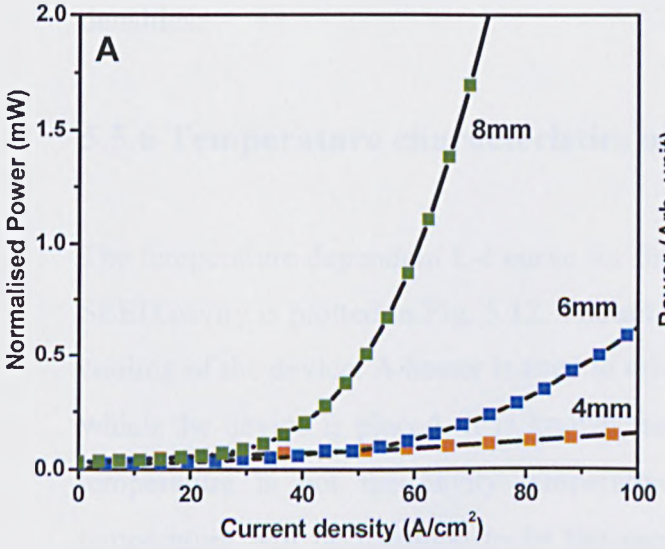

Fig. 5.11 (A) Experimentally obtained low current Superluminescence behaviour for 4, 6 and 8mm long SLEDs

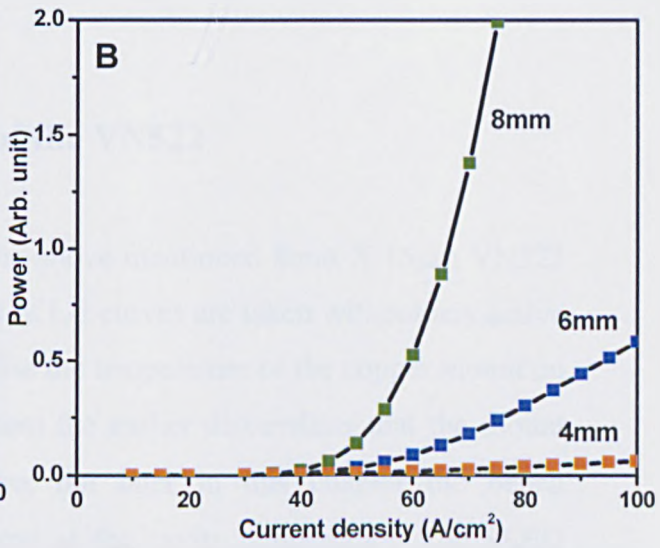

Fig. 5.11 (B) Modelled current density-power characteristics for 4, 6 and 8mm long SLEDs at low drive currents

Courtesy: T. L. Choi

Another important thing to notice for the 8mm long cavity is that the ground state does not exhibit any saturation (below 1Amp of drive current). In contrast, for the 6mm long cavity the ground state saturates after ~555A/cm^2 and the excited state begins to dominate the emission spectrum. Considering the ground-state emission, the reduced cavity length is expected to result in smaller powers. Also, carrier lifetime in the ground state can also be expected to be different, further complicating the modeling of the power and emission spectrum.

The full spatial/spectral modeling of QD SLEDs is required to adequately model these results. Initial results, taking an analytical approach to SLED modeling [11] yet introducing the key elements of QD active regions; a saturable gain and spontaneous emission) have allowed the modeling of the output power considering the ground state alone (i.e. at low carrier densities). In this analytical approach the theoretical model mentioned in section 4.3 is used with the introduction of different spontaneous emission response and gain response so as to obtain the emission characteristics of QD SLED. The experimental curves are obtained replotting fig. 5.2(b) at lower drive currents. Good correspondence between experiment and theory is observed. For both the experimental and the modeled curve the current densities at which the superluminescence turns on are almost same, also the nature of evolution of the curves are similar. This model incorporates the fundamental differences of QDs compared to QWs, namely a saturable spontaneous emission and gain at low current densities.

5.5.6 Temperature characteristics of the VN522

The temperature dependent L-I curve for the above mentioned 8mm X 15μm VN522 SLED cavity is plotted in Fig. 5.12. The set of L-I curves are taken without any active cooling of the device. A heater is used to raise the temperature of the copper mount on which the device is placed. It is known from the earlier discussions that the mount temperature is not the cavity temperature, but later in this chapter the bench temperature will be assumed to be the same as the cavity temperature. The SLED device exhibits >40mW of output power at 19^{0}C and as the temperature is raised the

output power drops as a consequence of the thermally sweep away of carriers from the QDs.

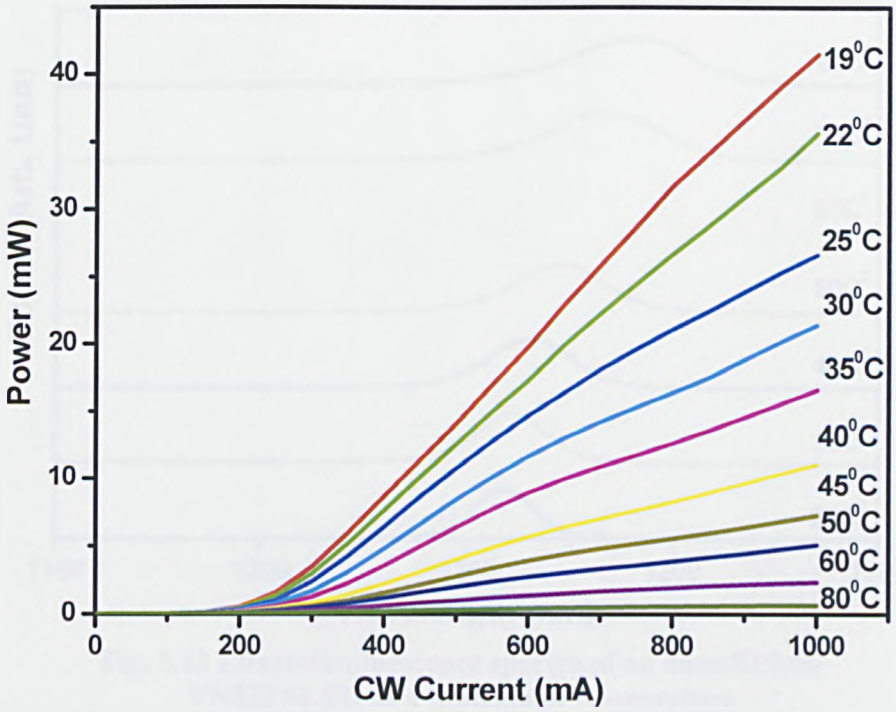

Fig. 5.12 Current-power characteristics of an 8mmX15μm VN522 SLED as a function of temperature

The EL spectra of the same device are plotted as a function of temperature in Fig. 5.13. At room temperature the device is observed to emit around 1260nm. As the temperature is raised a gradual red shift is observed. This red shift corresponds to the bandgap shrinkage due to the heating, an intrinsic property of the semiconductor. Also it is observed that with the increase in temperature the emission band broadens, which may be attributed to an increase in the homogeneous broadening. The device emits around 1290nm at 90^0C. It is observed that up to 100^0C no excited state appears also no evidence of thermal population of excited state is observed. Above this temperature it is not possible to capture any EL spectrum because as the homogeneous broadening increases the peak gain fall which in turn reduces the output power. Also from the temperature dependent L-I curve no switching to the excited state is observed. Beyond this temperature both the L-I curve and the EL spectrum can not be captured due to very low output power, so it is unknown at what temperature the excited state may appear for this device. An investigation with a shorter cavity could give some idea about the temperature sensitivity of this device.

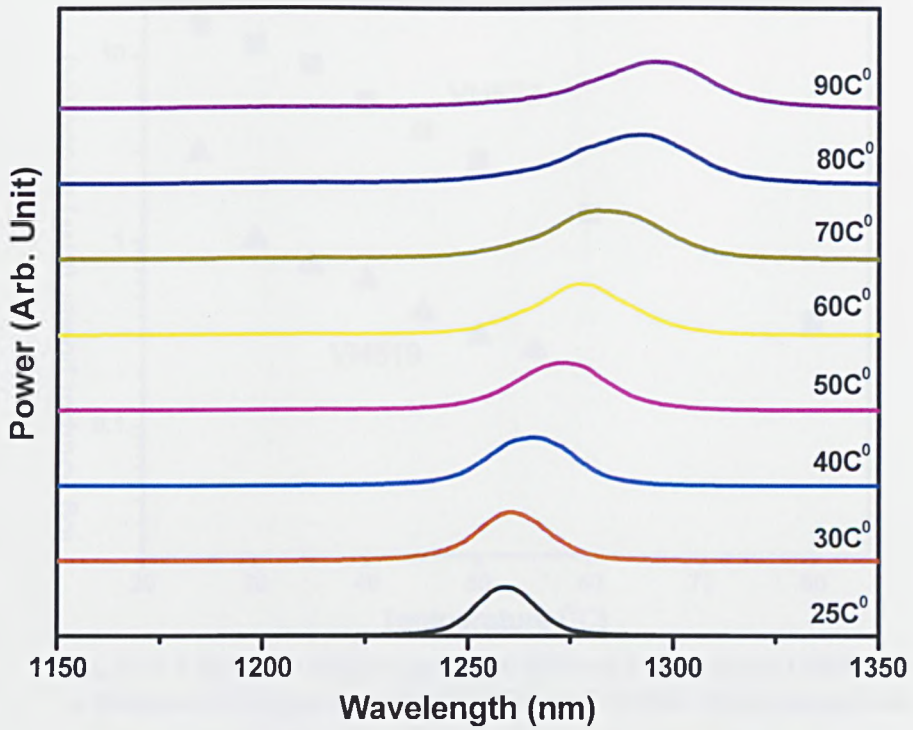

Fig. 5.13 Electroluminescence spectra of an 8mmX15μm VN522 SLED as a function of temperature

From the L-I curve it is evident that VN522 SLED device emits a very high output power compared to any device mentioned in this thesis. Though the output power for this device is very high, it is still sensitive to temperature. To investigate the temperature sensitivity of this device compared to VN519 SLED, a plot of the output power at a particular drive current is shown in Fig. 5.14. The log of the output power is plotted for both types of devices with the same geometrical dimension. The output power of the VN519 and VN522 SLED is recorded at 550mA drive current at room temperature and the log of that power is plotted as a function of cavity temperature. It is observed that the output power for the VN519 cavity is always lower than that of VN522 cavity. At lower temperatures (20-30^{0}C) VN519 is very sensitive to the temperature and the output power falls down rapidly, in contrast to VN522, suggesting a different mechanism for non-radiative recombination of carriers. At higher temperatures the fractional reduction in power is roughly similar for both devices suggesting a common mechanism.

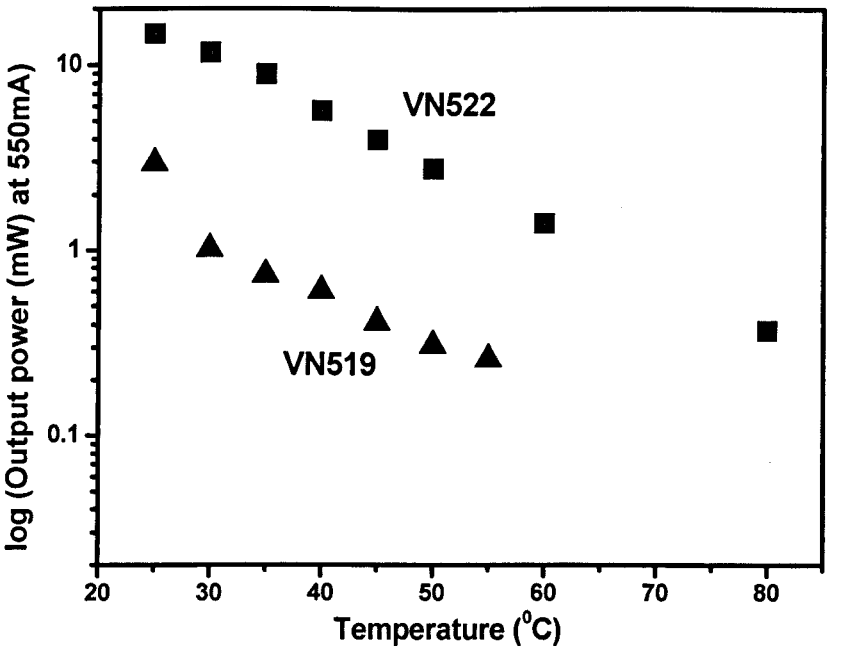

Fig. 5.14 Log of the output power at 550mA drive current plotted as a function of temperature for VN519 and VN522 SLED structures

The precise effect of defect density on the temperature sensitivity of the SLED device is still unknown (indeed the precise nature of these defects is not known) and requires detailed investigation, but from these results it can be concluded that thinner low temperature GaAs barrier layer helps improving the output power temperature dependence.

5.5.7 Analysis of samples using microscopic methods

A number of issues, like the emission wavelength shift for the VN522 samples or the existence of defects in those two samples, are explained in this section using the microscopic evidences from the uncapped and capped samples with the growth stopped before the high temperature growth step at the barrier layer.

It has been observed that the size of the InAs/GaAs QDs emitting around 1300nm at RT is close to the critical dot size for the nucleation of dislocation. Atomic Force Microscopy (AFM) measurement has been carried out to check the possibility of the existance defected dots. Fig. 5.15(a) shows the AFM image of an uncapped structure. Two types of dots are observed in the image. One type is relatively large dots with

irregular shape, and a very low density of ~ 1×10^{6} cm^{-2}, and height in a range of 13-16 nm, and the second type is the small dots with a regular shape, a high density of ~ 4×10^{10} cm^{-2}, and smaller height of ~10 nm, as shown in Fig. 5.15(a). The large islands with irregular size are frequently observed in AFM image of InAs/GaAs QDs with relative thick InAs deposition around 3.0 ML. Cross-sectional TEM studies have been performed on this type of island. The investigation indicates that there are dislocations formed around the edges of this type of large dot, as shown in the inset of Fig. 5.15(a), while the small dots are coherent.

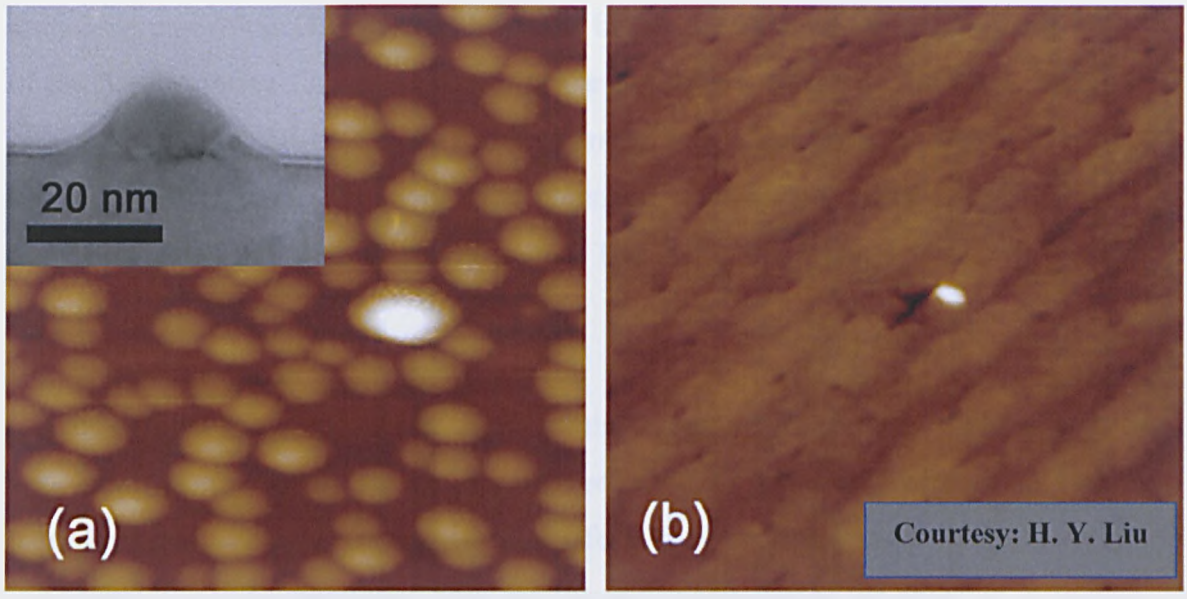

Fig. 5.15 (a) 500 nm × 500 nm AFM image of uncapped sample; and (b) 500 nm × 500 nm AFM image of InAs dots capped by 6-nm InGaAs and 2-nm GaAs. The inset in (a) shows the cross-sectional TEM of defected InAs islands.

Figure 5.15(b) shows the AFM image of a sample with 6nm of InGaAs capping layer on InAs dots and 2nm of low temperature GaAs layer. Growth of this sample is stopped after the growth of 2nm low temperature barrier layer and before the high temperature growth step. The sample is identical to the VN522 sample at the point of raising the growth temperature. From the AFM image a few islands and corresponding "holes" are observed on the surface of the sample. It is believed that the islands and the holes are originated from the different behaviour of the coherent

dots and the defective dots, and correspond to partially capped incoherent or defective dots as they have the same areal density.

For the coherent dots due to the deposition of the InGaAs capping layer a strain is formed at the base of the dots. This compression leads to the detachment of In atoms from the InAs dots resulting in a reduction in the dot size. Simultaneously the Ga atoms prefer to migrate away from the dots through the top of the InAs dots as consequence of the Ga atom related strain. Therefore small holes appear on top of the InAs dots as seen in Fig. 5.15(b). When the temperature is raised for the growth of the remaining part of the GaAs spacer layer the In atoms migrate away from the top holes of the dots resulting further reduction in the dot height. So for the VN522 sample a clear reduction in the In content is experienced and this leads to a blue shift in the emission wavelength. To keep the emission wavelength around 1300nm this migration of In atoms should be prevented. The method is discussed in the following section.

For the defective dots the change in the strain energy for the defected InAs islands is very small compared to that for the coherent dots. This happens because of full or partial relaxation of energy through the defects formed at the edges of the defected InAs dots. It is to be mentioned here that the lattice constant of the defected InAs dots is similar to that of the bulk InAs material, thus the defected dots tend to keep their size during the deposition of the this capping layer. This phenomenon resists the incorporation of Ga atoms into the dots and small islands are formed as seen in the AFM image in Fig. 5.15(b). When increasing the substrate temperature, In atoms within defected InAs islands will be evaporated. The difficulty of incorporating Ga atom into defected InAs dots could lead to the evaporation of whole defected dots during the step of increasing the substrate temperature. The elimination of defected InAs islands was also previously proven by TEM investigations on the sample with relative high-density defected dots.

From these microscopic evidences it is predicted that for the VN522 sample a better quality material is achieved due to the evaporation of whole defected dots during the high temperature growth step. Also the blue shift in the emission wavelength occurs due to the evaporation of In dots through the holes formed at the top of the dots during the high temperature growth step. To keep the emission wavelength around 1300nm it is thought that if the evaporation of In atoms through the holes on top of the non-defective dots is prevented then the emission wavelength can be pinned around 1300. To do this a sample was processed with 5nm low temperature grown GaAs barrier. The results from the SLED device fabricated from this material are shown in the following paragraph.

5.5.8 Keeping the emission wavelength around 1300nm

A sample was grown with 5nm low temperature grown GaAs in the barrier layer and the remaining 45nm were grown at the elevated growth temperature. It has been noticed during the microscopic observations that some holes are formed at the top of the non-defective dots due to the detachment of In atoms from the InAs dots and also due to the migration of the Ga atoms during the high temperature growth step.

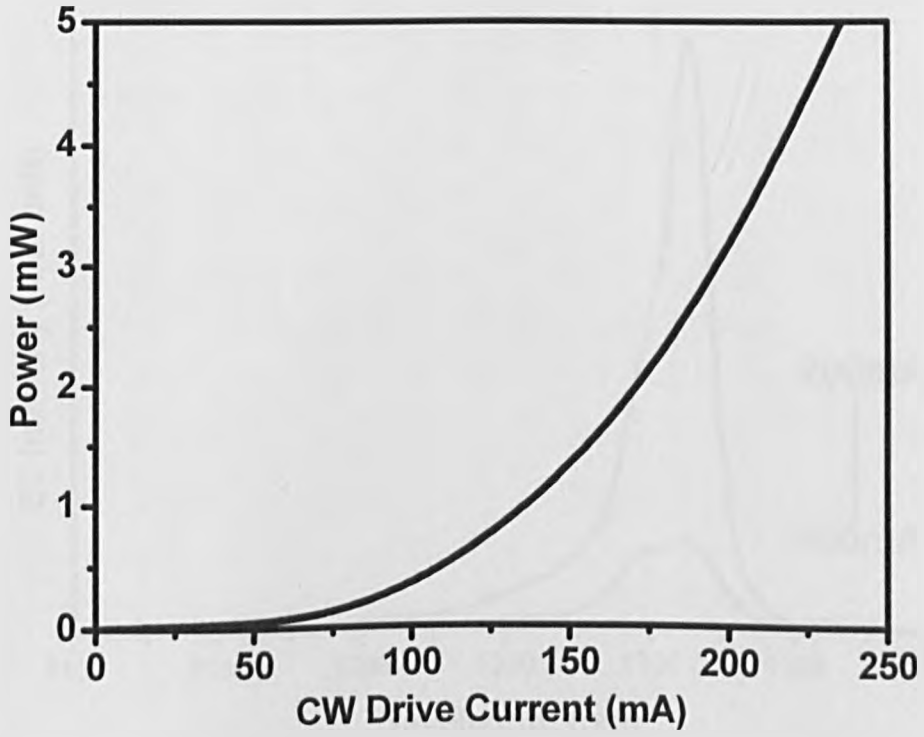

Fig. 5.16 Room temperature CW current-power characteristics for a 6mmX15μm SLED device

For the sample VN590 the holes are covered up by 5nm of low temperature GaAs barrier layer so as to prevent the migration of the Ga atoms and the evaporation of In atoms from the InAs dots.

It was thought that if the migration of In is prevented from the InAs dots during the high temperature growth step then the wavelength can be pinned to 1300nm, simultaneously a good quality, defect free material can be obtained. All the three samples are grown in the same manner, the only difference being the VN590 sample has a 5nm low temperature barrier layer and it has 6 DWELLs.

SLED devices are fabricated from VN590 material exactly in the similar manner as VN519 and VN522. The devices were mounted on the ceramic tiles and bonded by gold wires. The room temperature CW current-power characteristic of a 6mm long 15μm wide cavity is shown in Fig. 5.16. Superluminescence behavior is observed for the device. The turn on current density is very low for this device. However, above 225mA drive current the device is observed to lase. This phenomenon is confirmed by the room temperature EL spectrometry of the same device. The EL spectra for this device as a function of CW drive current is shown in Fig.5.17.

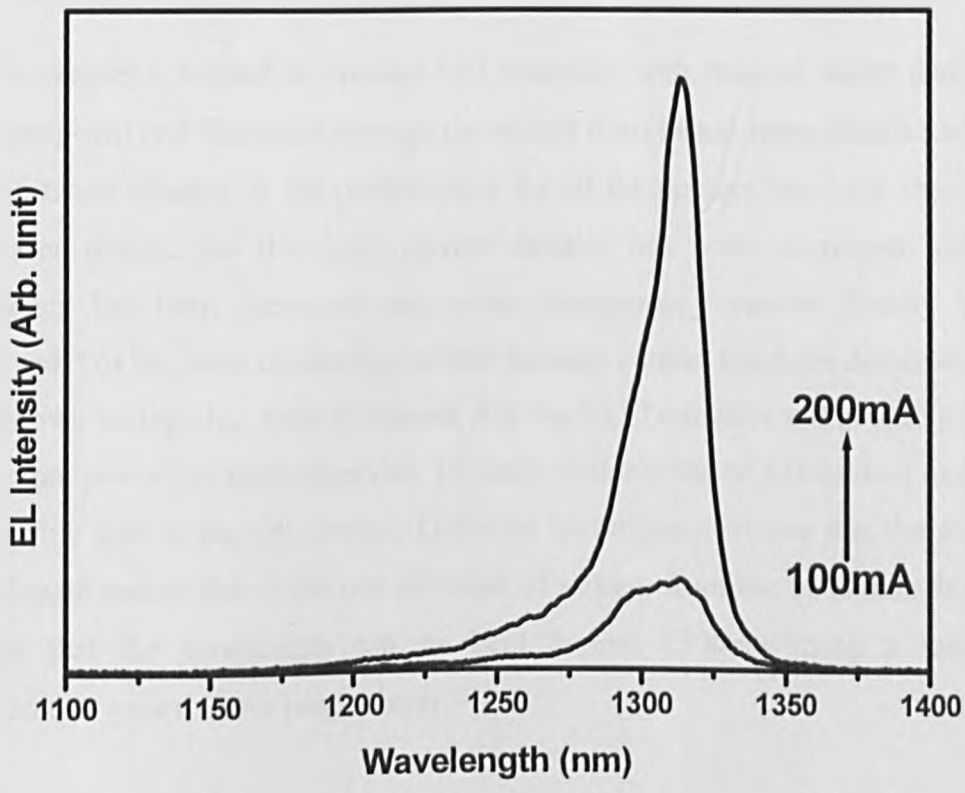

Fig. 5.17 Electroluminescence spectra as a function of CW drive current of the 6mmX15μm VN590 SLED

After 225mA drive current the device starts lasing. The measured FWHM for this device at 200mA is ~26nm, which is very similar to that of VN522. It is to be noticed that the emission wavelength is ~1300nm which is attributed to a direct effect of increased low temperature barrier layer than VN522. It seems that 5nm of low temperature GaAs enables to cover up the InAs dots preventing the out diffusion of In from the dots at the higher temperature. Also the high output power for this device is observed as a result of the high quality material produced by the thin low temperature barrier layer.

The main reason for lasing after a certain drive current is predicted to be due to the etch depth. The etching depth of all the SLED devices is around ~1.7μm. It was observed before that if the ridges of the SLEDs are etched deeper then the probability of lasing becomes higher. For this device also the etching depth is checked and it is found that the etching depth is slightly more (~1.9μm) than that of the other devices. The deep etch leads to an increase in the regenerative feedback from the facets which lead to lasing at high drive current.

5.6 Conclusion

In this chapter a method to produce QD materials with reduced defect densities has been proposed and discussed through the results from lasers, mesa diodes and SLEDs. A significant increase in the performance for all the devices has been observed. For the laser diodes, the threshold current density has been decreased; differential efficiency has been increased and lower transparency current density has been observed. For the mesa diodes the reverse leakage current has been decreased and the breakdown voltage has been increased. For the SLED devices a dramatic increase in the output power has been observed. The only problem the SLED devices experienced is the blue shift in the wavelength. Different investigation shows that the shift in the wavelength occurs due to the out diffusion of indium from the InAs dots. It has been shown that the wavelength can be kept around 1300nm using a thicker low temperature grown GaAs barrier layer.

5.7 Further work

Further investigations are required to determine the exact thickness of the low temperature grown GaAs barrier layer for which the emission wavelength can be kept around 1300nm. Furthermore, the precise reason for the improvements in device characteristics is still not entirely clear. The relative importance of defective dot removal compared to the reduction in volume of low temperature GaAs has not been entirely clarified. This may be achieved by growing structures similar to VN522 but with additional low temperature GaAs insertions to ensure a constant volume of low temperature GaAs. One important next step is to combine the emission band-width increasing work of chapter 4 with these epitaxial growth conditions for high power and bandwidth devices.

References

[1] N. S. Kwong, "High-power, broad-band 1550 nm light sources by tandem combinationof a superluminescent diode and an Er-doped fiber amplifier" IEEE Photon. Technol. Lett.4, 9, 996-999, (1992).

[2] L. Goldberg and D. Mehuys, "High power Superluminescent diode source", Electron. Lett. 30, 1682-1684, (1994).

[3] K. Y. Liou and G. Raybon, Operation of an LED with a single-mode semiconductor amplifier as broad-band 1.3-μm transmitter source IEEE Photon. Technol. Lett. 7, 1025, ()

[4] I. P. Kaminow, G. Eisenstein, L. W. Stulz and A. G. Dentai, IEEE Jrnl. Quantum Electron. 25, 696-704 (1983).

[5] N. S. K. Kwong, K. Y. Lau, N. bar-Chaim IEEE J. Quantum Electron. 25, 696-704 (1989).

[6] T. Yamatoya, S. Mori, F. Koyama, K. Iga "High power GaInAsP/InP strained quantum well superluminescent diodewith tapered active region" Jpn. J. Appl. Phys, 71, 5121-5122, (1999).

[7] D. Bimberg, M. Grundmann, F. Heinrichsdorff, N. N. Ledentsov, V. M. Ustinov, A. E. Zhokov, A. R. Kovsh, M. V. Maximov, Y. M. Shernyakov, B. V.Volvik, A. F. Tsatsulnikov, P. S. Kop'ev, Zh. I. Alferov. "Quantum dot lasers: breakthrough in optoelectronics", Thin Solid Films, 367, 235-249, (2000)].

[8] D.C. Heo, J.D. Song, W.J. Choi, J.I. Lee, J.C. Jung, I. K. Han "High power broadband InGaAs/GaAs quantum dot superluminescent diodes" Electron. Lett. 39 (11), (2003).

[9] Z.Y. Zhang, Z.G. Wang, X.P. Jin, Z. Z. Sun, F.Q. Liu "High performance Quantum dot Superluminescent Diodes" IEEE Photonics. Technol. Lett. 16, (1), 27-29, (2004)].

[10] M. Rosseti, A. Markus, A. Fiore, L. Occhi, C. Velez. "Quantum dot superluminescent diodes emitting at 1.3μm", IEEE Photonics. Technol.. Lett. Vol. 17, No. 3, 540-542 (2005).

[11] Tien-Pei Lee, Charles A. Burrus, Jr and B.I.Miller. IEEE J. Quantum Electron., Vol. QE-9, No.8, 820-828 (1974),

[12] A.E.Zhukov, A.R.Kovsh, V.M.Ustniov, A.Yu.Egorov, N.N.Ledenstov, A.F. Tsatsul'nikov, M.V.Maximov, Yu.M.Shernyakov, V.I.Kopchatov, A.V.Lunev, P.S.Kop'ev, D.Bimber, and Zh.I.Alferov. Semicond. Sci. Technol. 118-123. 14(1999).

[13] H. Y. Liu, S. L. Liew, T. Badcock, D. J. Mowbray, M. S. Skolnick, S. K. Ray, K. M. Groom, F. Hasbullah, C. Y. Jin, M. Hopkinson, and R. A. Hogg "P-doped 1.3-μm InAs/GaAs quantum-dot laser with low room-temperature threshold current density and high different efficiency" Appl. Phys. Lett.(Accepted).

[14] S. K. Ray, K. M. Groom, R. A. Hogg, H.Y. Liu, I R. Sellers, M. Hopkinson, T. J. Badcock, A. J. Ramsay, D. J. Mowbray, M. S. Skolnick. "Growth, Fabrication, and Operating Characteristics of Ultra-Low Threshold Current Density 1.3 μm Quantum Dot Lasers". Jap, J. Appl. Phys. 44(4B), 2520-2522, (2005).

[15] Rosseti, A. Markus, A. Fiore, L. Occhi, C. Velez. "Quantum dot superluminescent diodes emitting at 1.3 μm" IEEE Phot. Tech. Lett 17, (3), 540-542, (2005).

[16] H.Y. Liu, D.T. Childs, T.J. Badcock, I.R. Sellers, M. Hopkinson, R.A. Hogg, D.J. Robbins, D.J. Mowbray, M.S. Skolnick "High-performance three layer 1.3 μm InAs-GaAs Quantum-dot lasers with very low continuous-wave room-temperature threshold currents" IEEE Phot. Tech. Lett. 17(6), 1139-1140, (2005).

Chapter 6: Conclusion

In this thesis the epitaxial growth and fabrication of different types of quantum dot device, and the characterization of those devices has been described through successive chapters. Different aspects of the device performance and the engineering of these structures to bring about improvements in various figures of merit have been described in detail. Simultaneously, many problems and unanswered questions which arose could not be properly investigated during my studies have been highlighted. The main achievements and unanswered questions of the work outlined in this thesis are summarized in the following paragraphs.

Different fabrication and characterizing techniques have been outlined in chapter 2. During the fabrication of lasers or SLEDs, a few parameters needed to be optimized, in part due to the special characteristics of quantum dot active regions. In chapter 3, a technique for improving the temperature characteristics of lasers has been described which involves a shallow ridge etching (removing the top AlGaAs layer) and selective gold electroplating (~3.2μm) [1, 2]. By contrast, for the fabrication of SLEDs it was observed that some gold flaps of thick electroplated gold covered the facet of the SLED after cleaving. Results from these facets were erroneous and some times no useful emission was obtained from the facets. To cure this problem the thickness of the electroplated gold was reduced to ~1μm for the SLEDs.

It has been mentioned in chapter 2 (Sec. 2.4.1) that both dry and wet chemical etching was compared for deeply etched laser devices and the wet chemically etched lasers, showed lower threshold current densities. Later from the work mentioned in chapter 3 it was observed that wet chemically etched shallow etched ridges with selective electroplating exhibit better temperature performance. It would be useful to extend this work to investigate the performance of dry etched shallow and electroplated ridges, with more work on developing the dry etch process being carried out.

Similarly, an investigation was carried out on the effect of etch depth on SLED performance. Three different etch depths were studied, termed; deep etch (~3.2μm), shallow etch (~1.8μm) and very shallow etch (0.5μm).

For uncoated SLED devices it was found that superluminescent behavior was not possible for the very shallow etched devices. This is attributed to the poor optical confinement from such a shallow etch, reducing the fraction of spontaneous emission guided within the waveguide. Also, current spreading is expected to result in lower current densities for the "very shallow etched" sample. For deeply etched SLED devices the optical confinement was so strong that it was impossible to achieve significant output powers without the device beginning to lase due to the non-zero facet reflectivities. If broad-band, low reflectivity facet coatings, or other methods to reduce effective facet reflectivity are implemented, then deeply etched SLEDs will require further investigation. For uncoated SLEDs the shallow ridge etch provides a good compromise between providing enough waveguiding to ensure superluminescence, but not so much that the effective facet reflectivity is still low enough to ensure lasing does not occur easily.

The general performance of 1.3μm QD laser with the high temperature grown spacer layer incorporated was described in Chapter 3. This material was processed into ridge waveguide lasers with a deep ridge etch (3.2μm) For these laser structures, 2mm long cavities are the shortest cavity to lase from the ground state and exhibit a record low transparency current density per QD layer (J_0= 1.5A/cm^2) [1, 2]. Later in chapter 3 the same material is processed into lasers with a shallow ridge etch and selective electroplating. Through the study of different figures of merit of the QD laser it was shown that this fabricated device design reduced the threshold current density at any temperature and in turn the external differential efficiency was also increased compared to deeply etched devices. Also, the rate of change in J_{th} and η_d with increasing temperature was reduced for the shallow etched and selectively electroplated device. A clear increase of 10K in the characteristics temperature (T_0) was also observed for these devices. Also, for the shallow etched device the simultaneous lasing is observed at ~85^{0}C, which is ~15^{0}C degree higher than that observed for the deep etched device. All these results are a clear indication of the reduced temperature sensitivity for the shallow etched and electroplated devices.

The reasons for this improvement are predicted to be three fold. Firstly the shallow etching of the wet etched ridges reduces the electrical losses along the sidewalls of the

ridges due to the wet chemical etching and the reduced sidewall length. Secondly the shallow etching of the ridge confines the optical mode completely in the active region. And the last reason is attributed to be the better heat dissipation as a direct result of the selective electroplating of the bondpads.

However, a few phenomena are not answered from the results shown in that chapter. While improved heat sinking due to the selective gold electroplating is not the sole reason for the improvement in the temperature characteristics of the devices, the precise contributions of reduced optical and electrical loss at the ridge sidewall has not been clarified. Another interesting factor was observed during the EL measurement of the devices as a function of drive current. It was observed that, when the emission wavelength switches to the excited state, the ground state emission diminishes instead of saturating. As the theory suggests, the ground state should be clamped and the excess carrier injected should contribute to the excited state emission, but in reality it was observed that the ground state emission is suppressed as the excited state lasing develops. The reason for this behavior is not clear. This has been attributed to a common hole population for the ES and the GS, an increase in homogeneous line-width, reducing the peak gain of the ground state [3], or could be due to self-heating. Further work is required to determine the exact mechanism. The gain measurement of a short cavity laser can be informative so as to find out the reason of this phenomenon. The control of this mechanism could give rise to a novel modulation scheme for QD laser devices.

A novel technique for broadening the emission spectrum of a SLED is described and discussed in chapter 4. Using a 5x DWELL structure with different indium composition in different wells a SLED with 2.5mW CW output power and 85nm broad emission spectrum, with the peak emission wavelength around 1.27μm, was realized at room temperature [4, 5]. Also, a very broad gain spectrum of 100nm width was achieved [6]. The broadening is based on the principle of overlapping the ground state and the excited state emission from different In containing wells. This overlapping is evidenced from both the laser and the SLED results. Later in chapter 4 this technique is modified to incorporate an array of 6x DWELLs with different In compositions in order that the individual emission peaks of different wells are

separated by their line widths. The result is a broad flat-topped emission spectrum. With this new array of wells a SLED with ~95nm broad, flat-topped emission spectrum and 8mW output power is achieved at room temperature [7, 8]. The emission spectrum of this structure is spread over the range of 1200-1300nm.

From these results it is clear that the DCMWELL structure exhibits a broad emission spectrum and further development exhibits a broader emission spectrum and higher output power. For the 6x DWELL SLED structures p-type modulation doping was employed at a level of 12 acceptors per dot. The reason for this enhanced output power for this 6x DWELL structure compared to the DCMWELL structure may be either due to the p-type modulation doping or due to the increased number of DWELLs or maybe both. The exact contribution for each of these two factors is unknown. Further investigation on these two structures with/without p-type modulation doping can provide an answer and also can give an indication about how much these two factors contribute in enhancing the output power of the SLED device.

A broadening of the emission band-width of a SLED was obtained by incorporating the DCMWELL design in two forms. Using the same concept some other design combinations like 6 different indium containing wells, or some other different array of the wells could show better results. It would be useful to try other combinations in future. Also the maximum In content could be increased though it has been observed before that the emission intensity from the DWELLS with higher In content reduces. But increasing the range of the In content could result in a broader emission spectrum in the desired wavelength region.

Another issue regarding the DCMWELL structure to be considered in future is active thermal management. As the DCMWELL structure consists of different amount of In composition in different wells the confinement of the carriers can be expected to be poorer for the lower In containing wells. Though it has been observed that at low injection carrier density and at room temperature the carriers are evenly distributed in the active region [Sec. 4. 7. 2], but at higher current operation the carriers of the lower In wells are expected to be thermally excited out of their confinement more readily than the higher In wells. Some active cooling techniques are suggested such as by

mounting the sample on a thermo-electric cooler and operating the device at a low temperature, say 10° C.

It has been observed through the work described in chapter 4 that the broadening of the emission spectra is possible using the DCMWELL structure. Other broadening mechanism are possible and worthy of future investigation. It has been mentioned before [Sec. 4. 12] that, if the InAs deposition rate is reduced a significant broadening in the emission spectrum is observed though the integrated intensity remains almost identical [9]. This behavior represents the transition from the ensemble being made up of small dots to the formation of larger dots due to the increased amount of InAs. QD SLEDs utilizing such 'immature' quantum dots would be an interesting route to broadband emission.

Chapter 5 outlines a technique for increasing the output power for narrowband SLEDs through the reduction of dislocations. In this chapter a method to produce QD materials with reduced defect densities was proposed and discussed through the results from lasers, mesa diodes and SLEDs. In this growth process the thickness of the low temperature grown GaAs spacer layer is reduced and an > 40mW CW output power is obtained from an 8mm long and 15μm SLED cavity at room temperature [10]. A significant improvement in the performance of mesa diodes and laser devices is also observed. For the laser diodes, the threshold current density was decreased; differential efficiency was increased and lower transparency current density was observed [11]. For mesa diodes the reverse leakage current was decreased and the breakdown voltage was increased by incorporating this new growth technique. The only problem with the SLED devices is the blue shift in the wavelength. Electrical and microscopic results suggest that this blue shift is due to the out diffusion of In from the dots and the complete evaporation of a defected dot [12]. The exact reason for the blue shift is unclear but it has also been shown that by the use of a thicker low temperature GaAs spacer layer we can keep the emission wavelength around 1300nm. Also the SLEDs fabricated from this material emit high output powers.

Further investigations are required to determine the exact thickness of the low temperature grown GaAs barrier layer for which the emission wavelength can be kept around 1300nm. Furthermore, the precise reason for the improvements in device

characteristics is still not entirely clear. The relative importance of defective dot removal compared to the reduction in volume of low temperature GaAs has not been entirely clarified. This may be achieved by growing structures similar to VN522 but with additional low temperature GaAs insertions to ensure a constant volume of low temperature GaAs. Also some other techniques like increasing the number of QD layers or using anti reflective facet coating can be used to increase the output power of the SLEDs.

The most important thing in scientific research is to adapt the gradual development and to incorporate novel techniques in future work. In this short span of time I have tried to follow that rule. The development in the fabrication technique described in chapter 3 has been incorporated in the work mentioned in the following chapters. Two different techniques for broadening the emission spectrum of SLEDs and to increase the output power of SLEDs has been described in chapter 4 and 5. Considering the primary requirements for different applications of SLEDs, like OCT it is important to achieve both broad emission band and the high output power. I hope that the work presented in this thesis goes some way to allow the realization in future of high power, broad emission bandwidth SLEDs.

Reference:

1> S. K. Ray, K. M. Groom, R. A. Hogg, H.Y. Liu, I R. Sellers, M. Hopkinson, T. J. Badcock, A. J. Ramsay, D. J. Mowbray, M. S. SkolnickJpn, Jrnl. of Appl. Phys. 44 (4B), 2520-2522, (2005).

2> S. K. Ray, K. M. Groom, R. A. Hogg, H. Y. Liu, M. Hopkinson, T. J. Badcock, D. J. Mowbray, M. S. Skolnick. IEEE Photon. Technol. Lett. Vol. 17, No. 9, September (2005).

3> M. Sugawara, N Hatori, T Akiyama, Y Nakata, H Ishikawa. Jpn. J. Appl. Phys. 40, L488, (2000).

4> S. K. Ray, K. M. Groom, M. D. Beattie, H. Y. Liu, M. Hopkinson, R. A. Hogg "Broad-band Superluminescent Light Emitting Diodes Incorporating Quantum Dots in Compositionally Modulated Quantum Wells". IEEE Photon.Technol. Lett. Vol. 18, Issue 1, 58-60. (Jan.1 2006).

5> S. K. Ray, K. M. Groom, H. Y. Liu, M. Hopkinson, R. A. Hogg "Broad-band Superluminescent Light Emitting Diodes Incorporating Quantum Dots in Compositionally Modulated Quantum Wells". Jpn. Jrnl. of Appl. Phys., Vol. 45 No. 4A, (2006).

6> S. K. Ray, K. M. Groom, R. Alexander, K. Kennedy, H. Y. Liu, M. Hopkinson, R. A. Hogg "Design, Growth, Fabrication and Characterisation of InAs/GaAs 1.3μm Quantum Dot Broadband Superluminescent LED" Jrnl. Of Appl. Phys. (100, 103105, (2006).

7> K. M. Groom, S. K. Ray, H. Y. Liu, M. Hopkinson, R. A. Hogg "Flat-Topped Emission Centered at 1250nm from Quantum Dot Superluminescent Diodes" (Submitted to Electron. Lett.)

8> K. M. Groom, S. K. Ray, T. Choi, B. Stevens, H. Liu, M. Hopkinson, R. A. Hogg, High-Power and Broad-Band Quantum Dot Superluminescent diodes Centred at 1250nm for Optical CoherenceTomography. (Submitted to Jrnl. Of Sel. Topics in Quant. Electron.).

9> H.Y. Liu, M. Hopkinson, C.N. Harrison, M.J. Steer, R. Frith, I.R. Sellers, D.J. Mowbray, M.S. Skolnick "Optimizing the growth of 1.3 um InAs/GaAs dots-in-well structure" J. Appl. Phys. 93 (5), 2931, (2003).].

10> S. K. Ray, T. L. Choi, K. M. Groom, H. Y. Liu, M. Hopkinson, R. A. Hogg " High Power 1.3μm Quantum Dot Superluminescent Light Emitting Diode with Thin Low Temperature GaAs Spacer Layer in the Active Region". (Accepted for publication, IEEE Photon. Technol. Lett.).

11> S. K. Ray, H. Y. Liu, T. L. Choi, K. M. Groom, S. L. Liew, M. Hopkinson, R. A. Hogg "Molecular Beam Epitaxial Growth of High Power Quantum Dot Superluminescent Diodes" Jpn. Jrnl. of Appl. Phys. (Accepted for publication).

12> H. Y. Liu, S. L. Liew, T. Badcock, D. J. Mowbray, M. S. Skolnick, S. K. Ray, K. M. Groom, F. Hasbullah, C. Y. Jin, M. Hopkinson, and R. A. Hogg "P-doped 1.3-μm InAs/GaAs quantum-dot laser with low room-temperature threshold current density and high different efficiency" Appl. Phys. Lett.(Accepted for publication).